Targeting Gli-Mediated Transcription in Bone Metastasis: An Emerging Therapeutic Approach for Patients with Tumor-Induced Bone Disease

By

Kristin Angela Adjoa Sarpong Kwakwa

Dissertation

Submitted to the Faculty of the

Graduate School of Vanderbilt University

in partial fulfillment of the requirements

for the degree of

DOCTOR OF PHILOSOPHY

in

Cancer Biology

May 14, 2021

Nashville, Tennessee

Approved:

Alissa M. Weaver, M.D. Ph.D.

Vito Quaranta, M.D.

Julie A. Rhoades, Ph.D.

Craig L. Duvall, Ph.D.

Scott A. Guelcher, Ph.D.

For my beloved cousin

—

Sylvia Quarshie Williams, M.D.

January 31, 1972 – August 8, 2015

ACKNOWLEDGEMENTS

First and foremost, I would like to thank Dr. Julie Rhoades for her incredible mentorship and unwavering support. It has been a pleasure and a privilege working in her laboratory. I also want to acknowledge my current and former labmates: Alyssa Merkel, Erik Beadle, Natalie Bennett, Kennady Bullock, Dr. Denise Buenrostro, Dr. Shellese Cannonier, Dr. Ushashi Dadwal, Dr. Patrick Mulcrone, and Dr. Milene Moritz. Thank you all for your *humerus* advice and encouragement!

I am extremely grateful to Dr. Alissa Weaver and Dr. Vito Quaranta whose guidance over the past 5 years has been invaluable. I especially want to thank Dr. Craig Duvall for his collaboration and technical expertise. I am also thankful for all the funding sources that supported my dissertation research including the National Institutes of Health, Veterans Affairs, and Department of Defense.

I would be remiss if I did not acknowledge Dr. Jin Chen and Dr. Ann Richmond for their excellent directorship of the Cancer Biology Program. Likewise, I am indebted to both the Initiative for Maximizing Student Diversity program and the Interdisciplinary Graduate Program, particularly Dr. Roger Chalkley, Dr. Linda Sealy, Dr. Christina Keeton, Dr. James Patton, Dr. Elizabeth Bowman, and Carolyn Berry.

Special thanks to all my graduate school friends for keeping me *sane in the brain*: Dr. Aichurok Kamalova, Dr. Nilay Taneja, Dr. Oakleigh Folkes, Dr. Rafael Perez, Dr. Aimee Potter, Dr. Nicole Perry-Hauser, Dr. Jessica Abner, Dr. Matthew Kent, Dr. Austin Featherstone, Dr. Tessa Popay, Ben Kesler, Bryan Gitschlag, Parker Rundstrom, Andrea Cuentas, and Oscar Ortega. Finally, I want to thank my parents, my sister Annie, my brother Mike, and my husband Kalen for their endless love, support, and prayers—I love you more than words can say.

“Praise and glory and wisdom and thanks and honor and power and strength be to our God forever and ever. Amen!” – Revelation 7:12

TABLE OF CONTENTS

LIST OF TABLES

LIST OF FIGURES

CHAPTER 1

INTRODUCTION

1.1 Cancer Metastasis to Bone

Cancer is the second leading cause of death in the United States, ranking only behind heart disease and ahead of the novel COVID-19 infection which has decimated our country this past year. Prostate and breast cancer account for the majority of new cases among U.S. men and women, respectively [1]. Although screening and treatment for localized cancers has improved patient outcomes over the last decade, tumor metastasis remains a significant cause of morbidity and mortality [2].

Advanced solid tumors of the breast, prostate, and lung frequently metastasize to bone, with approximately 70-80% of patients with breast or prostate cancer and 20-40% of lung cancer patients having skeletal metastases upon autopsy [3]. Bone metastases from breast and lung malignancies predominately manifest as osteolytic lesions, characterized by a dramatic increase in osteoclast-mediated bone resorption. However, metastatic prostate tumors often induce formation of poor quality bone, resulting in osteoblastic or sclerotic lesions [4]. Regardless of the phenotype, patients with bone metastases are at high-risk for skeletal-related events (SREs) including severe bone pain, pathological fractures, spinal cord compression (due to vertebral fractures), hypercalcemia (high blood calcium levels), and other adverse comorbidities that significantly decrease patient quality of life [5, 6].

Metastatic disease is extremely challenging to treat as tumors typically spread to multiple bone sites in addition to visceral organs such as the lungs and liver. Historically, treatment has consisted primarily of palliative care including radiotherapy (to alleviate bone pain) and surgery (to prevent imminent fracture) [7, 8]. The current clinical standard-of-care for patients with bone

metastases are anti-resorptives like bisphosphonates and the RANKL inhibitor denosumab which inhibit osteoclast-mediated bone destruction [9]. While these drugs are effective in delaying onset of SREs and are generally well-tolerated by patients, neither agent directly inhibits tumor growth nor have demonstrated the ability to improve patient survival [10, 11]. Therefore, there is a critical need for bone-targeted therapies that reduce both tumor growth and bone destruction.

1.2 Tumor-Induced Bone Disease

Bone remodeling is an essential process that helps maintain the adult skeleton structure as well as normal calcium levels in the body [12]. Specifically, bone remodeling couples the physiological activities of osteoblasts (cells that produce osteoid or new bone) and osteoclasts (cells that resorb or break down bone tissue) [13-15]. These osteoblast and osteoclast functions are tightly regulated to ensure that bone homeostasis remains intact.

Tumors that metastasize to bone disrupt normal bone remodeling by secreting factors such as parathyroid hormone-related protein (PTHrP), vascular endothelial growth factor (VEGF), and various interleukins (e.g., IL-8, IL-11) that increase osteoblast expression of receptor activator of nuclear factor kappa-B ligand (RANKL). RANKL then binds to its receptor on osteoclast precursors resulting in increased osteoclast formation and resorptive activity. In turn, osteoclast-mediated bone resorption releases matrix-bound growth factors like transforming growth factor beta (TGF-β) and bone morphogenetic proteins (BMPs) that promote tumor growth and bone destruction [16, 17]. This vicious cycle of bone loss stimulated by metastatic cancer cells is known as tumor-induced bone disease (TIBD) (**Fig. 1.1**). Previous studies were largely dedicated to developing osteoclast-targeting therapies to minimize bone destruction and prevent fracture. However, with the advent bisphosphonates and RANKL inhibitors, current research efforts to

combat TIBD have focused on disrupting the vicious cycle via directly targeting tumor cells, endothelial cells, immune cells, and other stromal cells in the bone marrow niche [18].

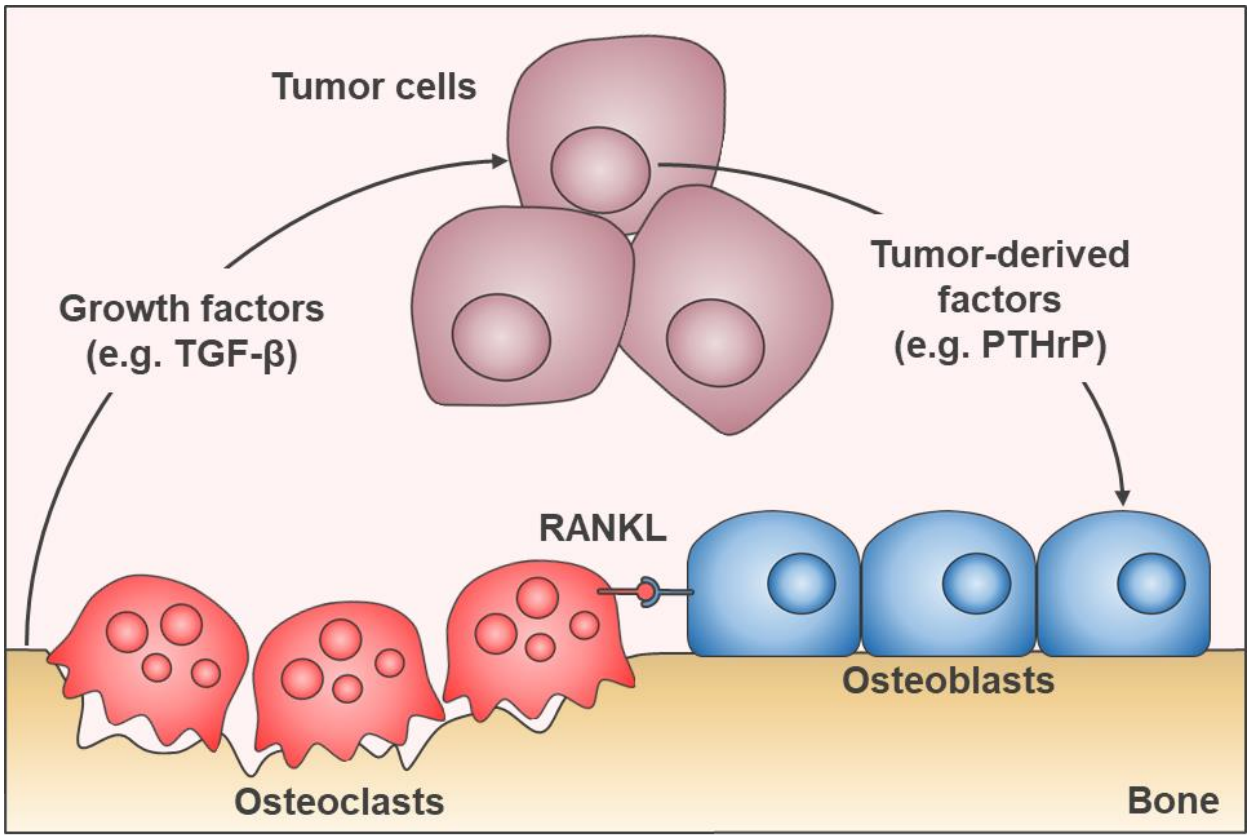

Fig. 1.1. Vicious cycle of tumor-induced bone disease. Tumor cells that metastasize to bone secrete factors such as PTHrP, which promotes osteoclast-mediated bone resorption through RANKL/RANK signaling. The resorption of mineralized bone results in the release of matrix-bound growth factors that stimulate tumor growth and PTHrP expression, thus perpetuating the vicious cycle of tumor-induced bone disease.

1.3 Hedgehog Signaling

The Hedgehog (Hh) signaling pathway regulates essential roles like cell differentiation, proliferation, tissue polarity, and stem cell maintenance during embryonic development [19, 20]. However, aberrant activation of Hh signaling in adult tissues has been implicated in the development and progression of various cancers including basal cell carcinoma (BCC), pancreatic, breast, prostate, lung, and oral cancer [21-25]. In the context of bone metastasis, our previous studies have shown that the Hh transcription factor Gli2 is overexpressed in metastatic tumor cells

and upregulates the expression of PTHrP to promote tumor-induced bone destruction [26, 27]. Conversely, genetic inhibition of Gli2 in tumor cells using an engrailed repressor construct dramatically reduced tumor burden and almost completely blocked bone destruction [28]. Taken together, these observations suggest that Gli2 is a promising therapeutic target for the treatment of TIBD.

Several pharmacological inhibitors against the Hh signal transducer Smoothened (Smo) have been tested in early-phase clinical trials with limited success [29-31]. For instance, Vismodegib (GDC-0449) and Sonidegib (LDE225) are currently FDA-approved for the treatment of BCC but failed to show significant clinical benefit in patients with other advanced solid tumors, which may be attributed to acquired mutations in Smo [32, 33]. Previous studies have also demonstrated that downstream effectors of Hh signaling can be activated via non-canonical pathways such as TGF-β and Wnt independently of Smo expression [28, 34]. In order to circumvent these resistance mechanisms, small molecule inhibitors that target Gli transcription factors downstream of Smo (e.g., GANT58, GANT61, HPI-1, HPI-4) have been identified as potential therapies for Hh-driven cancers [35, 36].

1.4 Unique Properties of the Bone Microenvironment

The extracellular matrix (ECM) is a three-dimensional network of proteins (e.g., collagen, fibronectin, laminin) and other macromolecules that provides structural support to cells in every tissue the body. In addition to serving as a scaffold for cell adhesion and migration, the ECM also plays a significant role in regulating cell behavior including proliferation, differentiation, and gene expression [37]. For example, increased matrix stiffness has been shown to promote both malignant transformation and tumor progression [38, 39].

Bone is characteristically distinct from other tissues because its mineralized ECM is 10^8 times more rigid [40, 41]. Our previous studies have demonstrated that the rigidity of the bone matrix induces malignant cells to adopt an osteolytic phenotype, particularly through the expression of Gli2, PTHrP, and the mechanosensitive factor integrin beta 3 (ITGB3) [42, 43]. Moreover, inhibition of ITGB3 significantly reduced Gli2 and PTHrP expression, thereby blocking bone destruction [43]. These findings suggest that mechanical signaling can also stimulate Gli2 expression independently of the canonical Hh pathway. Since multiple pathways converge on Gli2 to induce osteolysis, directly targeting Gli transcription factors rather than upstream regulators may be a more effective treatment strategy for TIBD.

1.5 Dissertation Focus

My thesis projects primarily involved testing the Gli-antagonist GANT58 in preclinical models of bone metastasis. The research discussed in this dissertation not only provides compelling evidence for the use of GANT58 in conjunction with nanotechnology to effectively block tumor-induced osteolysis, but also offers new insights into the signaling pathways regulating tumor growth and metastasis. This work has significant translational implications for patients with TIBD, particularly those with contraindications for existing anti-resorptive therapies.

CHAPTER 2

INTEGRIN αvβ3 SIGNALING IN TUMOR-INDUCED BONE DISEASE

Adapted from: **Kwakwa KA**, Sterling JA. Integrin αvβ3 signaling in tumor-induced bone disease. *Cancers (Basel)* 2017; 9:84.

2.1 Abstract

Tumor-induced bone disease is common among patients with advanced solid cancers, especially those with breast, prostate, and lung malignancies. The tendency of these cancers to metastasize to bone and induce bone destruction is, in part, due to alterations in integrin expression and signaling. Substantial evidence from preclinical studies shows that increased expression of integrin αvβ3 in tumor cells promotes the metastatic and bone-invasive phenotype. Integrin αvβ3 mediates cell adhesion to several extracellular matrix proteins in the bone microenvironment which is necessary for tumor cell colonization as well as the transmission of mechanical signals for tumor progression. This chapter will discuss the αvβ3 integrin receptor in the context of tumor-induced bone disease. Specifically, the focus will be the role of αvβ3 in modulating cancer metastasis to bone and tumor cell response to the bone microenvironment, including downstream signaling pathways that contribute to tumor-induced osteolysis. A better understanding of integrin dysregulation in cancer is critical to developing new therapeutics for the prevention and treatment of bone metastases.

2.2 Introduction

Advanced solid tumors frequently metastasize to bone, occurring in approximately 70–80% of patients with breast or prostate cancer, and in 30–40% of lung cancer patients [3]. Metastatic tumors disrupt normal bone remodeling to induce bone destruction by secreting factors

(e.g., parathyroid hormone-related protein (PTHrP), interleukin-8, interleukin-11) that promote osteoclast formation. Subsequently, osteoclast-mediated bone resorption releases matrix-bound growth factors such as transforming growth factor beta (TGF-β), which further stimulate tumor growth and bone destruction [16, 17]. Alternatively, metastatic tumors can secrete factors (e.g., bone morphogenetic proteins, insulin-like growth factors, endothelin-1) that promote osteoblast proliferation and differentiation, resulting in bone formation and sclerotic lesions [44]. This vicious cycle of tumor-induced bone disease (TIBD) results in severe comorbidities including extreme bone pain, spinal cord compression, hypercalcemia, and pathological fractures that significantly decrease patient quality of life and increase mortality [6, 45, 46]. Numerous preclinical studies have shown that the expression of specific integrin heterodimers, and their downstream signaling pathways, are perturbed in cancers that metastasize to bone. Most notably, integrin αvβ3 is upregulated in bone-metastatic tumor cells as well as multiple myeloma cells, and has been implicated in the progression of TIBD [47-49]. Interestingly, while integrin αvβ is also expressed in primary bone cancers such as osteosarcoma and chondrosarcoma, high αvβ3 expression has primarily been shown to promote metastasis of these tumors to the lung [50, 51]. Hence, αvβ3 is a promising therapeutic target against bone metastases and the mechanisms by which it mediates the pathogenesis of secondary bone cancers and multiple myeloma are an area of extensive study [52]. This chapter will discuss integrin αvβ3 in the context of metastatic cancers in bone, particularly how αvβ3 modulates tumor cell response to the bone microenvironment as well as downstream signaling pathways that promote tumor-induced bone destruction.

2.3 The Biology of Integrin αvβ3

Integrin αvβ3 is a heterodimeric transmembrane glycoprotein that mediates cell adhesion to the extracellular matrix (ECM) through recognition of conserved arginine–glycine–aspartic acid (RGD) motifs in various ligands including osteopontin, vitronectin, and fibronectin [53]. Like other integrins, αvβ3 acts as a bidirectional signaling molecule. During "inside-out" signaling, adaptor proteins talin and kindlin bind the cytoplasmic tail of the β3 subunit, which not only links the integrin to the actin cytoskeleton but also causes conformational changes that increase its affinity for extracellular ligands [54, 55]. In turn, ligation of activated αvβ3 triggers integrin clustering at the plasma membrane and recruitment of additional focal adhesion proteins (e.g., FAK, SFKs, paxillin, vinculin) which are important for actin cytoskeletal assembly as well as signal transduction ("outside-in" signaling) [56, 57]. Integrin αvβ3 signaling is also modulated by lateral associations with growth factor receptors such as epidermal growth factor receptor (EGFR) [58] and TGF-β receptor II (TGFβRII) [59], and there is significant crosstalk between the downstream pathways (e.g., Ras-MEK-MAPK, PI3K-Akt, RhoA-ROCK) regulating cell migration, proliferation, and survival [60, 61]. With respect to normal bone physiology, αvβ3 plays an important role in osteoclast-mediated bone resorption [62, 63], angiogenesis [64, 65], and phagocytosis of apoptotic cells [66].

2.4 Integrin αvβ3 is Upregulated in Cancers that Metastasize to Bone

Metastasis is a multi-step process whereby cancer cells detach from the primary tumor, locally invade the surrounding tissue, transit through the vasculature or lymphatics, and colonize distant sites. Each stage of the metastatic cascade requires the activity of many different cell adhesion molecules, including integrins. Although several integrin heterodimers have been implicated in tumor cell interactions with the bone microenvironment (e.g., α2β1, α4β1, α5β1)

[67], αvβ3 has been identified as a critical integrin for bone metastasis. Previous investigations have shown that the expression of integrin αvβ3 is increased in various bone-metastatic tumors such as breast, lung, and renal cancer compared to normal tissues [68]. One notable early study also demonstrated by immunohistochemistry that bone-residing metastases from breast cancer patients expressed higher levels of integrin αvβ3 compared to their respective primary tumors [69]. Collectively, these findings emphasize the importance of integrin αvβ3 in bone metastasis.

Another study illustrated that bone-metastatic subclones of a parental cancer cell line constitutively overexpressed integrin αvβ3 [70]. Specifically, a bone-tropic human breast cancer cell line (B02) was first established by repeated *in vivo* passages during which MDA-MB-231 breast carcinoma cells were injected into the left ventricle of the heart of nude mice and isolated from bone metastases [71]. The expression of various integrin heterodimers in these B02 cells was then assessed by immunoblotting and flow cytometry [70]. Results showed that integrin αvβ3 was overexpressed in B02 cells compared to the parental MDA-MB-231 cells while the cell surface expression of other integrins was not significantly different between the two cell lines.

In a more recent report, de novo expression of integrin αvβ3 in tumor cells that typically metastasize to the lungs was sufficient to promote homing to bone [72]. First, αvβ3 was exogenously expressed in the 66cl4 mouse mammary carcinoma cell line (66cl4beta3) and injected into the mammary fat pad of Balb/c mice. The 66cl4beta3-tumor bearing mice had significantly higher metastatic burden in the spine (20-fold increase) compared to mice that were inoculated with control 66cl4 cells. Spontaneous metastasis of 66cl4beta3 tumors to the long bones, particularly the femur, was also observed but these metastases were not detected in mice injected with control 66cl4 cells. Furthermore, several studies have shown that expression of functionally inactive αvβ3 mutants or treatment with αvβ3 antagonists significantly reduced the ability of tumor

cells to colonize bone [48, 70, 73]. Taken together, these data demonstrate that integrin αvβ3 contributes to the osteotropism of metastatic cancer cells.

2.5 Expression of Tumor-Specific αvβ3 Promotes Bone Destruction

It is well-established that metastatic cancers induce osteoclastogenesis to initiate bone resorption, which facilitates tumor expansion in this metastatic niche [16, 17, 74]. Evidence from one preclinical study showed an increased number of osteoclasts adjacent to bone-residing tumors that overexpressed integrin αvβ3 [72]. In a previously described study, bone-metastatic human breast cancer cells that constitutively overexpressed αvβ3 (B02) induced significantly larger and more numerous osteolytic lesions in animals compared to the parental MDA-MB-231 cells from which they were derived [70]. In a later study by the same group, human MDA-MB-231 breast cancer cells were stably transfected to overexpress αvβ3 and subsequently injected into the tail vein of nude mice [75]. Mice bearing αvβ3-overexpressing tumors had significantly more bone destruction (2-fold increase) compared to mice inoculated with mock-transfected cells. Furthermore, treatment with the αvβ3 inhibitor PSK1404 significantly reduced the incidence of osteolysis in mice with αvβ3-overexpressing tumors. Interestingly, prostate cancer cells lacking integrin αvβ3 expression promote bone resorption while αvβ3-expressing prostate cancer cells stimulate bone formation, thus illustrating the role of αvβ3 in the development of osteoblastic lesions [48].

The molecular mechanisms by which tumor-specific αvβ3 promotes osteolysis are still being explored, but prior studies have shown that αvβ3 signaling resulted in the nuclear localization of transcription factors such as Runx2, which upregulated matrix metalloproteinases (e.g., MMP-9, MMP-13) and soluble receptor activator of NF-κB ligand (RANKL) to aid in bone

matrix dissolution as well as osteoclast recruitment, differentiation, and function [76, 77]. More importantly, integrin αvβ3 can augment TGF-β signaling [59] which has been shown to stimulate the expression of PTHrP by tumor cells and osteoblast expression of RANKL, thereby promoting osteoclast-mediated bone destruction [16, 28]. In summary, these studies illustrate that increased αvβ3 expression in metastatic cancer cells contributes to the pathophysiology of tumor-induced bone destruction.

2.6 Integrin αvβ3 Modulates Tumor Response to the Rigid Bone Matrix

Over the past few decades, the ECM has been increasingly recognized as an important regulator of cell behavior and gene expression. For instance, matrix stiffness is increased in fibrotic soft tissues and has been linked to the malignant transformation of epithelial cells [38, 39]. Matrix rigidity also stimulates integrin clustering, focal adhesion assembly, and RhoA-ROCK-dependent actomyosin contractility that can induce changes in gene expression. Mineralized bone is unique in that it has an elastic modulus ranging from 1.7 to 2.9 × 10^{10} Pa, which is orders of magnitude more rigid than soft tissues (10^{2}–10^{6} Pa) [40, 41]. One study explored the effects of bone matrix rigidity on metastatic tumors by culturing osteolytic MDA-MB-231 breast cancer cells and non-osteolytic MCF-7 cells on rigid bone-like substrates [42]. MDA-MB-231 cells significantly upregulated their expression of PTHrP (2.5-fold increase) and other genes involved in TIBD in response to substrate stiffness while MCF-7 cells showed no difference in PTHrP expression. Although tumor-specific integrins were not investigated, strong evidence indicated that the effects of substrate rigidity on PTHrP expression were mediated by mechanically transduced signals, particularly through activation of ROCK.

The mechanism by which matrix rigidity mediates osteolytic gene expression in metastatic tumors was further elucidated in a more recent study [43]. Specifically, metastatic breast (MDA-MB-231), prostate (PC-3), and lung (RWGT2) cancer cells cultured on bone-mimetic rigid substrates had increased expression of integrin αvβ3, Gli2, and PTHrP compared to cells cultured on more compliant substrates. Fluorescence resonance energy transfer and co-immunoprecipitation assays showed that colocalization of integrin αvβ3 and TGFβRII was significantly increased in tumor cells cultured on rigid substrates. The authors proceeded to demonstrate that rigidity-stimulated clustering of αvβ3 and TGFβRII activates Src which stimulates Gli2 and PTHrP expression via p38 MAPK signaling. Inhibition of integrin αvβ3 in MDA-MB-231 cells using either an shRNA or the monoclonal antibody LM609 significantly decreased both Gli2 and PTHrP expression. Furthermore, mice injected with MDA-MB-231 cells stably expressing shRNA against αvβ3 had reduced bone destruction. Collectively, these data indicate that crosstalk between integrin αvβ3 and TGFβ signaling modulates tumor cell response to the rigid bone microenvironment and promotes the transition of tumor cells to a bone-destructive phenotype.

2.7 Targeting Integrin αvβ3-Expressing Tumors in Bone

Currently, the standard of care for patients with TIBD are drugs that interfere with osteoclast-mediated bone resorption such as bisphosphonates [78] and RANKL inhibitors [79]. Clinical trials have demonstrated that these drugs are efficacious in reducing the frequency of skeletal-related events (SREs) (e.g., pathologic fractures, spinal cord compression, hypercalcemia) in patients with bone metastases [78]. However, there remains a need for therapies that directly target tumor cells residing in bone. Integrin αvβ3 is a promising therapeutic target for TIBD due

to its high expression in metastatic tumors, angiogenic cells, and osteoclasts [80]; thus, αvβ3 antagonists could potentially disrupt multiple aspects of disease progression. Substantial evidence from preclinical investigations show that treatment with integrin αvβ3-targeting peptides (e.g., ATN-161, S247, cilengitide), non-peptide small molecules (e.g., PSK1404), or monoclonal antibodies (e.g., LM609) significantly reduces tumor growth and osteolysis in a variety of cancer types [43, 73, 75, 81].

Several αvβ3-targeting drug candidates have advanced to clinical trials for the treatment of osteoporosis and cancer. The RGD-mimetic cyclic peptide cilengitide was first developed for treatment of glioblastoma multiforme [82, 83] but has been investigated for use in patients with advanced solid tumors including prostate cancer, non-small cell lung cancer, and squamous cell carcinoma. The humanized monoclonal antibody etaracizumab was also in clinical trials for prostate cancer, ovarian cancer, and metastatic melanoma [84]. More recently, the small molecule GLPG0187 was evaluated for its effects in patients with progressive glioma and other advanced solid malignancies [85]. Despite success in early clinical trials, many of these therapies did not produce clinically relevant outcomes compared to standard chemoradiotherapy; however, few studies specifically targeted cancer patients with bone metastases. To evaluate the efficacy of novel or existing αvβ3 antagonists against bone metastases, future trials will need to be more inclusive of patients with TIBD.

2.8 Concluding Remarks

Patients with advanced solid cancers frequently develop TIBD which involves growth of metastatic tumors in bone as well as osteoclast-mediated bone destruction. Despite palliative treatments, TIBD remains a highly debilitating disease for many cancer patients. Current therapies

focus on inhibiting osteoclast-mediated bone resorption to reduce the risk of SREs, but there is a compelling need for therapies directly targeting metastatic tumor cells in bone. Despite the failure of existing drugs against advanced soft tissue tumors in clinical trials, integrin αvβ3 may be a promising therapeutic target for patients with TIBD as it is highly expressed in several bone-metastatic tumors including breast, prostate, and lung cancer. Preclinical studies have also demonstrated that the aberrant expression of tumor-specific αvβ3 promotes metastasis to bone, thereby increasing skeletal tumor burden and osteolysis. Mechanistically, integrin αvβ3 has been shown to mediate tumor cell response to the rigid bone microenvironment, which results in the upregulation of genes associated with bone destruction (**Fig. 2.1**). Still, the exact mechanisms of integrin αvβ3 regulation in TIBD are not fully understood and the signaling pathways that are altered by changes in αvβ3 expression will need to be further explored in order to identify potential therapeutic targets. It is also important to note that because integrin αvβ3 is expressed by osteoclasts, proliferating endothelial cells, and certain immune cell populations, therapies that target αvβ3 may affect multiple aspects of TIBD in addition to bone resorption, including angiogenesis and inflammatory immune responses. Future studies will need to examine, in greater detail, the impact of integrin αvβ3 suppression on the tumor-bone microenvironment. A better understanding of integrin dysregulation in cancer and the mechanisms by which tumors respond to the bone microenvironment is crucial in order to develop novel therapeutics for the treatment of bone metastases.

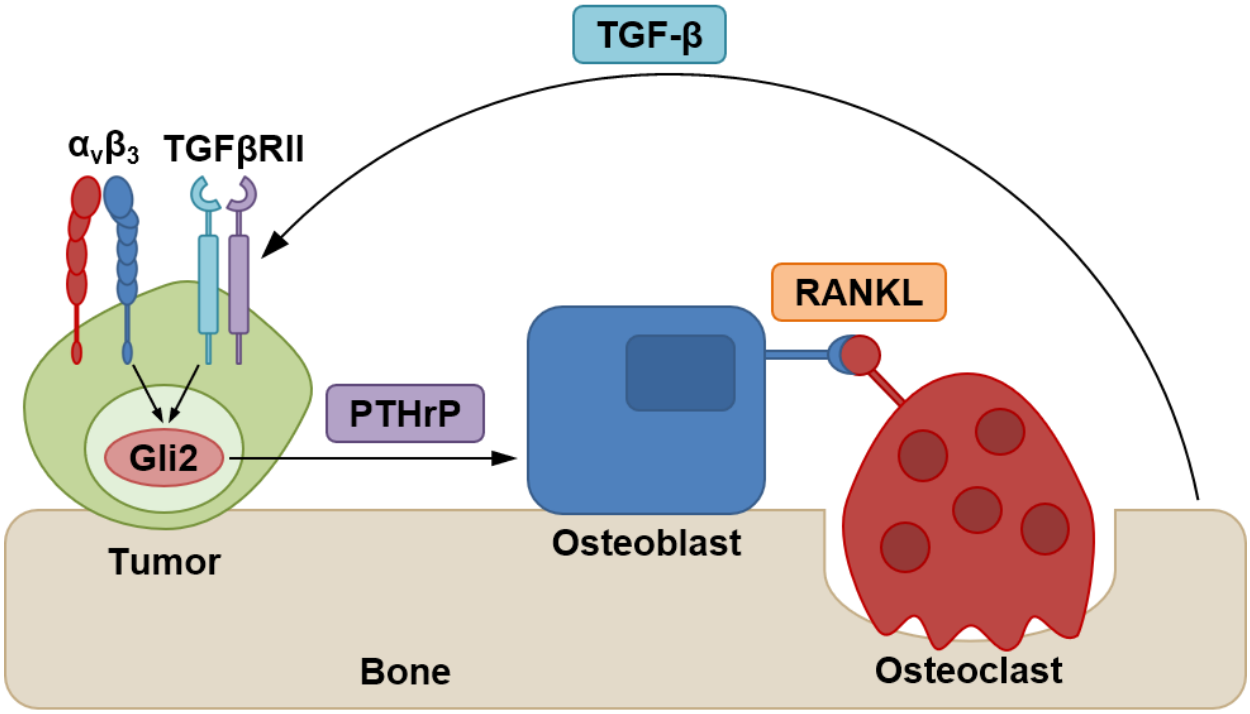

Fig. 2.1. Matrix rigidity regulates the transition of tumor cells to a bone-destructive phenotype via αvβ3 and TGFβRII. In the rigid bone microenvironment, integrin αvβ3 interacts with TGFβRII to induce the expression of Gli2, which in turn increases secretion of osteolytic factors such as PTHrP to stimulate osteoclast-mediated bone destruction.

CHAPTER 3

SYSTEMIC DELIVERY OF A GLI INHIBITOR VIA POLYMERIC NANOCARRIERS INHIBITS TUMOR-INDUCED BONE DISEASE

Adapted from: Vanderburgh JP*, **Kwakwa KA***, Werfel TA, et al. Systemic delivery of a Gli inhibitor via polymeric nanocarriers inhibits tumor-induced bone disease. *J Control Release* 2019; 311-312:257-272.

3.1 Abstract

Solid tumors frequently metastasize to bone and induce bone destruction leading to severe pain, fractures, and other skeletal-related events (SREs). Osteoclast inhibitors such as bisphosphonates delay SREs but do not prevent skeletal complications or improve overall survival. Because bisphosphonates can cause adverse side effects and are contraindicated for some patients, we sought an alternative therapy to reduce tumor-associated bone destruction. Our previous studies identified the transcription factor Gli2 as a key regulator of parathyroid hormone-related protein (PTHrP), which is produced by bone metastatic tumor cells to promote osteoclast-mediated bone destruction. In this study, we tested the treatment effect of a Gli antagonist GANT58, which inhibits Gli2 nuclear translocation and PTHrP expression in tumor cells. In initial testing, GANT58 did not have efficacy *in vivo* due to its low water solubility and poor bioavailability. We therefore developed a micellar nanoparticle (NP) to encapsulate and colloidally stabilize GANT58, providing a fully aqueous, intravenously injectable formulation based on the polymer poly(propylene sulfide)$_{135}$-*b*-poly[(oligoethylene glycol)$_9$ methyl ether acrylate]$_{17}$ (PPS$_{135}$-*b*-POEGA$_{17}$). POEGA forms the hydrophilic NP surface while PPS forms the hydrophobic NP core that sequesters GANT58. In response to reactive oxygen species (ROS), PPS becomes hydrophilic and degrades to enable drug release. In an intratibial model of breast cancer bone metastasis,

treatment with GANT58-NPs decreased bone lesion area by 49% ($p < 0.01$) and lesion number by 38% ($p < 0.05$) and resulted in a 2.5-fold increase in trabecular bone volume ($p < 0.001$). Similar results were observed in intracardiac and intratibial models of breast and lung cancer bone metastasis, respectively. Importantly, GANT58-NPs reduced tumor cell proliferation but did not alter mesenchymal stem cell proliferation or osteoblast mineralization *in vitro*, nor was there evidence of cytotoxicity after repeated *in vivo* treatment. Thus, inhibition of Gli2 using GANT58-NPs is a potential therapy to reduce bone destruction that should be considered for further testing and development toward clinical translation.

3.2 Introduction

Despite advances in early screening and adjuvant therapy, metastatic disease remains a leading cause of cancer patient morbidity and mortality. One of the most common metastatic sites is the skeleton. Approximately 70–80% of patients with breast or prostate cancer and 30–40% of patients with lung or renal cancer who die from disease develop bone metastases [7, 86]. Patients with bone metastases experience complications including severe bone pain, pathological fractures, and other skeletal-related events (SREs) that significantly reduce their quality of life [7, 87].

Once established in bone, cancer cells disrupt normal bone remodeling to initiate a vicious cycle of tumor-induced bone disease (TIBD) [6]. Specifically, tumor cells in the bone microenvironment secrete parathyroid hormone-related protein (PTHrP), which increases osteoblast expression of receptor activator of nuclear factor kappa-B ligand (RANKL) and consequent osteoclast-mediated bone resorption [16, 18]. Current treatment strategies for TIBD include the anti-resorptive therapies denosumab (RANKL inhibitor) and bisphosphonates (osteoclast inhibitor) [7, 86, 88]. However, these drugs are associated with increased risk of

atypical femoral fractures and osteonecrosis of the jaw [89-93]. Conventional chemotherapy and radiation therapies suppress bone marrow cells, resulting in adverse hematologic events and poor bone quality [94, 95]. Tumor-targeted therapies that reduce SREs while minimizing damage to the bone are currently unavailable.

The Hedgehog (Hh) signaling pathway is a key regulator of embryonic development with essential roles in cell differentiation and proliferation, tissue polarity, and stem cell maintenance [19, 20] but has limited activity in the healthy adult skeleton. Aberrant Hh signaling in adults has been implicated in the development and progression of breast, prostate, and lung cancer [21-24]. However, pharmacological inhibitors of the Hh receptor Smoothened (Smo) failed to show significant clinical benefit in patients with advanced solid tumors [29-31] due to acquired mutations in Smo and/or non-canonical Hh pathway activation [28, 32-34]. Small molecule inhibitors that target the Hh transcription factor Gli2 downstream of Smo circumvent these resistance mechanisms [35, 36]. Our previous studies demonstrated that Gli2 stimulates PTHrP expression in bone-destructive tumor cells [26, 27] and that genetic inhibition of Gli2 attenuates the ability of cancer cells to colonize bone and induce osteolysis *in vivo* [28]. The small molecule Gli-antagonists GANT58 and GANT61 have shown promising anti-tumor effects *in vitro* and in xenograft models [35, 96-98], but their low water solubility and poor pharmacokinetics (PK) has limited their testing to less translationally-relevant studies using direct injection into subcutaneous tumors. Thus, while Gli2 is a promising therapeutic target for TIBD, small molecule Gli inhibitors have not been tested using systemic delivery nor in models of bone metastasis.

Nanoparticle (NP) drug delivery systems have emerged in recent years as a promising approach to overcome PK and toxicity limitations of otherwise promising drug candidates. Cancer nanomedicines have been widely reported as carriers for chemotherapeutics [99, 100]. However,

molecularly targeted agents (MTAs) offer multiple benefits over conventional chemotherapies [101-103]. Most notably, their selectivity reduces normal tissue toxicity, thereby improving the therapeutic index [104]. GANT58 is a therapeutically promising MTA with limited bioavailability, and thus is an excellent candidate for development in a nanoparticle formulation to improve its PK *in vivo*. Polymer-based micellar nanoparticles have been shown to enhance the solubility and systemic PK of hydrophobic compounds *in vivo* and have also produced clinical success in cancer patients [105-110]. Further, advances in polymer science toward environmentally-responsive, “smart" polymer formulations have improved target-specific drug delivery [111-114].

Herein, we employ polymeric nanoparticles to encapsulate GANT58 (GANT58-NPs) to enable systemic delivery with distribution to breast and lung cancer bone metastases. Following NP characterization, evaluation of *in vitro* toxicity, and *in vivo* biodistribution and PK studies, we tested GANT58-NPs in mouse models of bone metastasis in order to investigate its therapeutic efficacy and safety. We hypothesized that GANT58-NPs delivered intravenously (i.v.) in a fully-aqueous formulation would reduce tumor-induced bone destruction with minimal effects on bone marrow progenitors.

3.3 Materials and Methods

Cell lines and reagents

Bone-metastatic variants of the human breast cancer cell line MDA-MB-231 and human squamous non-small cell lung carcinoma cell line RWGT2 were generated in our laboratory as previously published [26, 28, 34, 115]. MDA-MB-231-bone and RWGT2-bone clones were maintained in DMEM (Cellgro) and α-MEM (Cellgro) respectively, supplemented with 10% fetal bovine serum (FBS; Hyclone Laboratories) and 1% penicillin/streptomycin (P/S; Mediatech).

Human mesenchymal stem cells (hMSCs; Extem Biosciences) were maintained in Mesenchymal Stem Cell Growth Medium 2 (PromoCell). GANT58 was purchased from Santa Cruz Biotechnology (Dallas, TX, USA). All other reagents were purchased from Sigma Aldrich (St. Louis, MO, USA) unless otherwise specified.

Immunohistologic staining of patient tumor samples

Bone metastatic (n = 17) and soft tissue (n = 3) tumor biopsies were obtained from the Cooperative Human Tissue Network (CHTN) Western Division in accordance with our Institutional Review Board (IRB #151700)-approved protocol and upon informed consent from patients undergoing surgical resection. All patient information was deidentified prior to receipt by investigators to protect subject privacy. The clinical features of the patient samples are summarized in **Table S3.1**. Briefly, fresh tissue samples were fixed in 10% formalin (Fisher Scientific) for 48 hr and stored in 70% ethanol at 4°C before being processed and embedded in paraffin. Serial sections (5-μm thickness) were placed on slides, deparaffinized in xylene, and rehydrated with graded alcohol solutions, followed by antigen retrieval in 10 mM sodium citrate buffer at 80°C for 30 min. Sections were then blocked with 5% goat serum in phosphate-buffered saline (PBS)/0.1% Tween-20 for 30 min and incubated with rabbit polyclonal anti-Gli2 primary antibody (1:500, Novus Biologicals) overnight at 4°C. The VECTASTAIN Elite ABC HRP Kit (Vector Laboratories) with biotinylated goat anti-rabbit secondary antibody and the ImmPACT NovaRED Peroxidase Substrate Kit (Vector Laboratories) were both used according to the manufacturer's protocol. After counterstaining with hematoxylin, tumor sections were mounted with Cytoseal XYL (Thermo Scientific) and imaged using an Olympus BX41 microscope

equipped with an Olympus DP71 camera. Gli2-positive staining was quantified using Metamorph software (Molecular Devices, Inc.).

In silico analyses of patient tumors

The Gene Expression Omnibus (GEO) database was queried on 11 October 2018 for the GEO accession number GSE14017 to obtain the gene expression profiling dataset of 29 human breast cancer metastases in different organs, which was generated by X.H. Zhang, et al. [116]. For the purposes of their study, the authors used the Affymetrix Human Genome U133 Plus 2.0 Array (https://www.ncbi.nlm.nih.gov/geo/query/acc.cgi?acc=GSE14017) [116]. To determine Gli2 expression in bone, brain, and lung cancer metastases of breast cancer patients, the identifiers corresponding to Gli2 (207034_s_at, 228537_at, 208057_s_at) were located on the platform record, and gene expression values across dataset samples were retrieved. One brain metastasis (GSM352120) and one lung metastasis (GSM352127) sample from the microarray dataset were omitted from final statistical analyses after performing the Grubb's test for outliers (GraphPad Software, Inc.).

Polymer synthesis and characterization

The diblock poly(propylene sulfide)$_{135}$-*b*-poly[(oligoethylene glycol)$_9$ methyl ether acrylate]$_{17}$ (PPS$_{135}$-*b*-POEGA$_{17}$) was synthesized via a combination of anionic and reversible addition-fragmentation chain transfer (RAFT) polymerization as previously published [105, 106]. Briefly, the PPS block was synthesized via anionic polymerization to a degree of polymerization of approximately 135 (10 kDa), conjugated to the RAFT macro-chain transfer agent, and chain-extended with POEGA to a degree of polymerization of approximately 17 (8 kDa). Polymer

structure was confirmed by ^{1}H-NMR. Fluorophore-grafted polymers were synthesized by adding a small amount of the amine-reactive intermediate pentafluorophenyl acrylate (PFPA) into the reaction mixture with POEGA at a 1:1 mole ratio (PFPA:PPS-ECT). The reaction was allowed to proceed for 24 h at 70ºC. The reaction was dialyzed against methanol and dried under vacuum. The resulting polymer (0.021 mmol) was reacted with Cy7-amine or Cy5-amine fluorophores (0.042 mmol) in DMSO for 24 hr at 50ºC. The reaction mixture was again dialyzed against methanol and dried under vacuum.

GANT58-NP preparation and characterization

GANT58-loaded PPS_{135}-*b*-$POEGA_{17}$ micellar nanoparticles (GANT58-NPs) were formed by the bulk solvent evaporation method. PPS_{135}-*b*-$POEGA_{17}$ (10 mg) was co-dissolved with GANT58 (2.5 mg) in chloroform (0.1 mL) and added dropwise to a vial containing vigorously-stirring PBS (1 mL). The oil-in-water biphasic solution was left stirring overnight to evaporate the chloroform and allow for micelle formation. The resulting micelle solution was passed through a 0.45 µm syringe filter producing the final GANT58-NP formulation. The same technique, excluding addition of GANT58, was used to create empty PPS_{135}-*b*-$POEGA_{17}$ micellar nanoparticles (Empty-NPs). Dynamic light scattering (DLS) was used to measure the hydrodynamic diameter (D_h) and zeta potential (ζ) of the GANT58-NPs and Empty-NPs via a Malvern Zetasizer Nano-ZS (Malvern Instruments Ltd., Worcestershire, UK) equipped with a 4 mW He-Ne laser operating at λ = 632.8 nm. Transmission electron microscopy (TEM) samples were prepared as previously described [106]. Briefly, 5 µL of GANT58-NPs were added to a pure carbon TEM grid (Ted Pella, Inc., Redding, CA, USA), blotted dry after 60 s, and counterstained with 3% uranyl acetate for 20 s. After vacuum drying, the grids were imaged on an FEI Tecnai

Osiris microscope operating at 200 kV for TEM. GANT58 loading was quantified utilizing the fluorescence properties of GANT58. Aliquots of GANT58-NPs in PBS (50 µL) were added in triplicate to a 96-well plate and dissolved by adding an equal volume of DMF. On the same plate, a standard of GANT58 in the same solvent (1:1 DMF:PBS) was prepared. Fluorescence intensity of GANT58 (ex. 485 nm, em. 590 nm) was measured on a micro-plate reader (Tecan Infinite 500, Tecan Group Ltd., Mannedorf, Switzerland) and GANT58 concentration was calculated from the standard curve.

Critical micelle concentration (CMC) determination

The CMC was determined as previously described [105, 106]. Nile Red (NR) was substituted for GANT58 as the loaded species due to its unique fluorescence properties and its similar molecular weight to GANT58. NR is highly fluorescent in hydrophobic environments yet non-fluorescent in polar, aqueous environments, making it useful for characterizing self-assembly properties. Briefly, NR-loaded PPS_{135}-*b*-$POEGA_{17}$ micelles (NR-NPs) were prepared by the described bulk solvent evaporation method. NR loading was measured as described for GANT58. Different dilutions of the NR-NPs were prepared in PBS, and NR fluorescence (ex. 535 nm, em. 612 nm) was read on a micro-plate reader (Tecan Infinite 500, Tecan Group Ltd., Mannedorf, Switzerland). The CMC was defined as the intersection point on the plot of NR fluorescence versus polymer concentration as previously described [105, 106].

Hydrogen peroxide (H_2O_2)-dependent drug release

The ROS-responsive behavior of the PPS_{135}-b-$POEGA_{17}$ NPs was assessed as described previously, using H_2O_2 as the ROS-species [106]. Briefly, NR-NPs prepared as described were

exposed to a range of concentrations (0-1.5 M) of H_2O_2. Fluorescence intensity of NR was monitored in a 96-well plate using a micro plate reader (Tecan Infinite 500, Tecan Group Ltd., Mannedorf, Switzerland). Release of the NR due to NP oxidation and destabilization was assessed over time based on disappearance of NR fluorescence. The loss of fluorescence for each sample at each time point was determined by subtracting the fluorescent value from that of the sample prior to H_2O_2 addition, and the percent fluorescence remaining was determined by normalization to the same value (before addition of H_2O_2). This value for percent fluorescence remaining was subtracted from 100% and expressed as a percent release for each sample at each time point.

Quantitative real-time polymerase chain reaction (qPCR)

Total RNA was extracted from MDA-MB-231 bone cells after 48 hr GANT58 (0-20 μM) treatment with the RNeasy Mini Kit (Qiagen) as per manufacturer's instructions. Complimentary DNA (cDNA) was synthesized from 1 μg RNA using the qScript cDNA SuperMix (Quanta Biosciences) and serially diluted to create a standard curve. qPCR was performed on a 7500 Real-Time PCR System (Applied Biosciences) using TaqMan Universal PCR Master Mix (Applied Biosystems) and the TaqMan primers for eukaryotic 18S rRNA (4352930E, Applied Biosystems) or human PTHLH (Hs00174969_m1, Thermo Fisher) under the following conditions: 10 min at 95°C, (15 s at 95°C, 1 min at 60°C) x 40 cycles. Three technical replicates were run for each biological replicate. Quantification was performed using the absolute quantitative method using 18S as an internal control.

Western blotting

Nuclear and cytoplasmic protein lysates were isolated from MDA-MB-231 bone cells after 72 hr treatment with GANT58 (0-20 μM) using NE-PER Nuclear and Cytoplasmic Extraction Reagents (Thermo Scientific) supplemented with Halt Protease and Phosphatase Inhibitor Cocktail (Thermo Scientific). Protein concentrations were quantified using the Pierce BCA Protein Assay Kit (Thermo Scientific). Protein samples (20 μg/well) were separated on a 4–20% Mini-PROTEAN TGX polyacrylamide gel (Bio-Rad) by SDS-PAGE prior to being transferred to a nitrocellulose membrane (Bio-Rad) with the Trans-Blot Turbo Transfer System (Bio-Rad). Membranes were then blocked for 1 hr in 1X TBS containing 0.1% Tween-20 and 5% w/v BSA and incubated with the following primary antibodies at 4°C overnight: anti-Gli2 (1:500, Novus Biologicals), anti-TATA binding protein (TBP) (1:1000, Cell Signaling), or anti-Glyceraldehyde 3-phosphate dehydrogenase (GAPDH) (1:5000, Cell Signaling). Following incubation with anti-rabbit IgG HRP-linked secondary antibody (Cell Signaling) at room temperature for 1 hr, protein bands were developed by Western Lightning Plus-ECL (Perkin Elmer) and imaged on a ChemiDoc MP Imaging System (Bio-Rad). The intensity of each band was determined by densitometry using ImageJ software.

Tumor cell proliferation assay

MDA-MB-231-bone cells were seeded in a 96-well plate at 2,000 cells/well in quadruplicate. Vehicle (DMSO), free GANT58, Empty-NPs, or GANT58-NPs were introduced to wells after 24 hr. Cell proliferation was determined after 24 hr treatment by 3-(4,5-dimethylthiazol-2-yl)-5-(3-carboxymethoxyphenyl)-2-(4-sulfophenyl)-2H-tetrazolium (MTS) assay using the CellTiter 96 Aqueous Non-Radioactive Cell Proliferation Assay kit (Promega) per the

manufacturer's instructions. Absorbance values were measured on a plate reader at optical density (OD) 450 nm.

hMSC proliferation assay

hMSCs were seeded in a 96-well plate at 50,000 cells/mL (5,000 cells/well). Vehicle (DMSO), free GANT58, Empty-NPs, or GANT58-NPs were introduced to the wells after 24 hr. As described, cell proliferation was determined using the CellTiter 96 Aqueous Non-Radioactive Cell Proliferation Assay kit (Promega) per manufacturer's instructions. Absorbance values were measured at OD 490 nm.

Fluorescence microscopy

MDA-MB-231-bone cells were seeded in a 4-chamber well slide at 20,000 cells/well. After 24 hr, media was replaced with media containing treatments. For NP uptake experiments, GANT58-Cy5NPs were added and incubated for 12 hr after treatment. Cells were then stained with DAPI and viewed on a Nikon Eclipse TI confocal microscope for Cy5 and DAPI fluorescence. For Gli2 immunofluorescence, cells were incubated with 20 μM GANT58, 20 μM GANT58-NP, Empty-NP, or DMSO control for 72 hr, fixed with 4% neutral-buffered formalin, and washed with Tris-buffered saline (TBS). The cells were then blocked and permeabilized with TBS containing 2.5% BSA, 0.1% Tween, and 0.2% Triton-X for 5 min. Gli2 antibody (1:500, Novus Biologicals) was then incubated in permeabilization buffer overnight at 4ºC. Cells were then washed again with TBS and incubated with secondary Alexa-488 anti-rabbit antibody (1:2000, Thermo Fisher) for 90 min. The cells were then stained with DAPI for 10 min, washed, and mounted with a cover slip. Cells were imaged using an Olympus BX60 fluorescence

microscope for DAPI and Alexa-488 fluorescence. ImageJ was used to calculate the Manders coefficient to quantify Gli2 nuclear colocalization.

Cell viability, cytotoxicity, and apoptosis

MDA-MB-231 bone cells were seeded in a 96-well plate (5,000 cells/well) and treated with GANT58 (0-80 μM) for 24 hr and viability, cytotoxicity, and apoptosis were measured using the ApoTox-Glo Triplex Assay (Promega) according to the manufacturer's instructions. Briefly, 20 μL of Viability/Cytotoxicity Reagent was added to 100 μL of media in each well and incubated for 30 min at 37ºC. Fluorescence intensity was then measured for viability (ex. 400 nm, em. 505 nm) and cytotoxicity (ex. 485 nm, em. 520 nm). Luminescence was measured for apoptosis (caspase 3/7 activation) following the addition of 100 μL of Caspase-Glo 3/7 Reagent and 30 min incubation at room temperature.

Mineralization assay

hMSCs were seeded at 25,000 cells/mL (50,000 cells/well) in a 24-well plate and allowed to grow to confluency for 48 hr in MSC Growth Medium 2 (PromoCell) as we have described previously [117]. Cells were then induced with MSC Osteogenic Differentiation Medium (PromoCell) treated with vehicle (DMSO), free GANT58, Empty-NPs, or GANT58-NPs. Cells were cultured for 14 days and media was changed every third day. A cohort of wells remained in MSC Growth Media and served as a control. Cells were then washed with PBS and fixed in 10% formalin for 45 min, and stained with Alizarin Red S (80 mM) for 30 min. After staining, cells were washed five times with deionized (DI) water and imaged under an inverted microscope.

Alizarin dye was then extracted with 5% SDS for 1 hr. Absorbance of the extracted dye was read on a plate reader at OD 405 nm.

Osteoclastogenesis assay

Mouse bone marrow-derived stromal cells were obtained from C57BL/6J mice and used in an osteoclastogenesis coculture assay as previously described [118, 119]. Briefly, femora and tibiae were dissected, and both ends cut off. Bone marrow cells were flushed out and collected via centrifugation, suspended in α-MEM with 10% FBS, and plated in 100 mm culture dishes. After 2 hr, nonadherent cells were harvested and pelleted. The non-adherent bone marrow cells (500,000 cells/well) and MDA-MB-231-bone cells supplemented with 10 ng/mL TGF-β (1000 cells/well) were plated in 48-well plates in 300 μL α-MEM (day 1). Treatments with Free GANT58, Empty-NPs, and GANT58-NPs started on day 1. On day 2, 300 μL of fresh α-MEM supplemented with treatments was added to each well, and 300 μL was replaced with fresh, treatment supplemented media each subsequent day until fixation. On day 6, cells were fixed and stained for TRAP using a TRAP kit (Sigma) and counterstained with hematoxylin. TRAP-positive cells with 3 or more nuclei were counted as osteoclasts. Vitamin D3 was used as a positive control for osteoclast formation, whereas absence of MDA-MB-231-bone cells and vitamin D3 was used as a negative control.

NP cargo biodistribution

Athymic female nude mice (4-6 weeks old, Envigo) were intratibially inoculated with GFP-expressing MDA-MB-231-bone tumor cells and given 14 days to progress into tumors. Two independent experiments were performed to assess the biodistribution of the NP cargo and of the

NP polymer. For biodistribution of the NP cargo, the near-IR fluorophore Cy7 was loaded into the NP formulation via the bulk solvent evaporation method to serve as the surrogate fluorescent loading species. Cy7-loaded NPs were then injected via tail vein injection (1 mg/kg Cy7). Mice were then imaged on a Pearl Near-IR imager (Licor) immediately, 2 hr, 6 hr, and 24 hr after injection and the images analyzed using region of interest (ROI) analysis in the Licor software. For biodistribution of the NP polymer, Cy7-grafted GANT58-NPs were injected via tail vein injection (8 mg/kg GANT58). Mice were then sacrificed at 1, 4, and 24 hr post NP-injection. Organs and long bones were imaged on a Pearl Near-IR imager (Licor) and the images analyzed using ROI analysis in the Licor software.

Pharmacokinetics

Rag 2-/- mice were injected with Cy5-grafted GANT58-NPs via retroorbital injection (8 mg/kg GANT58, 100 µL injection) under isoflurane anesthesia. Immediately post-injection, 15 min, 30 min, 1 hr, 2 hr, 4 hr, 12 hr, and 24 hr, a small volume of blood (< 5 µL) was drawn via tail-nick into a heparinized capillary tube and deposited into PCR tubes. PCR tubes containing whole blood samples were then frozen until analysis. Blood samples were thawed at time of analysis and diluted 40x in PBS. Samples were then read on a Take3 microvolume plate (Biotek) and a Synergy H1 fluorescence plate reader (Biotek) and background fluorescence was subtracted. NP concentration was calculated via a standard curve made by doping Cy5-grafted NPs into fresh mouse blood that was then frozen until time of analysis, at which time it was also diluted 40x [120].

Free GANT58 intratibial mouse model of late bone metastasis

Athymic female nude mice (4-6 weeks old, Harlan) were injected with 2.5 x 10^5 GFP-expressing MDA-MB-231-bone cells in 10 µL PBS into the left tibia under isoflurane anesthesia as previously described [121]. As a control, the contralateral limb was injected with 10 µL PBS. GANT58 was reconstituted in a 4:1 Cremophor EL:ethanol solution to solubilize the drug. GANT58 treatments started 4 days post-tumor inoculation to allow for tumor establishment (n = 8, GANT58; n = 8, vehicle). Mice were then treated 3 days/week with 50 mg/kg GANT58 via subcutaneous, 100 µL injection. Mice were imaged weekly to track tumor progression and sacrificed at 4 weeks.

GANT58-NP intratibial mouse model of late bone metastasis

Athymic female nude mice (4-6 weeks old, Envigo) were injected with 2.5 x 10^5 GFP-expressing MDA-MB-231-bone or RWGT2-bone cells in 10 µL PBS into the left tibia under isoflurane anesthesia as previously described [121]. As a control, the contralateral limb was injected with 10 µL PBS. GANT58-NP and Empty-NP treatment started 4 days post-tumor inoculation to allow for tumor establishment (n = 12, GANT58-NP; n = 12, Empty-NP). Mice were then treated 5 days/week with 8 mg/kg GANT58 in the GANT58-NP formulation or an equivalent polymer dose of Empty-NPs in 100 µL of PBS via tail vein injection. Mice were imaged weekly to track tumor progression and sacrificed at 4 weeks or 6 weeks post-tumor injection for the MDA-MB-231 and RWGT2 experiments, respectively.

GANT58-NP intracardiac mouse model of early bone metastasis

Athymic female nude mice (4-6 weeks old, Envigo) were anesthetized by continuous isoflurane and inoculated with 1 x 10^5 GFP-expressing MDA-MB-231-bone cells resuspended in

PBS via intracardiac injection into the left cardiac ventricle using a 27-gauge needle, as previously described [26, 28, 121]. Mice were then divided into two cohorts: one group which was treated immediately post-tumor inoculation with GANT58-NPs (8 mg/kg, n = 12) or Empty-NPs (equivalent polymer dose, n = 12), and the remaining group started the same treatment 7 days post-tumor inoculation. Mice were imaged weekly to track tumor progression and sacrificed at 4 weeks.

Radiographic imaging

Mice were radiographically imaged weekly beginning 1-week post-tumor cell inoculation using a Faxitron LX-60. Specifically, mice were anesthetized with isoflurane and laid in a prone position on the imaging platform. Images were acquired at 35 kVp for 8 seconds. Using a freehand selection tool, osteolytic lesions in each image were manually outlined and total lesion area and number were measured using the quantitative image analysis software Metamorph (Molecular Devices, Inc.). All data are represented as mean lesion area and number per mouse.

Micro-computed tomography (μCT)

Tibiae and femora were analyzed using a high-resolution benchtop μCT 40 system (Scanco Medical). Tomographic images were acquired at 70 kVp with an isotropic voxel size of 12 μm and at an integration time of 300 ms. Scans were acquired with hindlimbs in 70% ethanol. μCT images were reconstructed, filtered (σ = 0.2, support = 1.0) and thresholded at 230. Tibiae and femora were then contoured using the Scanco software algorithm starting 10 slices below the growth plate and continued 100 slices in the distal direction. Images were then reconstructed using the Scanco Medical Imaging software. The software was also used to calculate the bone morphometric parameters bone volume/total volume (BV/TV, ratio of segmented bone volume to the total

volume of interest), trabecular separation (Tb.Sp., mean distance between trabeculae), trabecular thickness (Tb.Th., mean thickness of trabeculae), and trabecular number (Tb.N., measure of the average number of trabeculae per unit length) of the segmented bone.

Histology/histomorphometry

Tibiae and femora were removed during autopsy and fixed in 10% neutral-buffered formalin (Fisher Scientific) for 48 hr at room temperature after which they were stored at 4ºC in 70% ethanol. Bone specimens were decalcified in 10% EDTA for 2 weeks at 4°C and embedded in paraffin wax. Bone sections (5-μm thickness) were stained with hematoxylin & eosin (H&E), orange G, and phloxine. Tumor burden was examined under a microscope and quantified using Metamorph software (Molecular Devices, Inc.). Specifically, tumors were manually outlined as ROIs using a freehand selection tool and the total tumor area was measured as a percentage of the total bone marrow area.

The rabbit anti-PTHrP antibody (1:2500, R87, generated against PTHrP (amino acids 1-34)) was a gift from Drs. T.J. Martin (St. Vincent's Institute of Medical Research, Australia) and Natalie Sims (The University of Melbourne, Australia). Immunohistochemistry (IHC) was carried out on decalcified paraffin-embedded tibial and femoral sections as previously described [122, 123]. PTHrP-positive staining was quantified using Metamorph software (Molecular Devices, Inc.).

Ethics statement

All animal protocols were approved by Vanderbilt University Institutional Animal Care and Use Committee (IACUC) and were conducted according to National Institutes of Health (NIH) guidelines for care and use of laboratory animals.

Statistical analyses

All statistical analyses were performed using Prism version 7 (GraphPad Software, Inc.). Values are presented as mean ± SEM and p-values determined using one-way ANOVA unless otherwise specified where *$p < 0.05$, **$p < 0.01$, ***$p < 0.001$, and ****$p < 0.0001$.

3.4 Results

Gli2 is overexpressed in bone metastatic patient tumors

Our previous data have established that Gli2 regulates PTHrP expression and is strongly correlated with bone-destructive tumor cells [26, 28]. To test our hypothesis that Gli2 is overexpressed in patients with bone metastases, we collected 20 human biopsies through the CHTN (**Table S3.1**) and evaluated Gli2 expression in bone-metastatic tumors from a mix of primary origins. Three of the 20 biopsies were from non-metastatic soft tissue sarcomas and were tested as controls. Patient bone metastases expressed significantly higher levels of Gli2 by IHC compared to soft tissue sarcomas (6-fold increase) (**Fig. 3.1A-B**). To further show that Gli2 is overexpressed in bone metastases, we queried the GEO database to obtain Gli2 expression values among 29 human breast cancer metastases in different organs [116]. Gli2 gene expression was significantly higher in bone metastases compared to brain and lung metastases from breast cancer patients (**Fig. 3.1C**). Together, these observations suggest that the expression of Gli2 correlates with tumors that reside in bone, suggesting that Gli2 inhibitors may be a strategy to reduce TIBD.

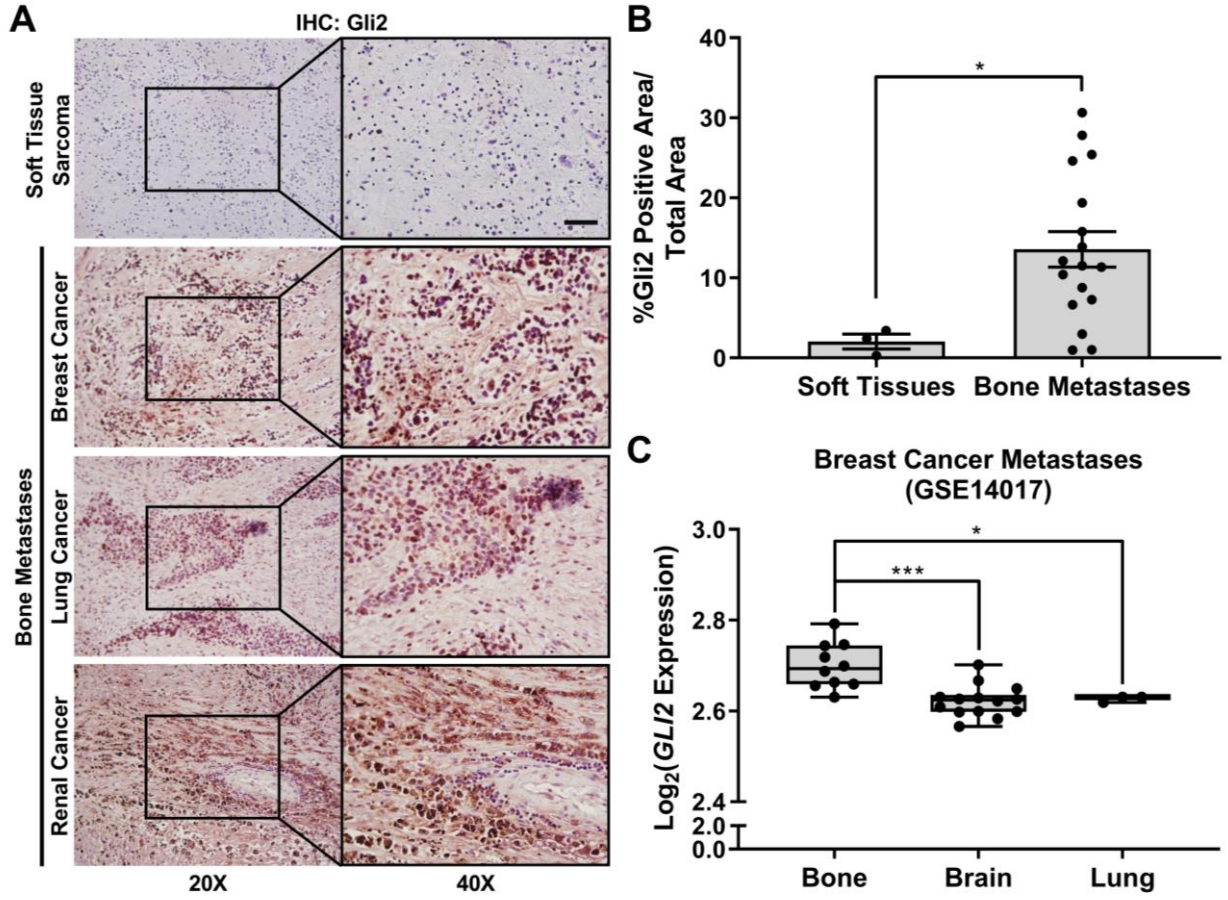

Fig. 3.1. Gli2 is overexpressed in patient bone-metastatic tumors. (A) Representative images of Gli2 IHC for patient soft tissue sarcomas (n = 3) and bone-metastatic tumors (n = 17) from different primary origins. Scale bar: 50 µm. (B) Quantification of Gli2-stained patient tumor samples. Groups were statistically compared using student's unpaired t-test. (C) Gli2 gene expression in human breast cancer metastases from bone (n = 10), brain (n = 14), and lung (n = 3). Minima = 25th percentile, maxima = 75th percentile, centers = median.

Free GANT58 does not reduce tumor growth or bone destruction

Since previous studies using subcutaneous tumors showed efficacy of GANT58 for reducing prostate tumor growth [35], we tested the efficacy of this approach in models of TIBD. Based on this study and other studies using poorly-water soluble drugs such as paclitaxel [124], we used a 4:1 Cremophor EL:ethanol mix for delivery. Athymic nude mice were inoculated with MDA-MB-231 cells into the left tibiae and were then treated 3 days/week with 50 mg/kg GANT58 or vehicle control via subcutaneous injection (**Fig. 3.2A**).

Radiographic imaging of the mice over the course of the study showed that by week 3 both the GANT58 and vehicle-treated groups exhibited severe osteolytic lesions, which significantly worsened by week 4, at which time the mice were sacrificed. Further, the mice showed an adverse response to the injections, presenting with necrosis at the drug injection site as early as week 2 (Division of Animal Care was consulted and necessary treatment provided). Radiographic analysis showed that there was no significant difference between GANT58 and control mice in lesion area or lesion number, with both groups exhibiting numerous lesions in the tumor-bearing tibia (**Fig.**

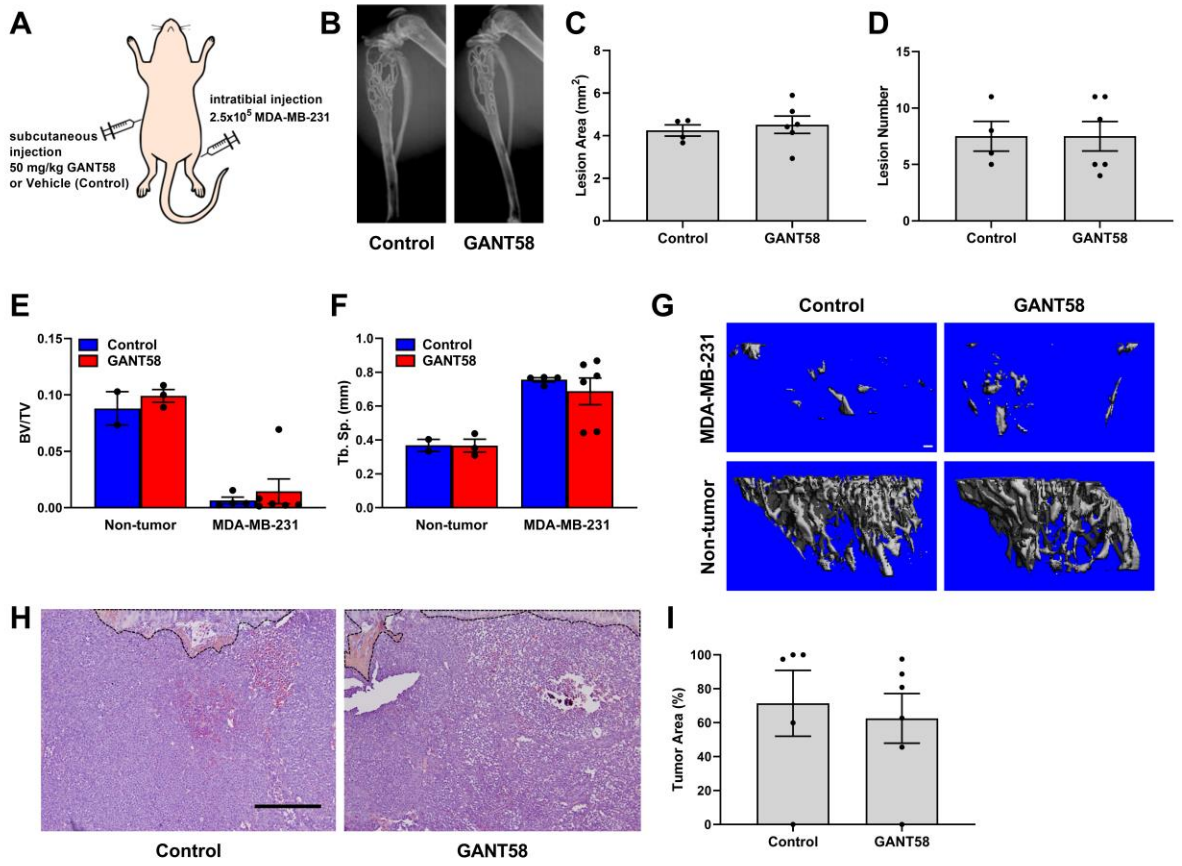

Fig. 3.2. GANT58 treatment does not block tumor-induced osteolysis when delivered via Cremophor EL vehicle. (A) Tumor inoculation and subcutaneous treatment scheme for intratibial model of bone metastasis. (B) Representative radiographic images of vehicle (control) and GANT58 treated mice at 4-weeks post-tumor (MDA-MB-231) inoculation. Osteolytic bone lesions are outlined in white. (C) Lesion area and (D) lesion number as assessed by radiographic analysis exhibit no significant difference between vehicle and treatment groups. (E & F) µCT analysis of tibiae bone volume fraction (BV/TV) and trabecular separation (Tb. Sp.) showed no significant difference in mice treated with GANT58 versus those treated with Cremophor EL vehicle. (G) Representative µCT reconstructions of vehicle-treated, GANT58-treated, and contralateral, non-tumor bearing tibiae. (H) Representative H&E stained sections and (I) histomorphometric analysis of tumor area in vehicle-treated and GANT58-treated mice inoculated with MDA-MB-231 cells. Growth plate and remaining trabecular bone outlined in black. Scale bar: 200 µm.

3.2B-D). To further investigate the bone outcomes in these mice, μCT was conducted on the tibiae after sacrifice. BV/TV was significantly reduced in all tumor bearing animals and was comparable for vehicle- and GANT58-treated tumor-bearing tibiae (**Fig. 3.2E**). Similarly, Tb.Sp. was comparable for vehicle-and GANT58-treated tumor-bearing tibiae and both were significantly higher than the non-tumor controls (**Fig. 3.2F-G**). Histological analysis showed that in both treated and control mice, the average tumor area (%) measured by histomorphometry was 60-70%, indicating that tumor had effectively invaded the entire marrow space of the tibia (**Fig. 3.2H-I**). These findings demonstrate that delivery of free GANT58 at high doses using standard clinical formulation techniques is not well-tolerated by the animals and is not effective at blocking TIBD, highlighting the need for delivery strategies that solubilize the drug and improve its PK profile to enable bone tumor delivery.

Synthesis of PPS_{135}-b-$POEGA_{17}$ diblock copolymer

In order to improve drug solubility and potentially improve efficacy of GANT58, a diblock copolymer comprising PPS and POEGA was synthesized via RAFT polymerization (**Fig. 3.3A, Fig. S3.1A-B**). PPS was chosen as the core-forming hydrophobic block primarily due to its promise from other studies in our lab that showed excellent encapsulation and retention of hydrophobic small molecules [106, 114, 125]. Furthermore, the sulfide group in PPS reacts with oxygen radicals to create sulfoxides and sulfones. This reaction causes a hydrophobic to hydrophilic phase transition in the polymer which potentially contributes to both drug release at sites of oxidative stress and ultimate systemic clearance of the polymer through a renal route. Previous studies have also reported that PPS is a potent reactive oxygen species (ROS)-scavenger, which is hypothesized to impart beneficial antioxidant properties to the GANT58-NPs [126, 127].

The POEGA hydrophilic block forms a brush-like conformation of 9 repeating units of ethylene glycol pendant to the hydrocarbon backbone. POEGA was chosen as the NP surface-forming block because this graft polymer architecture has been shown to improve circulation time over linear PEG [128-130].

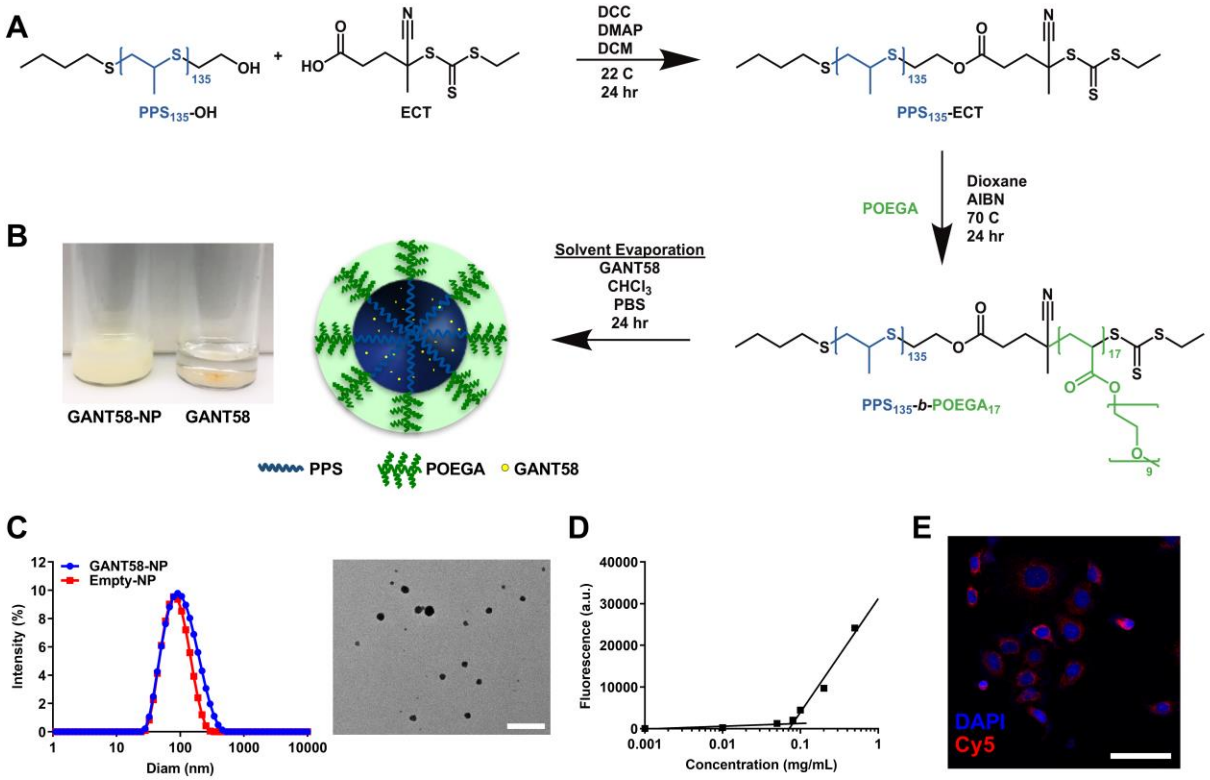

Fig. 3.3. GANT58-NP fabrication and characterization. (A) Synthesis of PPS_{135}-b-$POEGA_{17}$ polymer and nanoparticle fabrication. (B) GANT58-NPs (2 mg/mL GANT58) are dispersed in PBS while insoluble free GANT58 (2 mg/mL) precipitates from solution. (C) Particle size distribution of GANT58-NPs and Empty-NPs measured by dynamic light scattering (DLS) indicate that both loaded and unloaded formulations have an average diameter < 100 nm. A TEM image (right) reveals the spherical morphology of GANT58-NPs. Scale bar: 500 nm. (D) Critical micelle concentration (CMC) determined by Nile red assay. (E) Fluorescence microscopy image of MDA-MB-231-bone cells after 3 hr treatment with Cy5-labeled GANT58-NPs indicating significant NP uptake into the tumor cells.

Nanoparticle Preparation and Characterization

Nanoparticles were formed by the bulk solvent evaporation method to create either GANT58-loaded PPS_{135}-*b*-$POEGA_{17}$ nanoparticles (GANT58-NPs) or unloaded PPS_{135}-*b*-$POEGA_{17}$ nanoparticles (Empty-NP) (**Fig. 3.3B**). GANT58 (**Fig. S3.1C**) was introduced into the

organic phase resulting in an average loading content of 11.4% (mg drug/mg polymer) and an encapsulation efficiency of 51.8%. The hydrodynamic diameter of both the GANT58-NPs and Empty-NPs were assessed by DLS. The GANT58-NPs have an average hydrodynamic diameter of 93.3 ± 4.1 nm, while the Empty-NPs have a slightly smaller diameter of 73.5 ± 3.4 nm. TEM shows the NPs exhibit a spherical morphology (**Fig. 3.3C**). Both the GANT58-NPs and Empty-NPs were monodispersed with an average PDI of 0.22 and 0.18, respectively, and a relatively low ζ-potential (-1.33 mV and -1.20 mV, respectively). The critical micelle concentration (CMC) of the GANT58-NPs was 0.079 mg/mL as determined by the Nile Red (NR) method (**Fig. 3.3D**) [105]. This CMC is almost an order of magnitude lower than the initial NP concentration after i.v. administration (~0.5 mg/mL) and remains lower than the NP blood concentration after 12 hr of circulation (~0.15 mg/mL) as indicated by circulation time measurements. Since tumor cells have high levels of ROS [131], this particle chemistry was chosen to be released at higher ROS concentrations (such as the tumor) as previously described [114, 125]. To confirm ROS-responsiveness of the NPs which have previously been characterized by our group [132], we performed *in vitro* studies using H_2O_2 as the model ROS species and NR-loaded NPs (**Fig. S3.2**). Incubation of Cy5-labeled GANT58-NPs with MDA-MB-231-bone cells revealed that cells readily uptake the NPs. The Cy5-labeled NPs (red) exhibit close proximity to DAPI-stained nuclei (blue), indicating uptake of the NPs within the cells (**Fig. 3.3E**).

GANT58-NPs block Gli2 nuclear translocation

The authors of the manuscript on the original drug screen that identified GANT58 hypothesized that it primarily acts at the nuclear level [35], but the molecular mechanism has not been reported. To test the hypothesis that GANT58 inhibits nuclear translocation of Gli2, MDA-

MB-231-bone cells were treated with 20 μM GANT58 or GANT58-NP for 72 hr. Immunofluorescent analyses revealed significantly reduced colocalization of Gli2 with DAPI-stained nuclei in cells treated with GANT58 or GANT58-NPs compared to the Empty-NP control (**Fig. 3.4A**). Additionally, MDA-MB-231-bone cells treated with increasing concentrations of free GANT58 or GANT58-NPs showed reduced nuclear Gli2 protein levels as shown by immunoblotting (**Fig. 3.4B**). Nuclear protein levels of Gli2 in cells treated with 20 μM GANT58

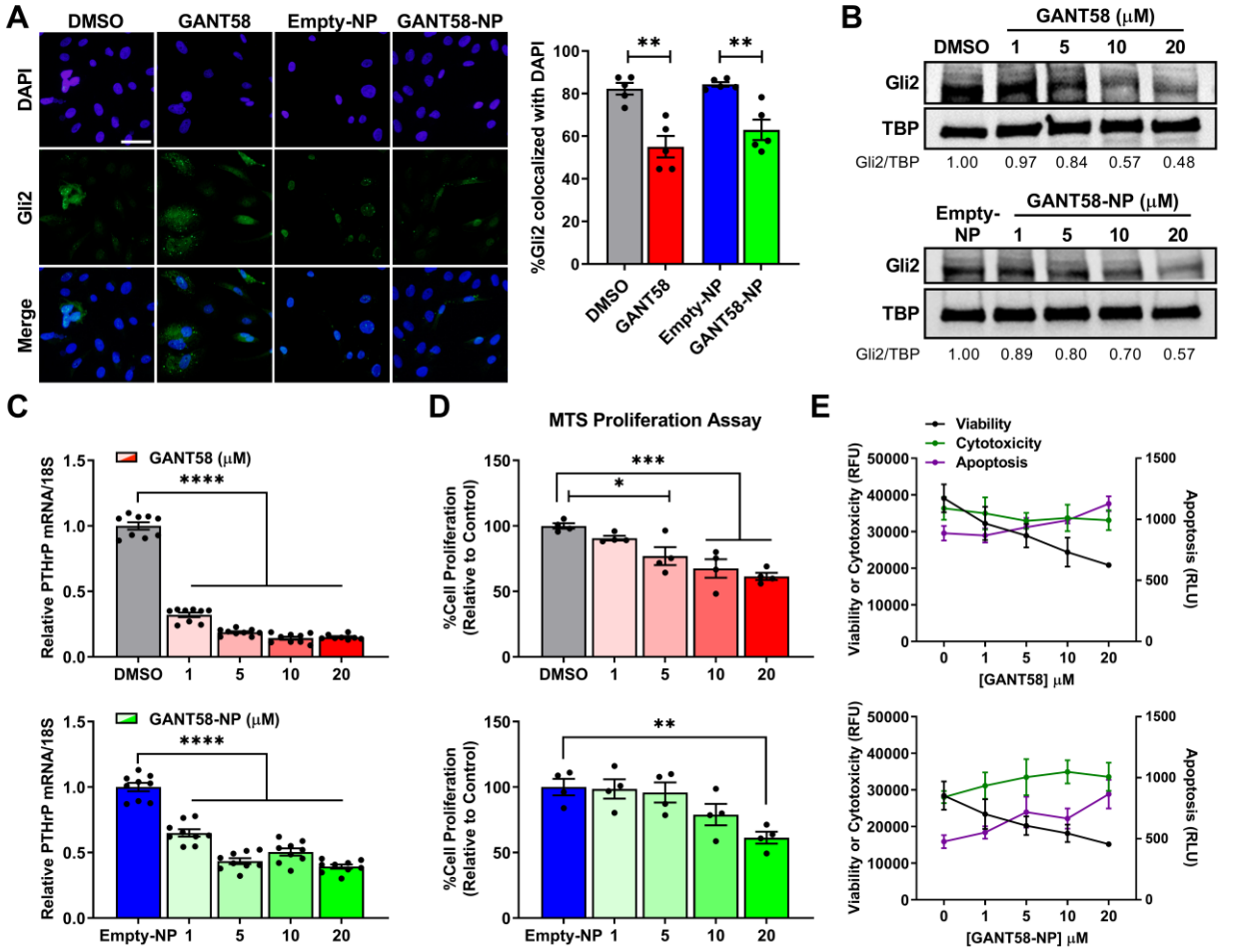

Fig. 3.4. GANT58-NP treatment inhibits nuclear translocation of Gli2 and tumor cell proliferation. (A) Representative immunofluorescent images of Gli2 nuclear translocation *(left)* with quantification as measured by the Manders coefficient *(right)* after treatment with 20 μM GANT58 or GANT58-NP for 72 hr. Scale bar: 50 μm. (B) Nuclear Gli2 protein levels in MDA-MB-231-bone cells at 72 hr. (C) Expression of PTHrP mRNA for MDA-MB-231-bone cells treated with varying concentrations of free GANT58 (red), Empty-NP (blue), or GANT58-NP (green) for 48 hr. Gradient colors indicate varying doses: 1 μM (transparent), 5 μM, 10 μM, to 20 μM (opaque). (D) Tumor cell proliferation as assessed by MTS assay after 24 hr treatment with free GANT58 or GANT58-NPs (same dosage scheme as (C)). (E) Viability, cytotoxicity, and apoptosis of MDA-MB-231-bone cells treated with free GANT58 or GANT58-NPs for 24 hr measured by ApoTox-Glo assay. Four technical replicates from a single experiment are shown in (D) and (E).

or GANT58-NP was 48% and 57% of the control, respectively. Inhibition of Gli2 nuclear translocation by GANT58 also significantly reduced PTHrP mRNA levels (**Fig. 3.4C**). In contrast, Gli2 protein levels in the cytoplasm did not decrease in a dose-dependent manner following treatment with GANT58 or GANT58-NP, but cytoplasmic Gli2 protein levels were reduced (67 - 69% of the control) at the highest GANT58 dose tested (20 μM) (**Fig. S3.3**). These findings show that GANT58 blocks translocation of Gli2 into the nucleus and consequent transcription of PTHrP.

GANT58-NPs reduce tumor cell proliferation and induce apoptosis

To determine the effect of GANT58-NPs on tumor cell proliferation and viability, MDA-MB-231-bone cells treated with increasing drug concentrations were cultured for 24 hr. Cell proliferation assessed by MTS assay demonstrated that treatment with GANT58 or GANT58-NP significantly reduced tumor cell growth rate *in vitro* (**Fig. 3.4D**). GANT58 and GANT58-NP also reduced cell viability and increased activation of caspase 3/7 (which is indicative of apoptosis) compared to vehicle-treated cells in the ApoTox-Glo assay (**Fig. 3.4E**).

GANT58-NPs do not alter mesenchymal stem cell proliferation

The effect of GANT58-NPs on hMSC proliferation and osteoblast differentiation was assessed to ensure that GANT58-NPs do not negatively impact osteoblast function and behavior. Proliferation (assessed by MTS assay) was not significantly affected by free GANT58, Empty-NPs, or GANT58-NPs at concentrations up to 20 μM (**Fig. 3.5A**). Deposition of mineralized matrix by osteoblasts was assessed via Alizarin Red stain after 14 d culture in osteogenic media. Neither the DMSO vehicle nor free GANT58 significantly reduced Alizarin red staining compared to no treatment, and NP treatment had no negative effects on osteoblast mineralization (**Fig. 3.5B**).

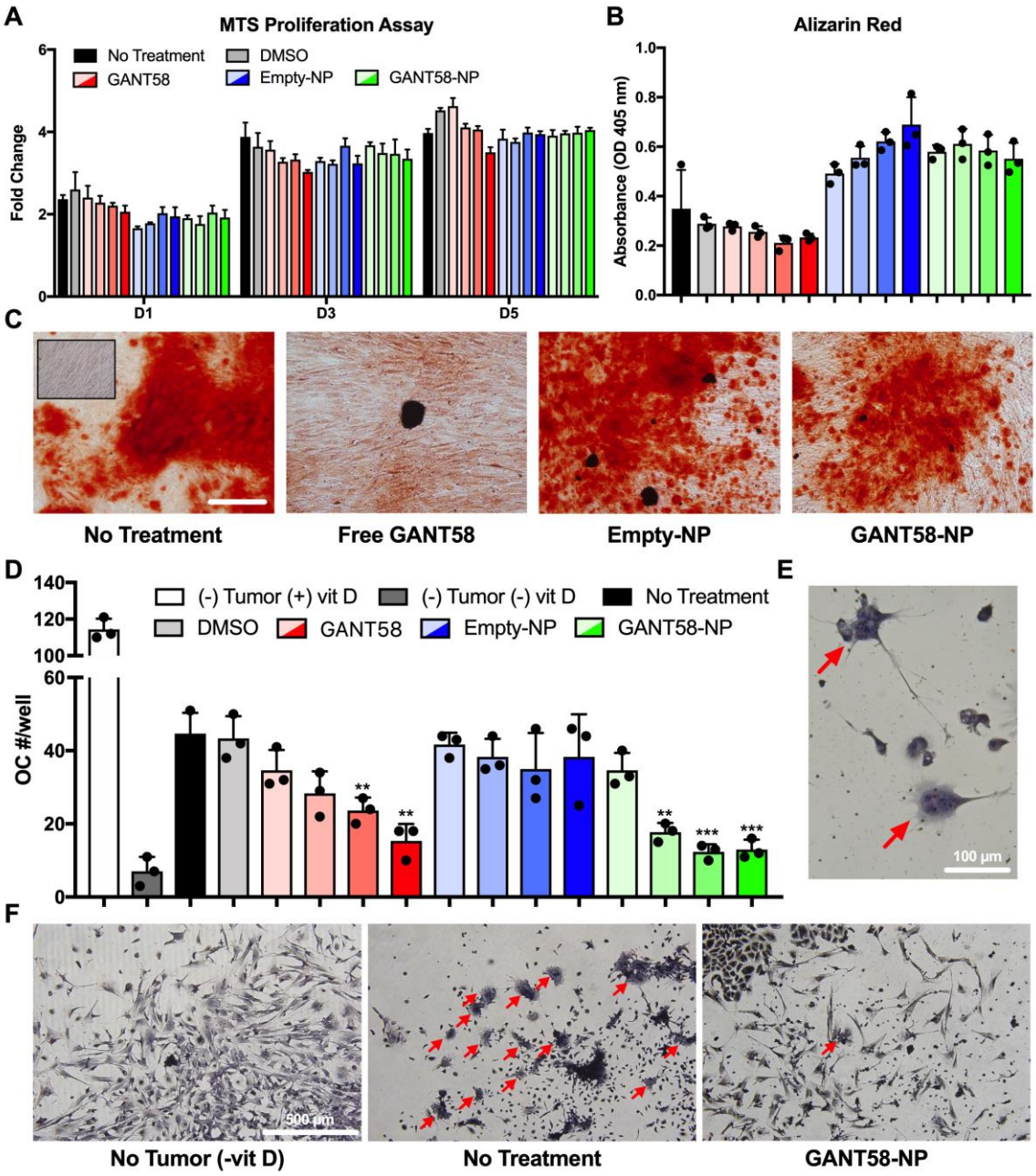

Fig. 3.5. GANT58-NP treatment does not inhibit osteoblast function but reduces tumor-mediated osteoclastogenesis *in vitro*. (A) hMSCs treated with varying concentrations of free GANT58 (red), Empty-NP (blue), or GANT58-NP (green) were cultured for 1, 3, and 5 days (D1, D3, D5) and proliferation assessed by MTS assay. Gradient colors indicate varying doses: 1 µM (transparent), 5 µM, 10 µM, to 20 µM (opaque). (B) hMSCs were cultured in osteogenic medium treated with same dosage scheme described in (A). Deposition of mineralized matrix by osteoblasts was determined by absorbance of extracted Alizarin Red stain after 14 d of culture in osteogenic media. (C) Representative images of Alizarin Red staining of treated osteoblasts after 14 d culture in osteogenic media. Inset image shows hMSCs cultured in non-osteogenic media. Scale bar: 200 µm. (D) Number of osteoclasts (OC)/well in coculture treated with varying doses of GANT58, Empty-NP, and GANT58-NP after 6 days culture with MDA-MB-231 cells. Three technical replicates are shown in (A), (B), and (D) from single experiments. (E) Multinucleated (3 or more nuclei) and TRAP positive cells were counted as OCs. Red arrows: OCs. (F) Representative images of negative control group (no tumor, -vitD), no treatment group, and 20 µM GANT58-NP treatment group. Red arrows: OCs.

Representative images of the Alizarin Red-stained cells show the deposition of mineralized matrix by the NP-treated osteoblasts (**Fig. 3.5C**).

While GANT58 is an antagonist of Gli2 within tumor cells, its functional effect is to reduce secretion of PTHrP protein, which stimulates osteoblasts to express RANKL, a transmembrane protein that stimulates osteoclast differentiation. In order to investigate the effect of GANT58-NPs on osteoclast differentiation, an osteoclastogenesis assay utilizing a coculture of mouse bone marrow-derived stromal cells and MDA-MB-231 cells was performed. Osteoclast number was counted after 7 d culture in the presence of free GANT58, Empty-NP, and GANT58-NP via TRAP stain (**Fig. 3.5D**). Osteoclasts were counted at 40x magnification and identified as TRAP+ (red/pink stain), multinucleated (≥ 3 nuclei) cells (**Fig. 3.5E**). Osteoclast number showed a GANT58 dose-dependent decrease in osteoclasts for both the free GANT58 and GANT58-NP, while the Empty-NP had no effect on osteoclastogenesis. Representative 10x magnification images of the coculture show very few osteoclasts in the (-) vitamin D negative control and 20 μM GANT58-NP group, whereas the untreated tumor group exhibited extensive osteoclast maturation (**Fig. 3.5F**).

GANT58-NPs distribute to the tumor bearing bones

After validation of *in vitro* efficacy, the biodistribution and pharmacokinetics (PK) of the PPS_{135}-b-$POEGA_{17}$ NPs and its cargo was evaluated via near-IR fluorescent dye grafting and loading (for NP and cargo tracking, respectively) of the micelles. First, Cy7 fluorophore-loaded PPS_{135}-b-$POEGA_{17}$ NPs (Cy7-NPs) were administered via i.v. tail vein injection to tibial tumor-bearing athymic nude mice to evaluate NP cargo biodistribution and PK of in tumor and organs of interest. Cy7 was chosen as the surrogate compound for GANT58 due to its strong near-IR

fluorescence and solubility properties similar to that of GANT58 (logP = 3.4 and 3.9, respectively). *In vivo* biodistribution was assessed in mice over time to observe Cy7 cargo localization in the tumor-bearing tibia site versus control tibia (**Fig. 3.6A**). Near-IR *in vivo* imaging and Pearl image analysis software were used to quantify Cy7 fluorescence intensity in both the tumor and control ROI. Cy7 fluorescence intensity was significantly higher in the tumor-bearing tibia at each time point, indicating that the Cy7 cargo was preferentially localizing in the tumor bearing site.

Next, Cy7-grafted GANT58-NPs (GANT58-Cy7NPs) were administered via tail vein injection to track GANT58-Cy7NP biodistribution over time. Mice were sacrificed at predetermined time points, and Cy7 fluorescence was measured in organs of interest *ex vivo*. At 24 hr post-injection, the tumor-bearing left hindlimb (LHL) had significantly increased uptake over the other long bones, while the liver had the highest intensity as expected due to clearance by the mononuclear phagocyte system (MPS). The kidneys had the next highest level of fluorescence, potentially serving as a route for clearance of the Cy7-grafted polymer following NP disassembly (**Fig. 3.6B**). Cy7 fluorescence steadily decreased over time in all long bones aside from the tumor-bearing hindlimb, indicating stable accumulation in the bone-tumor site (**Fig. 3.6C**). Similarly, there was a steady decrease in Cy7 fluorescence in all organs aside from liver and kidney, where there was an expected increase in intensity as the NPs were cleared from circulation (**Fig. 3.6C-D**). To further validate the findings that the NPs are preferentially accumulating in the tumor, GFP intensity from the MDA-MB-231 cells was measured and spatially compared to the Cy7 fluorescence (**Fig. 3.6E**). A strong colocalization was observed, suggesting the NP polymer accumulation is primarily within the tumor site.

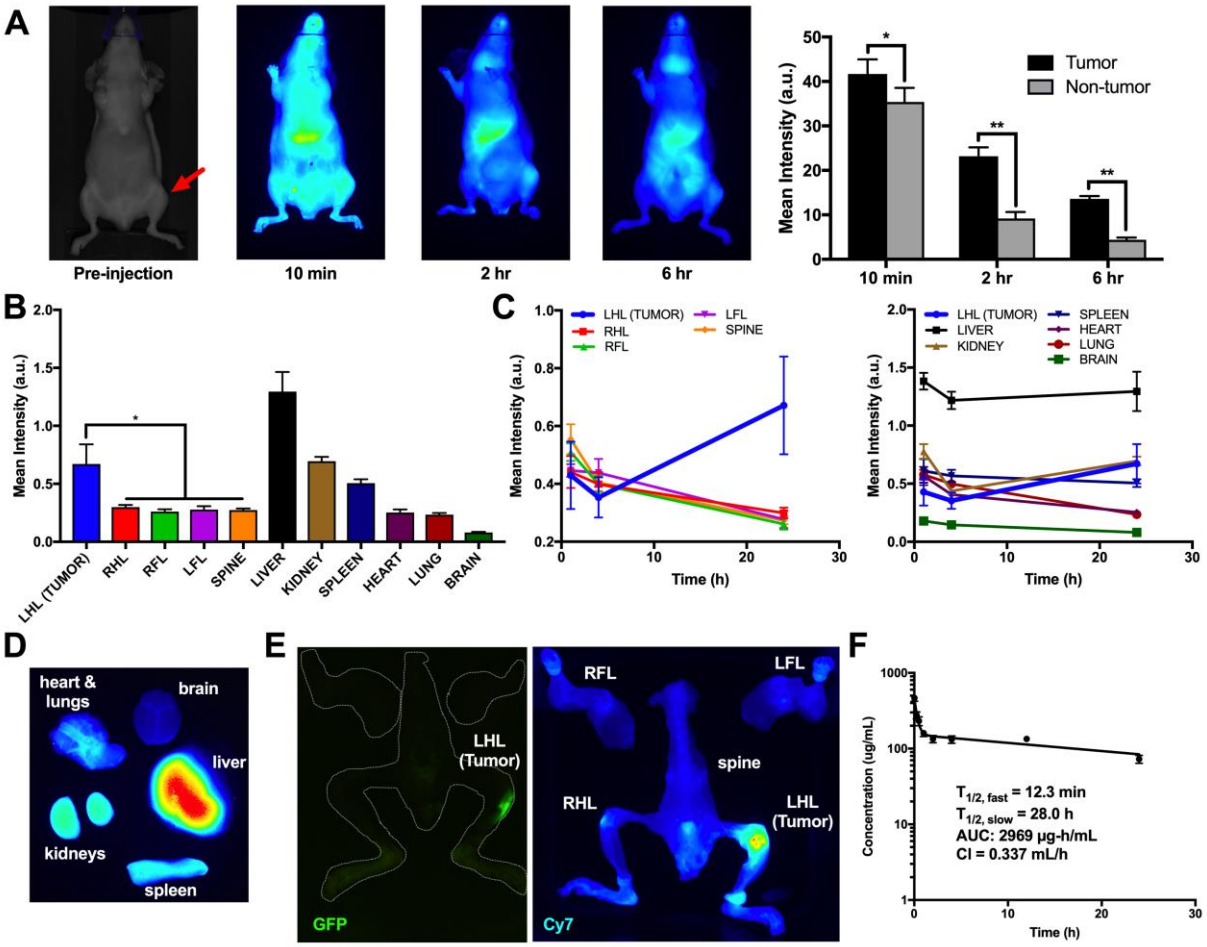

Fig. 3.6. GANT58-NPs accumulate in tumor and demonstrate prolonged blood circulation. (A) Cy7-loaded NPs (Cy7-NPs) time course biodistribution in tumor-bearing mice. Cy7 fluorescence is significantly higher in the tumor-bearing tibia (red arrow) compared to the contralateral control. (B) Cy7-grafted GANT58-NPs biodistribution *ex vivo* analysis at 24 hr shows significantly higher Cy7 fluorescence in the tumor-bearing hindlimb compared to other long bones. L(R)HL = left (right) hindlimb; L(R)FL = left (right) forelimb. (C) Time-course *ex vivo* analysis of Cy7-grafted GANT58-NPs shows that NPs increasingly accumulate in tumor over 24 hr period. (D) Representative organ Cy7 fluorescence at 24 hr post-NP injection. (E) GFP imaging (tumor) and Cy7 fluorescence (NP) confirm colocalization of NPs within the tumor site. (F) Circulation time of Cy5-grafted GANT58-NPs as assessed by tail nick method.

The PK profile of the GANT58-NPs was next investigated by measuring the blood circulation time of Cy5-grafted GANT58-NPs (GANT58-Cy5NPs). The findings from the biodistribution study suggested a significant concentration of NPs are still in circulation after 12 hr due to the increased NP polymer accumulation in tumor, liver, and kidneys at the 24 hr time point. We designed the circulation time experiment to encompass both short (< 30 min) and long (> 12 hr) time periods for accurate measurement of the α and β phase circulation half-lives. After

retroorbital injection of the GANT58-Cy5NPs, a tail nick method was used to draw small volumes (< 5 μL) of blood immediately post-injection (t=0) and at subsequent predetermined intervals up to 24 hr. These small blood volumes were then measured for Cy5 fluorescence intensity on a micro-volume plate using a fluorescence plate reader and NP concentration calculated from a standard curve. A rapid α-phase distributive half-life of 12.3 min was observed, after which there was a more gradual β-phase with a 28 hr half-life (**Fig. 3.6F**). Even after 24 hr, roughly 15% of the initial NP dose was still in circulation, which supports the biodistribution findings showing increased uptake in tumor and clearance organs at 24 hr.

GANT58-NPs reduce bone destruction in mouse model of established tumors in bone

The promising *in vitro* results and preferential uptake in the tumor site presented compelling evidence that GANT58-NPs would successfully block tumor-induced bone destruction *in vivo* and possibly reduce tumor burden. To test this hypothesis, MDA-MB-231-bone cells were inoculated into the left tibiae of female athymic nude mice. After 4 days to allow tumor establishment, mice were treated daily with GANT58-NPs (8 mg/kg GANT58) or Empty-NPs via tail vein injection (**Fig. 3.7A**). Empty-NPs were chosen as the control due to the *in vitro* results suggesting the positive effect the Empty-NPs may have on osteoblast differentiation.

Substantial osteolytic lesions were observed radiographically in the mice treated only with the Empty-NPs after 4 weeks, while smaller and fewer lesions were visible in mice treated with GANT58-NP (**Fig. 3.7B**). Quantitative assessment of both lesion area and number confirmed that the osteolytic lesions in the GANT58-NP-treated mice were significantly smaller and fewer (**Fig. 3.7C-D**).

After sacrifice, mouse tibiae were examined by µCT to assess the effects of the drug on bone morphometric properties. Mice treated with the GANT58-NPs had 2.5-fold higher ($p < 0.001$) BV/TV than those treated with Empty-NPs and 22% lower ($p < 0.05$) BV/TV than the treated, non-tumor bearing control (**Fig. 3.7E**). Tb.Sp. in the GANT58-NP group was 34% lower ($p < 0.05$) than the Empty-NP group and 48% higher ($p < 0.05$) than the untreated control (**Fig. 3.7F**). Similarly, trabecular number (Tb.N.) in the GANT58-NP group trended higher than the Empty-NP group and was 28% lower than the untreated control (**Fig. 3.7G**). 3D µCT renderings of

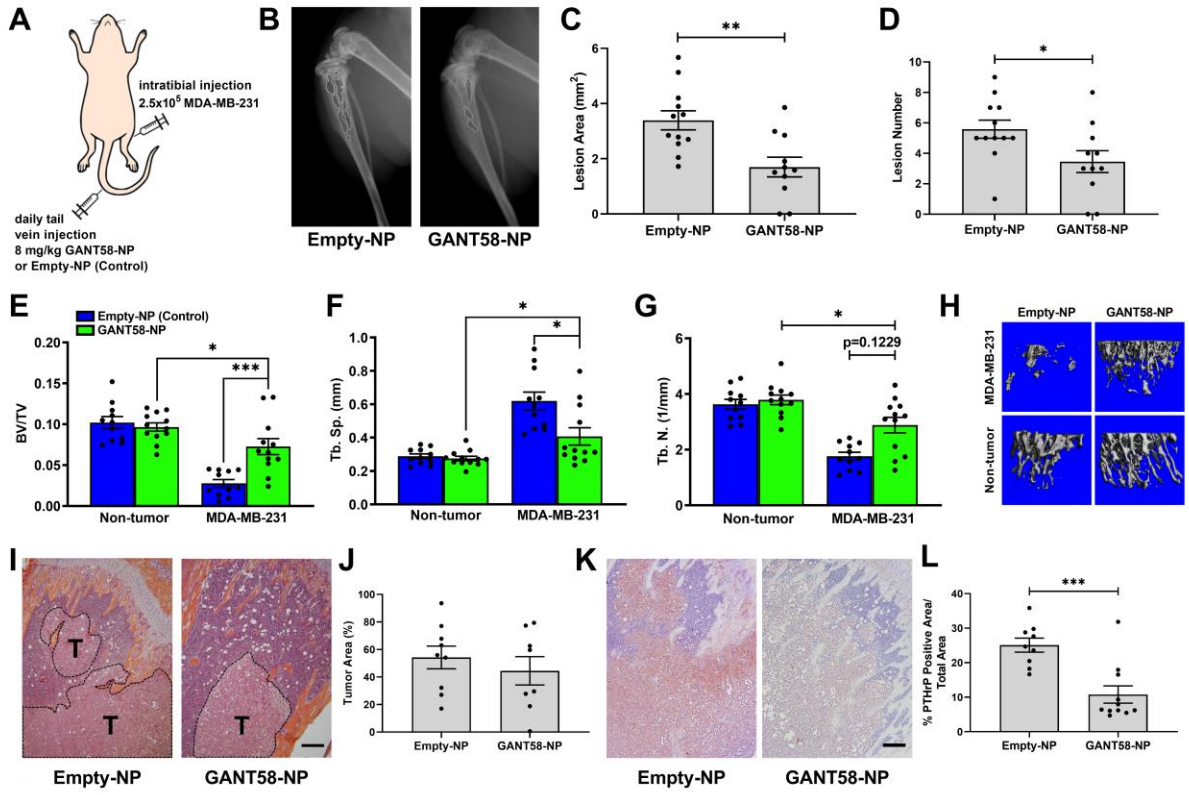

Fig. 3.7. GANT58-NP treatment reduces tumor-induced osteolysis in mouse model of late bone metastasis in multiple tumor cell lines. (A) Tumor-inoculation and treatment scheme for intratibial model of bone metastasis. (B) Representative radiographic images of Empty-NP (control) and GANT58-NP treated mice at 4-weeks post-tumor (MDA-MB-231) inoculation. Osteolytic bone lesions are outlined in white. (C) Lesion area and (D) lesion number as assessed by radiographic analysis are significantly reduced in GANT58-NP treated mice. (E-G) µCT analysis of tibiae bone volume fraction (BV/TV), trabecular separation (Tb. Sp.), and trabecular number (Tb. N.) showed significantly improved bone quality in mice treated with GANT58-NPs. (H) Representative µCT reconstructions of GANT58-NP-treated, Empty-NP-treated, and contralateral, non-tumor bearing tibiae. (I) Representative H&E stained sections and (J) histomorphometric analysis of tumor area (indicated by T) in Empty-NP-treated and GANT58-NP-treated in mice inoculated with MDA-MB-231 cells. Scale bar: 200 µm. (K) Representative images and (L) quantification of immunohistochemical staining for PTHrP (red-brown staining) in sections from Empty-NP-treated and GANT58-NP-treated tumor-bearing mice. Scale bar: 200 µm.

representative tibiae from each group further demonstrate the significant tumor-induced bone destruction in the mice treated with Empty-NPs compared to those treated with GANT58-NPs (**Fig. 3.7H**). Histomorphometric analysis of the tibiae showed no significant differences in tumor burden between groups (**Fig. 3.7I-J**); however, a significant reduction in PTHrP protein expression was detected by IHC in GANT58-NP-treated mice compared to those treated with Empty-NPs (**Fig. 3.7K-L**).

In order to establish the broader generalizability of these findings, another human osteolytic cancer cell line was tested in the same intratibial model. In this experiment, a bone-metastatic variant of a squamous non-small cell lung carcinoma line, RWGT2-bone, was used and the same bone outcomes were assessed. Again, radiograph analysis showed a significant reduction in lesion area and number in GANT58-NP-treated mice (**Fig. S3.4A**). BV/TV was also significantly higher in the mice treated with GANT58-NPs than those treated with Empty-NPs (**Fig. S3.4B**). Further, there was no significant difference in BV/TV in GANT58-NP-treated mice and the non-tumor-bearing control tibiae (**Fig. S3.4B**). Other morphometric parameters, however, were not significantly different between the GANT58-NP and Empty-NP groups (**Fig. S3.4C-E**). 3D μCT renderings of representative tibiae from each group again demonstrate the tumor-induced bone destruction in the mice treated with Empty-NPs compared to those treated with GANT58-NPs (**Fig. S3.4F**). It is important to note that the RWGT2-bone cell line was not as aggressive as the MDA-MB-231-bone line, as indicated by the higher BV/TV in the RWGT2-bone Empty-NP group compared to the same group in the MDA-MB-231-bone experiment. This lower tumor burden could explain the diminished significance in μCT outcomes for the GANT58-NP treatment group relative to controls for this study relative to the MDA-MB-231 study.

GANT58-NPs reduce TIBD in bone metastatic mouse model

The intratibial model of bone metastasis was informative in showing that GANT58 is effective in blocking bone destruction induced by established tumors, but its effect on tumor metastasis could not be elucidated using this model. Therefore, an intracardiac model of bone metastasis was used in order to investigate the effect of GANT58-NPs on blocking tumor metastasis in addition to bone destruction. In this experiment, mice were injected with MDA-MB-231 cells via intracardiac injection and were subsequently divided into two cohorts. The first cohort, denoted the "immediate" group, was immediately treated via tail vein injection with either GANT58-NPs (treatment) or Empty-NPs (control). The second cohort of mice, denoted the "delayed" group, was allowed 7 days for tumor establishment before starting treatment (**Fig. 3.8A**).

Tibiae and femurs were scanned by μCT after sacrifice, and subsequent observation of histological sections showed that tumor presence was more substantial in the femur than in the tibia. Thus, the femur was chosen for thorough μCT and histological analysis. μCT analysis revealed that there was significantly higher BV/TV and Tb. Th. in the mice that were treated with GANT58-NPs, indicating reduced bone destruction and improved bone quality in GANT58-NP-treated mice. However, there was no significant difference between the mice treated immediately and the mice that received delayed treatment (**Fig. 3.8B**). Histological analysis showed no significant reduction in tumor burden across all groups (**Fig. 3.8C**); however, a significant reduction in PTHrP expression was observed by IHC in tumor-bearing mice that were immediately treated with GANT58-NPs compared to control-treated mice (**Fig. 3.8D**). Taken together, these findings are consistent with those of the intratibial model where GANT58-NP treatment significantly improved bone outcomes, but tumor burden was not significantly affected. While more studies are needed to further characterize potential effects on tumor growth, these studies

strongly demonstrate that GANT58-NPs reduce tumor-induced bone destruction in two mouse models of bone metastasis.

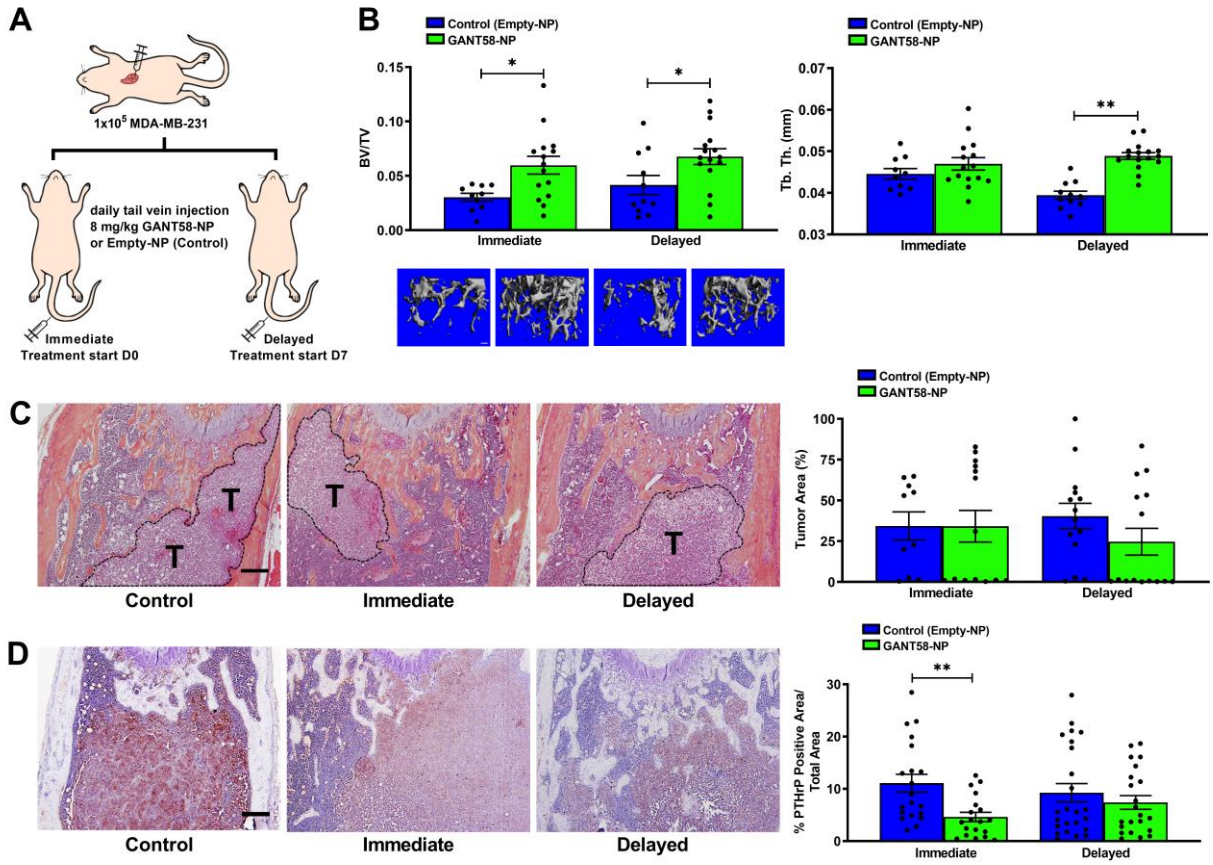

Fig. 3.8. GANT58-NP treatment reduces tumor-induced osteolysis in early metastasis model of tumor-induced bone disease. (A) Tumor-inoculation and treatment scheme for intracardiac model of bone metastasis. (B) µCT analysis of tibiae bone volume fraction (BV/TV) and trabecular thickness (Tb. Th.) showed significantly improved bone quality in mice treated with GANT58-NPs. (C) Representative H&E stained sections and histomorphometric analysis of tumor area (indicated by T) in Empty-NP-treated and GANT58-NP-treated in mice inoculated with MDA-MB-231 cells. Scale bar: 200 µm. (D) Representative images and quantification of immunohistochemical staining for PTHrP (red-brown staining) in femoral sections from Empty-NP-treated and GANT58-NP-treated tumor-bearing mice. Scale bar: 200 µm.

Safety profile of GANT58-NPs

In addition to efficacy, successful clinical translation of the GANT58-NPs hinges upon safety of the treatment at therapeutic doses. To test the safety profile of the GANT58-NPs, blood was drawn at time of sacrifice for the cohort of mice in the intratibial study after having received GANT58-NP or Empty-NP treatment 5 days/week at 8 mg/kg GANT58 (or equivalent dose of

Empty-NP) for 4 weeks. Biochemical analysis of blood serum markers for liver and kidney toxicity was performed. There was no significant increase in aspartate aminotransferase (AST), alanine aminotransferase (ALT), or blood urea nitrogen (BUN) levels above two standard deviations from average levels reported by the animal supplier (Envigo) (**Fig. S3.5A**). Further, histological sections of the liver and kidney of the same mice were observed by a blinded, board certified pathologist and there was no evident toxicity in either group (**Fig. S3.5B**).

3.5 Discussion

Metastatic disease accounts for over 90% of cancer-related deaths and therefore remains a major clinical concern [2]. In patients with bone metastases, standard-of-care RANKL and osteoclast inhibitors improve quality of life but do not target tumor-specific aberrations in signaling that cause TIBD. We identified Gli2 as a promising therapeutic target for bone metastases based on our previous studies establishing its overexpression in bone-destructive cell lines [26, 28]. While free GANT58 did not inhibit bone resorption *in vivo* due to its poor solubility and PK, GANT58-NPs significantly reduced bone resorption in intracardiac and intratibial injection models of TIBD using bone-metastatic breast and lung cancer cell lines.

Since RANKL and osteoclast inhibitors target osteoclast function throughout the body, osteoblast activity, which is tightly coupled with and triggered by bone resorption, is also decreased, which severely impairs bone remodeling and fracture healing [9, 133]. Consistent with these findings, other studies have reported dose-dependent inhibitory effects of bisphosphonates on osteoblast proliferation, differentiation, and mineralization [134, 135]. In contrast, the MTA GANT58 did not inhibit osteoblast hMSC proliferation or deposition of mineralized matrix by osteoblasts (**Fig. 3.5A-C**). GANT58 blocked nuclear translocation of Gli2 (**Fig. 3.4A-B**) and

consequent PTHrP expression *in vitro* (**Fig. 3.4C**) and *in vivo* (**Fig. 3.7K-L, 8D**). Considering that PTHrP stimulates expression of RANKL (a stimulator of osteoclast formation) by osteoblasts, we investigated the effects of GANT58 treatment on osteoclastogenesis in vitro. GANT58 treatment of mouse bone marrow-derived cells co-cultured with MDA-MB-231-bone tumor cells significantly inhibited osteoclastogenesis (**Fig. 3.5D-F**). These findings suggest that GANT58 blocks tumor-induced stimulation of osteoclastogenesis without impairing osteoblast differentiation.

While the current study establishes the therapeutic potential of Gli2 inhibition to block tumor-mediated bone destruction, other studies have previously utilized nanomedicine strategies for delivery of Hh pathway inhibitors to tumors. Delivery of Hedgehog Pathway Inhibitor-1 (HPI-1) has been investigated for treatment of medulloblastoma and hepatocellular carcinoma [107, 136]. While these studies showed that HPI-1 nanoparticles inhibited systemic metastases in an orthotopic model of human hepatocellular carcinoma, the effects of Hh inhibition on bone metastases were not investigated [107, 136]. Nanomedicine strategies have also been applied to inhibit bone metastases by delivering conventional chemotherapies to reduce bone tumor burden in the bone marrow [137, 138]. These studies found that nano-encapsulated docetaxel and paclitaxel reduced tumor burden, but the effects of the drugs on bone were not investigated extensively *in vivo*. Other studies have reported that conventional chemotherapies cause DNA damage and apoptotic cell death in human bone marrow cells, and that these treatments negatively affect trabecular bone microarchitecture and mechanical properties [139, 140]. Thus, targeted delivery of chemotherapies to tumors in bone is anticipated to have adverse effects on the bone microenvironment and warrants further investigation. In contrast, nano-encapsulated GANT58

blocked tumor-induced bone destruction in tumor-bearing bones, but the drug did not inhibit mineralization (**Fig. 3.5B-C**).

GANT58-NPs inhibited tumor proliferation (**Fig. 3.4D**) and viability (**Fig. 3.4E**) *in vitro*, but there were only modest changes in cytotoxicity with increasing GANT58 dose (**Fig. 3.4E**). These data suggest that GANT58 slows tumor growth but is not cytotoxic to tumor cells, which is consistent with previous studies reporting that GANT58 and GANT61 inhibit tumor proliferation by inducing cytostasis (cell cycle arrest) and early phase apoptosis rather than direct cytotoxic killing [35, 97, 141]. Our previous study showed that genetic inhibition of Gli2 using an Engrailed repressor construct significantly attenuated the ability of cancer cells to colonize bone (only micrometastases were observed) and induce osteolysis *in vivo* [28]. However, GANT58-NPs did not significantly reduce tumor burden in either the intratibial or intracardiac models. Micellar nanoparticles are passively targeted to tumor sites via the enhanced permeability and retention (EPR) effect, which requires the tumor vasculature to be permeable or "leaky" in order for nanoparticles to accumulate within the tumoral interstitial space [142]. Though the significant reduction in PTHrP expression confirms on-target delivery of GANT58-NPs into bone-associated tumors, the nanoparticles likely do not sufficiently accumulate at bone-tumor sites until larger, vascularized tumors are established, at which point it is difficult to reduce tumor burden in the short time-line of current animal models. In future studies, we will evaluate the nanoparticle carrier to determine if conferring bone-binding affinity to the polymer chemistry will improve targeted delivery to bone and block initial bone tumor establishment.

There may also be spatial variation in the tumor cell responsiveness to GANT58 within the bone and bone marrow. Matrix rigidity in the bone microenvironment is a key mediator of Gli2 expression in bone-metastatic tumor cells. Gli2 expression was significantly increased in patient

bone-metastatic tumors but not soft tissue tumors (**Fig. 3.1A-B**) or brain and lung metastases (**Fig. 3.1C**). Furthermore, Gli2 is not expressed on collagen-like (30 MPa) substrates but is overexpressed on bone-like (>100 MPa) substrates *in vitro* [43]. Considering the relatively low elastic modulus of bone marrow (0.25–24.7 kPa) [143], tumor cells growing in the marrow space are anticipated to express low levels of Gli2 and are therefore likely to be less sensitive to GANT58. However, as tumor cells approach the interface with bony trabeculae, they overexpress Gli2 and PTHrP in response to the rigid (>100 MPa) mineralized bone matrix [42, 43]. Thus, GANT58 is anticipated to inhibit tumor cell proliferation, expression of PTHrP, and the transition to the bone-destructive phenotype in tumor cells within close proximity of bone but potentially have less direct impact on tumor cells in the marrow space. In future studies using bone targeted approaches, we will evaluate whether GANT58 can block the transition of tumor cells from micro-metastatic cells in the bone marrow to more aggressive and bone destructive tumors that have invaded the bone.

Previous studies have also implied the importance of tumor-stromal interactions in promoting bone metastasis [18]. Recent work has elucidated new molecular mechanisms and therapeutic targets for prevention of bone metastasis and/or halting the vicious cycle of bone destruction. In addition to Hh signaling, Notch signaling has been implicated in bone metastasis, and the Notch ligand Jagged1 drives tumor progression in bone [144]. A subsequent study developed a Jagged1 antibody that not only reduced incidence of bone metastasis, but also sensitized the tumor to chemotherapy and reduced tumor recurrence [145]. Another recent study showed that crosstalk between ROR1-HER3 and the Hippo-YAP pathway promotes breast cancer bone metastasis and identified multiple new therapeutic targets for inhibition [146]. While these tumor-targeted approaches offer the potential of reducing tumor burden in bone, inter-patient

heterogeneity may limit their ability to benefit all bone-metastatic cancer patients [147]. In patients with metastatic cancer, PTHrP is expressed in > 90% of bone-residing tumors compared to < 20% at non-bony sites [148]. Similarly, we show that Gli2 is also overexpressed in bone-metastatic tumors from various primary sites (**Fig. 3.1A-B**). The prevalence of Gli2 and PTHrP expression in bone suggests that GANT58 treatment is likely to be effective in a broad spectrum of patients suffering from bone metastases, which is supported by our observations of bone protection by GANT58-NPs across both breast and lung cancer models. Thus, combined delivery of GANT58, which blocks the transition to the bone-destructive phenotype, with targeted therapies or conventional chemotherapeutics that block tumor growth in the bone marrow could potentially slow the progress of TIBD and improve patient quality of life.

3.6 Conclusions

Polymeric NP encapsulation of GANT58 provided an injectable aqueous dispersion that significantly decreased bone lesions and increased trabecular bone volume in two breast cancer models of bone metastasis (intratibial and intracardiac). Importantly, GANT58-NPs did not alter hMSC proliferation or osteoblast mineralization, essential processes for bone remodeling and fracture repair in cancer patients. Pharmacokinetic and biodistribution analysis showed the GANT58-NPs exhibit an extensive circulation time, preferentially localize at the tumor site, and show no evidence of cytotoxicity in the liver or kidneys, the major organs through which the GANT58-NPs are cleared. Thus, the efficacy and safety profile of GANT58-NPs provide promising rationale to continue testing GANT58-NPs in pre-clinical models of TIBD to potentially lead to novel therapies for reducing TIBD.

3.7 Supplementary Data

Table S1. Clinical features of patient tumor samples.

Patient ID	Age (years)	Gender	Primary Site	Histological Type	Metastatic Site	Chemotherapy	Radiotherapy	Pathologic Fracture
45478	38	F	Soft Tissue	Myxoid sarcoma	-	Y	N	N
45479	69	M	Soft Tissue	Myxoid sarcoma	-	N	N	N
52086	22	M	Soft Tissue	Synovial sarcoma	-	Y	N	N
50892	58	F	Bone	Ewing's sarcoma	Kidney	Y	Y	N
48233	59	F	Breast	Carcinoma*	Humerus	N	Y	Y
48538	80	F	Breast	Carcinoma†	Femur	N	Y	Y
51392	69	F	Breast	Carcinoma‡	Femur	Y	Y	Y
48081	55	M	Kidney	Renal cell carcinoma	Femur	Y	Y	Y
48459	73	M	Kidney	Renal cell carcinoma	Humerus	N	N	N
48640	77	M	Kidney	Renal cell carcinoma	Femur	N	N	N
48641	77	M	Kidney	Renal cell carcinoma	Tibia	N	N	N
48909	50	M	Kidney	Renal cell carcinoma	Femur	N	N	Y
49652	63	F	Lung	Non-small cell carcinoma	Humerus	Y	Y	Y
53159	77	M	Lung	Non-small cell carcinoma	Humerus	Y	Y	N
52963	69	M	Lung	Squamous cell carcinoma	Humerus	N	N	Y
53107	67	M	Lung	Squamous cell carcinoma	Femur	Y	Y	Y
50080	80	M	Prostate	Adenocarcinoma	Femur	Y	N	N
48089	54	F	Thyroid	Follicular carcinoma	Pelvis	Y	Y	N
52766	69	M	Thyroid	Follicular carcinoma	Pelvis	N	N	Y
49224	29	F	Unknown	Squamous cell carcinoma	Fibula	Y	Y	Y

ER: estrogen receptor; PR: progesterone receptor; HER2: human epidermal growth factor receptor 2
*Receptor status unknown; †ER+/PR+; ‡ER+/PR-/HER2+

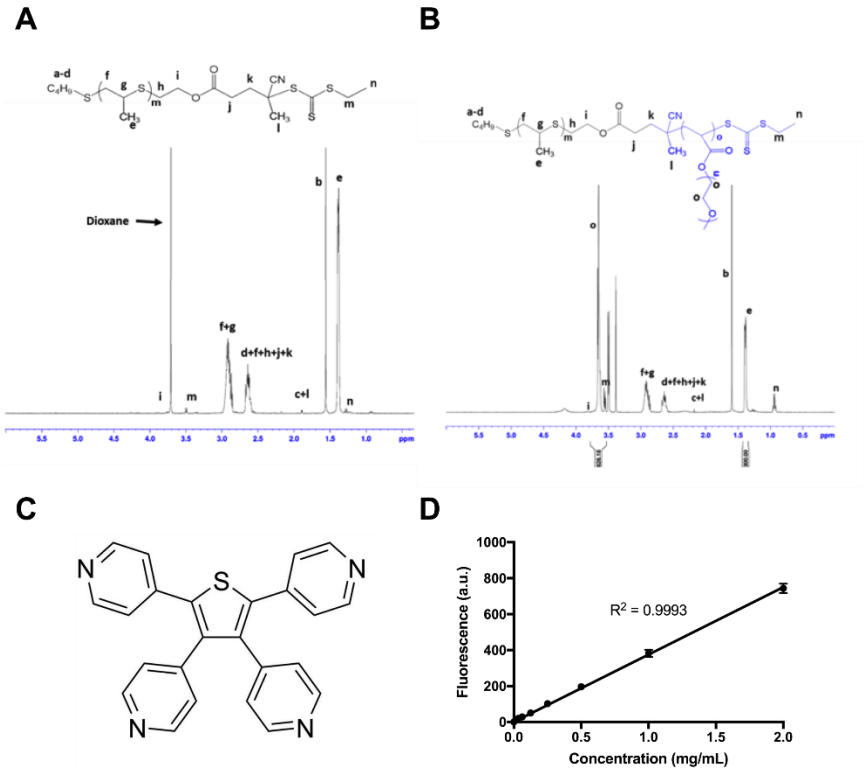

Fig. S3.1. PPS_{135}-b-$POEGA_{17}$ synthesis and GANT58 characterization. (A) ^{1}H-NMR of PPS_{135}-ECT and (B) PPS_{135}-b-$POEGA_{17}$. (C) GANT58 chemical structure. (D) GANT58 fluorescence standard curve.

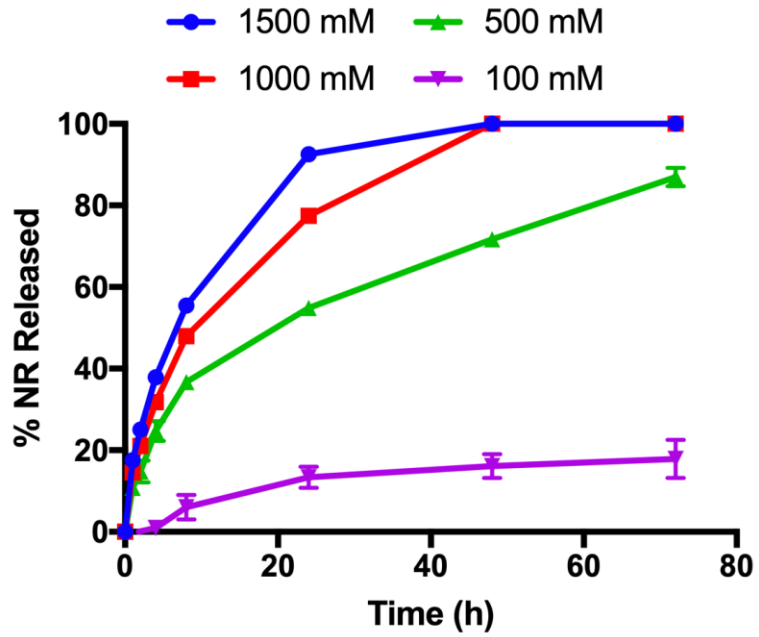

Fig. S3.2. H_2O_2 concentration-dependent release of Nile red (NR) from NPs. H_2O_2 concentrations were chosen to include physiologically relevant ROS concentrations (~100-400 mM) based on calculations from published values for macrophage ROS generation rates.

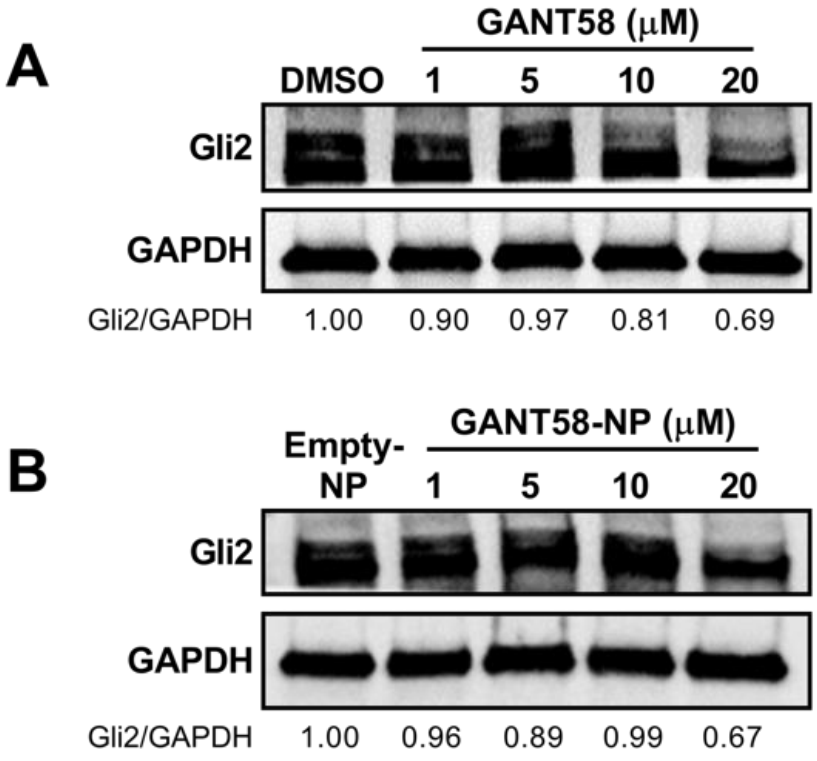

Fig. S3.3. Western blots of Gli2 cytoplasmic protein after 72 hr treatment with (A) free GANT58 and (B) GANT58-NPs.

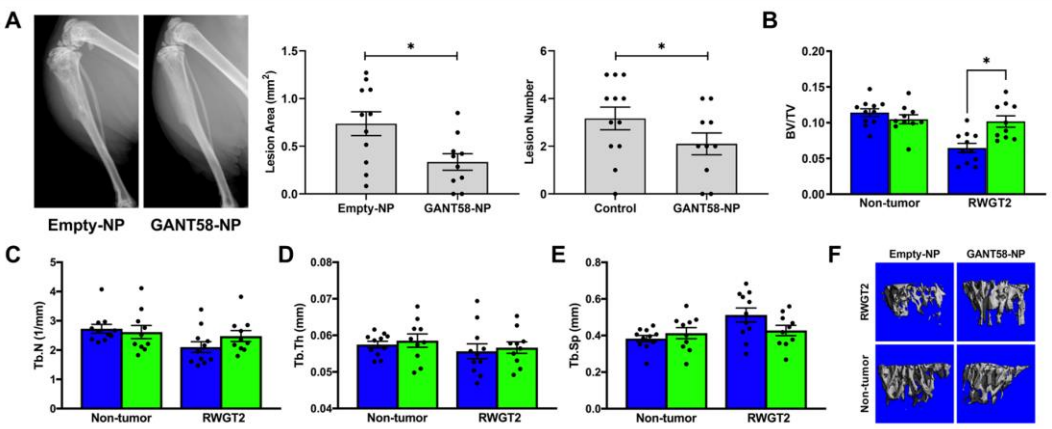

Fig. S3.4. RWGT2 Faxitron and µCT analysis. (A) Representative radiographic images of Empty-NP (control) and GANT58-NP treated mice at 4-weeks post-tumor inoculation with RWGT2 cells. Lesion area and lesion number as assessed by radiographic analysis (right). µCT analysis of tibiae (B) bone volume fraction (BV/TV), (C) trabecular number (Tb. N.), (D) trabecular thickness (Tb. Th.), and (E) trabecular separation (Tb. Sp.) in mice treated with Empty-NPs (blue) or GANT58-NPs (green) after sacrifice at 4 weeks. (F) Representative µCT reconstructions of GANT58-NP-treated, Empty-NP-treated, and contralateral, non-tumor bearing tibiae.

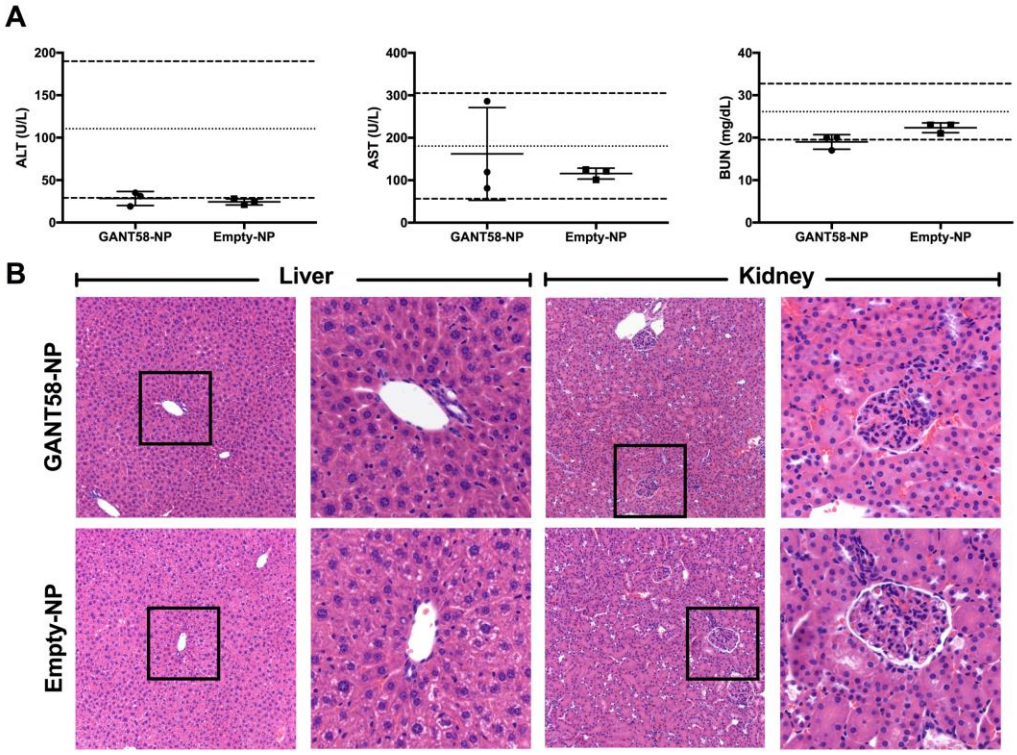

Fig. S3.5. GANT58-NPs elicit minimal systemic toxicity. (A) Serum chemical markers of liver (ALT and AST) and kidney (BUN) toxicity measured after 8 mg/kg GANT58-NP i.v. treatment 5 days/week for 4 weeks. (B) Representative images of liver and kidney at 10x and 20x with GANT58-NP and Empty-NP treatment.

CHAPTER 4

GLI ANTAGONIST BLOCKS BONE INVASION BY ORAL SQUAMOUS CELL CARCINOMAS REGARDLESS OF EGFR INHIBITOR RESISTANCE

4.1 Abstract

Oral squamous cell carcinoma (OSCC) is the most common type of head and neck cancer, accounting for over 90% of all cases. Despite advances in surgery and chemoradiation therapy, the prognosis for patients with tumors that have invaded the mandible remains poor (5-year survival rate $\leq$ 50%). Current therapies targeting epidermal growth factor receptor (EGFR), which is highly expressed in OSCC, have also failed to improve outcomes due to resistance mechanisms. Thus, new treatments are needed in order to improve patient morbidity and mortality. Here, we demonstrate that EGFR signaling promotes mandibular invasion by modulating the expression of Gli2 and its transcriptional target parathyroid hormone-related protein (PTHrP). Treatment with the EGFR tyrosine kinase inhibitor erlotinib (5 μM) significantly decreased EGF-stimulated Gli2 and PTHrP expression in OSCC cells (SCC4, HSC3, CAL27) but not in erlotinib-resistant cells (C27R). However, treatment with the Gli-antagonist GANT58 (10 μM) decreased Gli2-mediated PTHrP expression in both erlotinib-sensitive and resistant cells as well as significantly reduced cell proliferation *in vitro*. To elucidate whether pharmacological inhibition of Gli2 blocks OSCC-induced bone destruction, we utilized a semi-orthotopic mouse model of mandibular invasion and locally delivered GANT58 encapsulated within reactive oxygen species (ROS)-responsive polymeric microparticles (GANT58-MPs). Although GANT58-MP treatment (5 mg/kg) did not reduce tumor burden, we observed a significant decrease in bone lesion area ($p < 0.01$) and lesion number ($p < 0.0001$) in mice inoculated with either CAL27 or C27R cells compared to tumor-

bearing mice treated with empty-MPs (control). Similarly, micro-CT analyses revealed that both CAL27 and C27R tumor-bearing mice treated with GANT58-MPs had significantly higher trabecular bone volume ($p < 0.001$) compared to control treated mice. Taken together, these data suggest that Gli-inhibition via GANT58-MPs is a potential strategy for treating OSCC patients with bone-invasive tumors regardless of their resistance to existing EGFR inhibitors.

4.2 Introduction

Head and neck cancer is the sixth most common cancer by incidence worldwide, with more than 50,000 new cases diagnosed annually in the United States [1, 149, 150]. Over 90% of all head and neck cancers are squamous cell carcinomas that originate in the oral cavity and oropharynx [151, 152]. Despite advances in treatment, the overall survival of patients with oral squamous cell carcinoma (OSCC) has not improved for decades, which is largely attributed to tumor recurrence and local invasion. OSCC frequently invades the mandible and induces bone destruction, a major complication that predicts poor prognosis (5-year survival rate $\leq$ 50%) [153-155]. In lieu of effective targeted therapies, surgical resection of the tumor and involved bone is standard-of-care for patients with mandibular bone invasion, but current procedures are associated with comorbidities that drastically reduce quality of life (e.g., dysfunctional respiration, articulation, mastication) [156]. Likewise, adjuvant chemotherapy and radiotherapy cause significant damage to remaining healthy bone, further limiting oral function [157-159]. Furthermore, existing anti-resorptive agents like bisphosphonates and denosumab are contraindicated for OSCC patients due to complications of medication-related osteonecrosis of the jaw (MRONJ) [160]. Thus, targeted therapies that prevent bone destruction are needed in order to reduce patient morbidity and mortality.

Epidermal growth factor receptor (EGFR) is highly expressed in OSCC and has been implicated in promoting osteoclast-mediated bone destruction [161-163]. Accordingly, preclinical studies have intensely focused on EGFR as a molecular target and prompted the development of drugs that antagonize receptor signaling. Until the recent FDA approval of pembrolizumab (PD-1 inhibitor) [164], the EGFR-directed monoclonal antibody cetuximab was the only targeted therapy approved for treatment of recurrent and/or metastatic OSCC [165-168]. However, response rates to cetuximab as a single agent have been consistently low (~15%). The addition of cetuximab to chemoradiotherapy has also failed to improve outcomes [152, 165, 169]. Ultimately, OSCC patients who initially respond to cetuximab or other EGFR tyrosine kinase inhibitors (TKIs) often develop resistance which results in tumor recurrence [170, 171]. Recurrent OSCC tumors are typically more aggressive and invasive, and there are no viable treatment options for patients once they develop resistance to EGFR inhibitors. Therefore, identifying novel drug targets remains a major priority.

The Hedgehog (Hh) signaling pathway is an essential regulator of cell proliferation and differentiation during embryonic development [19, 20]. Aberrant activation of Hh signaling in adult tissues is associated with tumor progression and has been observed in various types of cancer, including OSCC [21-25]. Our previous work demonstrated that the Hh transcription factor Gli2 stimulates expression of parathyroid hormone-related protein (PTHrP) in bone-invasive OSCC cells [27, 172]. Genetic inhibition of Gli2 attenuates PTHrP expression and blocks osteoclast-mediated bone destruction induced by OSCC cells *in vivo*, suggesting that Gli2 is an ideal therapeutic target for advanced oral cancer [172]. Several small molecule inhibitors targeting Gli family proteins have been identified and have demonstrated anti-tumor activity in subcutaneous xenograft models of prostate, breast, and hepatocellular carcinoma, in large part, because they

block Gli transcriptional activity irrespective of the mode of upstream activation [35, 36, 136, 173]. However, preclinical studies investigating the effects of these inhibitors against tumors residing in bone are limited due to their low water solubility. Therefore, we previously developed polymeric nanoparticles that enhanced the solubility and pharmacokinetic profile of the Gli-antagonist GANT58 to enable systemic delivery to bone metastases *in vivo* [174, 175].

In the present study, we report that EGFR signaling regulates Gli-mediated transcription of PTHrP in bone-invasive OSCC cells. Treatment with the EGFR TKI erlotinib significantly reduced Gli2 and PTHrP expression in multiple OSCC lines but not in erlotinib-resistant cells. However, treatment with GANT58 inhibited Gli2 and PTHrP expression in cells that were either sensitive or resistant to erlotinib. Using a semi-orthotopic mouse model of mandibular invasion, we locally delivered GANT58-loaded polymeric microparticles (GANT58-MPs) to investigate its therapeutic efficacy against these tumors *in vivo*. We found that GANT58-MPs reduced bone destruction induced by OSCC tumors regardless of their response to EGFR inhibition.

4.3 Results

EGFR and Gli2 are correlated in OSCC patient tumors

We first queried the TCGA PanCancer Atlas to determine the prevalence of EGFR and Gli2 alterations in patients with OSCC (**Fig. 4.1A**). Analysis of this dataset revealed that EGFR and Gli2 were upregulated in 10-15% of OSCC patient tumors (**Fig. S4.1**). Moreover, there was a significant positive correlation between EGFR and Gli2 mRNA levels (**Fig. 4.1B**). To identify patients with bone-invasive tumors, we conducted a review of all publicly available pathology reports in the same dataset. Consistent with our previous findings, Gli2 expression was higher in OSCC tumors that invaded bone (e.g., mandible, maxilla) compared to non-invasive tumors (**Fig.**

4.1C). Bone invasion was also associated with a significant decrease in overall patient survival (**Fig. 4.1D**). These findings suggest that the EGFR/Gli2 signaling axis may be important for OSCC tumor progression and bone invasion.

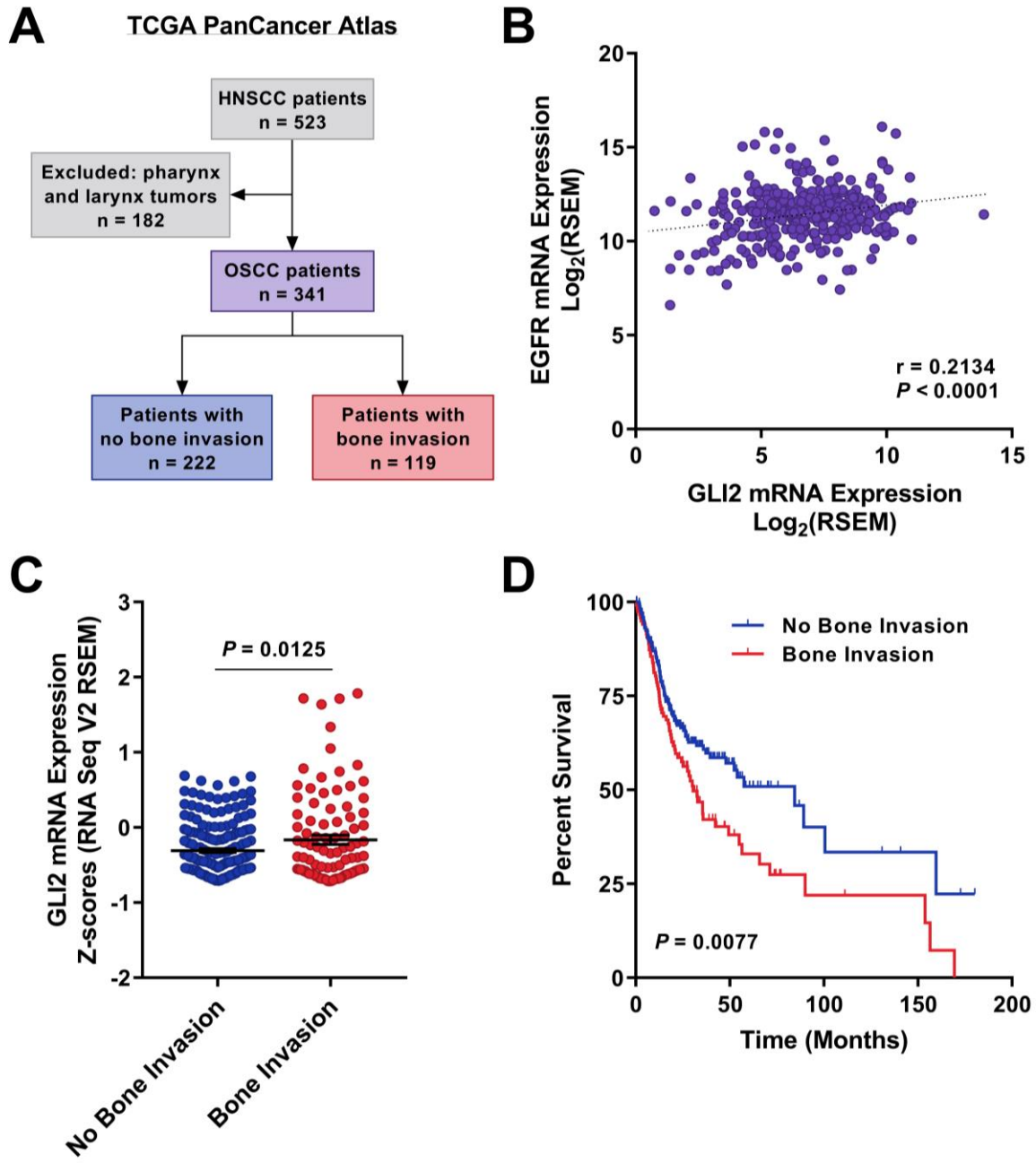

Fig. 4.1. EGFR and Gli2 are correlated in OSCC patient tumors. (A) Flow chart of patient selection from the TCGA PanCancer Atlas dataset. **(B)** Correlation of EGFR and Gli2 mRNA levels in OSCC patient tumors (n = 341). Pearson's correlation analysis. **(C)** Gli2 mRNA expression in patients with (n = 119) or without (n = 222) bone-invasive tumors. Student's unpaired t-test. **(D)** Kaplan-Meier survival curves for OSCC patients with or without bone-invasion. Log-rank test.

EGFR signaling regulates Gli2 and PTHrP in bone-invasive OSCC cells

To determine whether EGFR regulates Gli2 expression in OSCC cells that induce bone destruction, we treated human OSCC lines (SCC4, HSC3, CAL27) with EGF (10 ng/ml) in the presence or absence of 5 μM erlotinib for 48 hours (**Fig. 4.2A**). Western blot analysis showed that while EGF treatment increased Gli2 protein levels, erlotinib significantly reduced EGF-stimulated Gli2 expression (**Fig. 4.2B-C**). Since Gli2 is a transcription factor, we next investigated if EGFR signaling modulates its translocation into the nucleus. Decreased colocalization of Gli2 with DAPI-stained nuclei was observed in OSCC cells treated with erlotinib compared to those treated with EGF alone, as assessed by immunofluorescence (**Fig. 4.2D-E**). Using a Gli-dependent enhanced green fluorescent protein reporter (pGL3b-8XGliBS:EGFP) [36], we discovered that erlotinib also attenuated Gli2 DNA-binding activity in the nucleus (**Fig. S4.2A-B**). Consequently, EGF-stimulated PTHrP expression was also significantly reduced with erlotinib treatment (**Fig. 4.2F**). Taken together, these data indicate that Gli2 expression and activity, as well as the expression of its transcriptional target PTHrP, are mediated by EGFR in bone-invasive OSCC cells.

Erlotinib-resistant cells reactivate pAKT/pERK to maintain Gli2 and PTHrP expression

Several mechanisms of acquired resistance to EGFR inhibitors have been elucidated in both preclinical and clinical studies. The most common mechanism is the development of

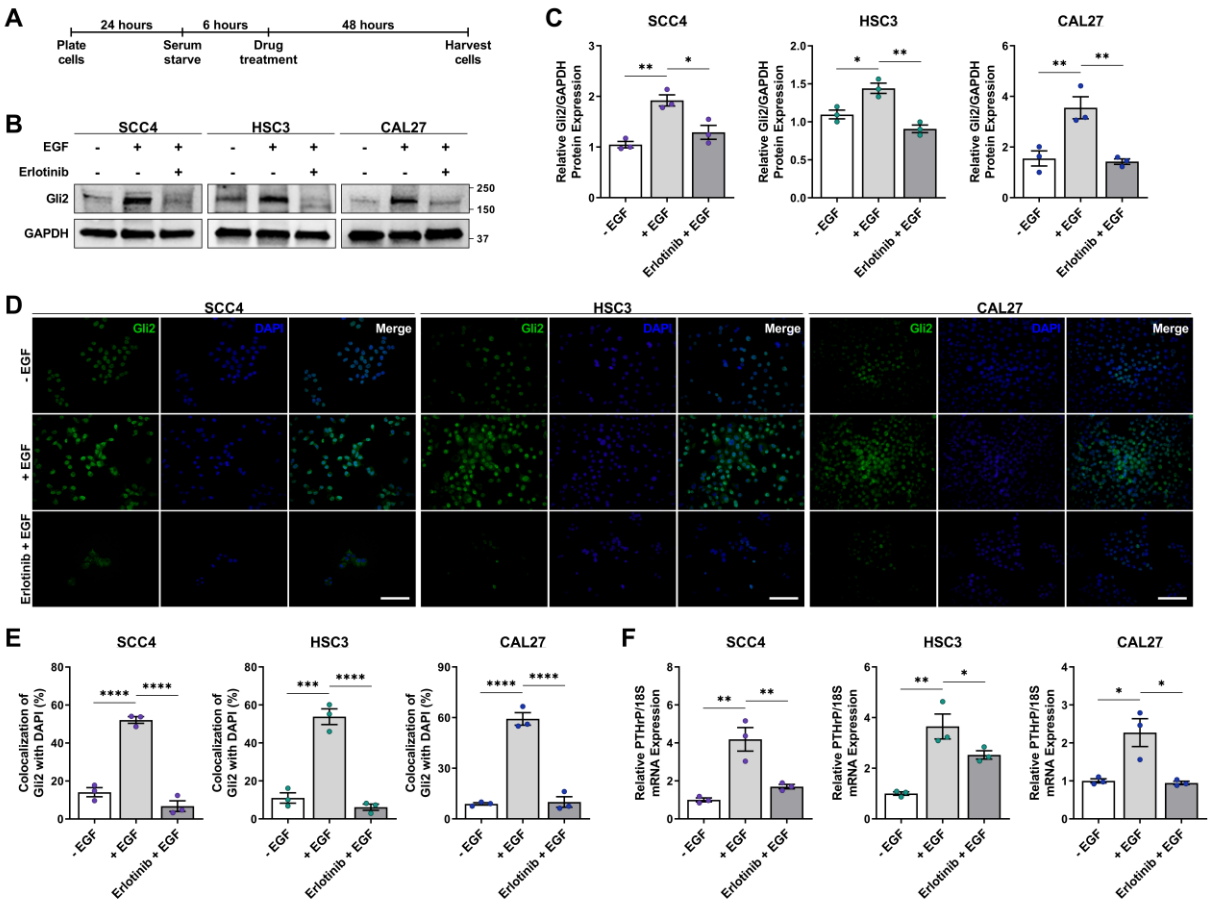

Fig. 4.2. EGFR signaling regulates Gli2 and PTHrP in OSCC. (A) Experimental timeline of drug treatment. **(B)** Representative western blots and **(C)** quantification of Gli2 protein in OSCC cell lines treated with DMSO (-EGF), 10 ng/ml rhEGF (+EGF), or a combination of rhEGF and 5 μM erlotinib (Erlotinib + EGF) for 48 hr. **(D)** Representative immunofluorescent images and **(E)** quantification of Gli2 colocalized with DAPI staining. Scale bars: 100 μm. **(F)** qPCR analysis of PTHrP mRNA levels in OSCC cells. n = 3 biological replicates for panels C, E, and F.

secondary mutations in EGFR, such as T790M, which is detected in over 50% of non-small cell lung cancer (NSCLC) patients with disease progression after initial response to erlotinib or gefitinib [176, 177]. In contrast, approximately 20-40% of OSCC patients express a truncated, constitutively active form of EGFR called variant III (EGFRvIII) [162, 178, 179]. Other mechanisms of resistance to EGFR-targeted therapies in OSCC include epithelial-mesenchymal transition (EMT) and activation of alternative and/or downstream pathways [170, 171].

In order to generate the erlotinib-resistant OSCC line C27R, we cultured CAL27 cells in the presence of increasing concentrations of erlotinib for 6 months (**Fig. 4.3A**). We observed by

fluorescent microscopy that CAL27 cells exhibited a typical epithelial-like morphology (round and flat) while the C27R cells had adopted a mesenchymal-like morphology (elongated and spindle-shaped) (**Fig. 4.3B**). Despite EGFR inhibition, C27R cells showed robust expression of phosphorylated AKT and ERK protein compared to the CAL27 cells from which they were derived (**Fig. 4.3C-D**). Furthermore, erlotinib treatment did not attenuate Gli2 protein levels or its nuclear localization in C27R cells (**Fig. 4.3E-H**). There was also no significant difference in PTHrP mRNA expression between treatments (**Fig. 4.3I**).

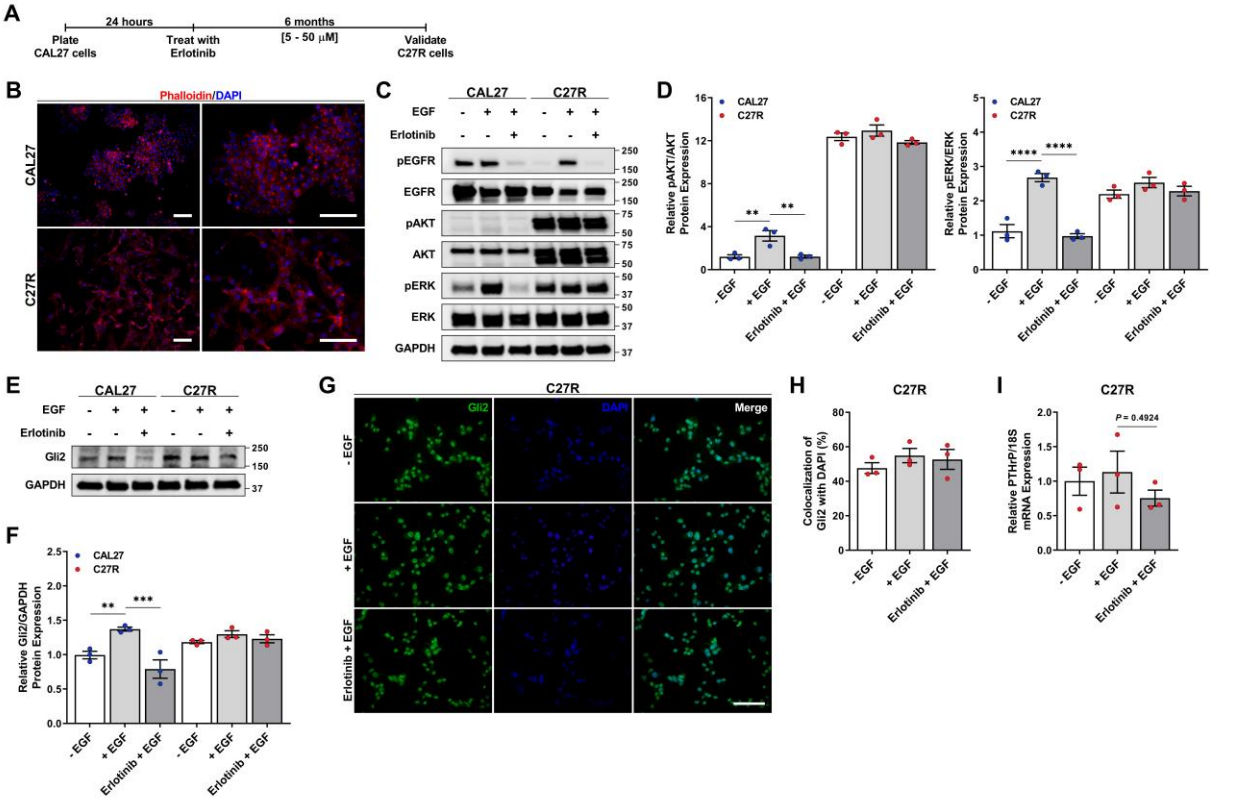

Fig. 4.3. Erlotinib-resistant cells adopt mesenchymal-like morphology while maintaining Gli2 and PTHrP expression via pAKT/pERK. (A) Timeline of C27R cell line generation. **(B)** Fluorescent images showing epithelial- and mesenchymal-like morphologies of CAL27 and C27R cells, respectively. Scale bars: 100 μm. **(C)** Representative western blots and **(D)** quantification of EGFR and downstream signaling kinases in CAL27 and C27R cells treated with DMSO (-EGF), 10 ng/ml rhEGF (+EGF), or a combination of rhEGF and 5 μM erlotinib (Erlotinib + EGF) for 48 hr. **(E)** Representative western blots and **(F)** quantification of Gli2 protein in CAL27 cells compared to C27R cells after the same drug treatments. **(G)** Representative immunofluorescent images and **(H)** quantification of Gli2 colocalized with DAPI staining. Scale bar: 100 μm. **(I)** qPCR analysis of PTHrP mRNA levels in C27R cells. n = 3 biological replicates for panels C, E, G, and F.

To evaluate whether the phosphorylation of AKT and ERK were contributing to Gli2 expression in the erlotinib-resistant line, we inhibited phosphorylation of these kinases using the PI3K and MEK inhibitors LY294002 and U0126, respectively. Inhibition of either pAKT or pERK was sufficient to reduce Gli2 protein expression in C27R cells (**Fig. S4.3A-D**), suggesting that erlotinib-resistant cells reactivate these downstream kinases to maintain Gli2 and PTHrP expression.

GANT58 changes the transcriptomic profiles of both erlotinib-sensitive and resistant cells

We performed RNA sequencing (RNA-seq) on CAL27 and C27R cells treated with or without GANT58 (10 μM) to investigate transcriptomic changes associated with Gli inhibition. Principal component analysis (PCA) showed distinct clustering of CAL27 and C27R samples along the first principal component (PC1), which accounts for 91% of the total variance. Control and GANT58-treated samples are also clearly separated along PC2 (explains 6% of the total variance), irrespective of their resistance status (**Fig. 4.4A**).

Further analyses revealed significant differential expression of over 5000 genes between CAL27 and C27R cells (**Fig. 4.4B**). Consistent with previous reports implicating EMT as a mechanism of EGFR inhibitor resistance [170, 171], we identified several genes with roles in EMT among the top 50 most differentially expressed. Specifically, the epithelial marker *CDH1* and EMT suppressor *GRHL2* [180, 181] were both upregulated in CAL27 cells. In contrast, the mesenchymal marker *VIM* and EMT-promoting transcription factor *ZEB2* were upregulated in C27R cells (**Fig. 4.4C**). Recent studies have shown that fibroblast growth factor receptor 1 (*FGFR1*) promotes EMT-mediated resistance to third-generation EGFR TKIs (e.g., osimertinib)

in NSCLC [182, 183]. Interestingly, *FGFRI* was also upregulated in the erlotinib-resistant C27R cells (**Fig. 4.4C**).

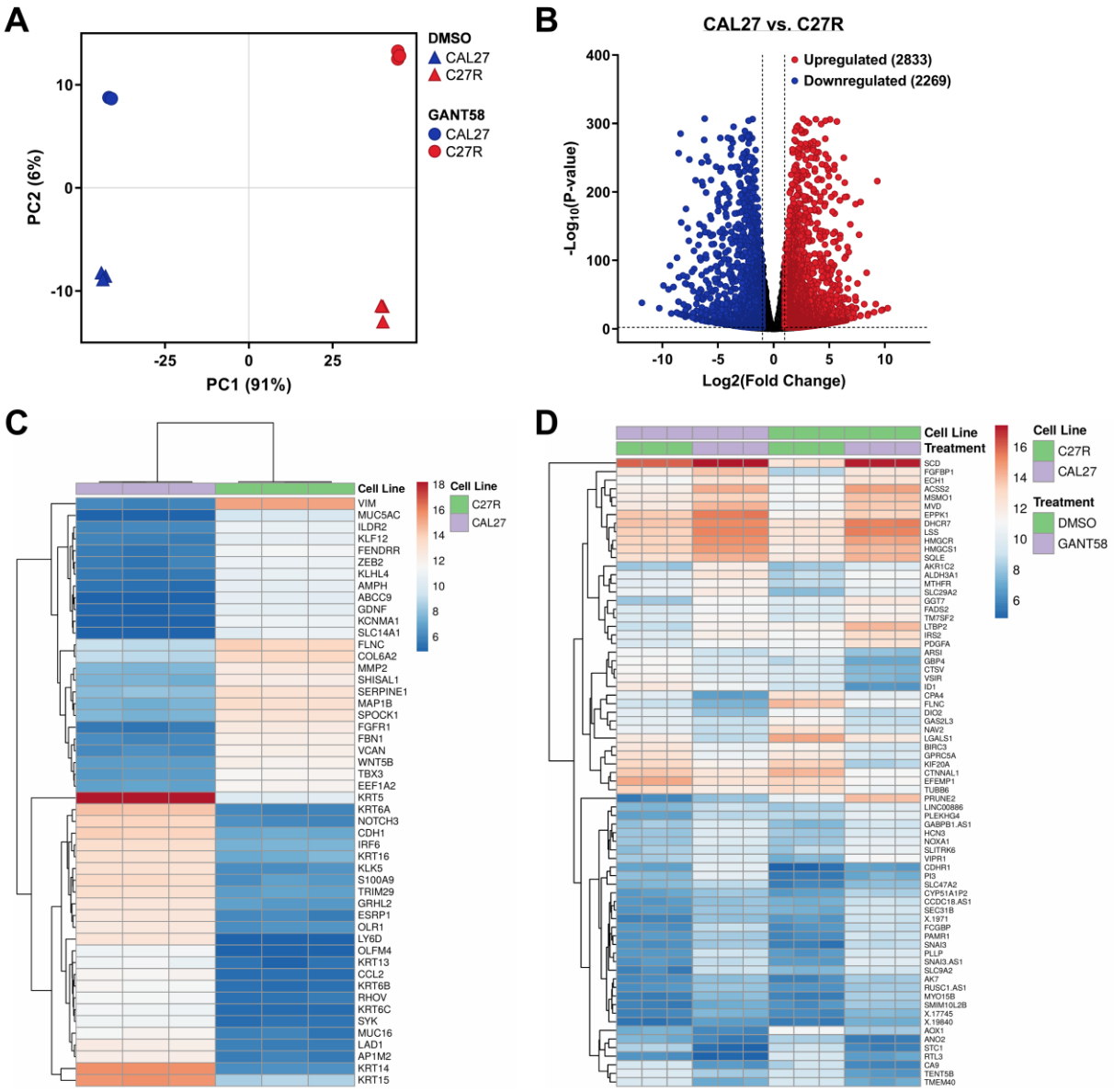

Fig. 4.4. GANT58 changes CAL27 and C27R transcriptomic profiles. (A) Principal component analysis (PCA) of CAL27 and C27R cells from RNA-seq data. **(B)** Volcano plot of differential expressed genes as assessed by RNA-seq analysis. Differentially expressed genes were selected with thresholds of a fold change >2 and $p<0.01$. **(C)** Heatmap of the top 50 most differentially expressed genes between CAL27 and C27R cells. **(D)** Heatmap of 73 overlapping genes in CAL27 and C27R cells treated with GANT58 for 48 hr as measured by RNA-seq.

Next, we evaluated the top 100 most differentially expressed genes in response to GANT58 treatment and identified 49 upregulated and 24 downregulated genes shared between CAL27 and C27R cells. Many of these overlapping genes were involved in cholesterol biosynthesis and lipid metabolism such as 7-dehydrocholesterol reductase (*DHCR7*), methylsterol monooxygenase 1 (*MSMO1*), and fatty acid desaturase 2 (*FADS2*). Surprisingly, GANT8 treatment altered the expression of HMG-CoA synthase (*HMGCS1*), HMG-CoA reductase (*HMGCR*), and mevalonate diphosphate decarboxylase (*MVD*) which are key enzymes of the mevalonate pathway (bisphosphonates disrupt this metabolic pathway in osteoclasts to inhibit bone resorption) (**Fig. 4.4D**) [184, 185]. Taken together, these data suggest that GANT58 treatment may be efficacious against both CAL27 and C27R cells despite their diverging transcriptomic profiles.

GANT58 reduces Gli2-mediated PTHrP expression and cell proliferation in both erlotinib-sensitive and resistant cells

To test the hypothesis that Gli inhibition would be effective in both lines, we treated CAL27 and C27R cells with 10 μM GANT58 for 48 hr. GANT58 treatment significantly decreased Gli2 protein expression (**Fig. 4.5A-B**) and nuclear colocalization in both cell lines (**Fig. 4.5C**). Consequently, PTHrP mRNA expression was also inhibited in both lines (**Fig. 4.5D**). To determine the effect of GANT58 on cell growth, CAL27 and C27R cells were treated with 20 μM GANT58 for 7 days and proliferation was measured by MTT assay. Treatment with GANT58 alone significantly reduced the proliferation of both cells *in vitro* compared to the DMSO control (**Fig. 4.5E**). As expected, treatment with 10 μM erlotinib significantly reduced CAL27 cell proliferation while no significant change was observed in C27R cells (**Fig. 4.5E**). Likewise, the erlotinib + GANT58 drug combination significantly reduced proliferation of CAL27 cells compared to

treatment with GANT58 alone whereas no significant decrease was seen in the C27R line with erlotinib + GANT58 treatment (**Fig. 4.5E**). Based on these findings, we decided to proceed with GANT58 monotherapy *in vivo*.

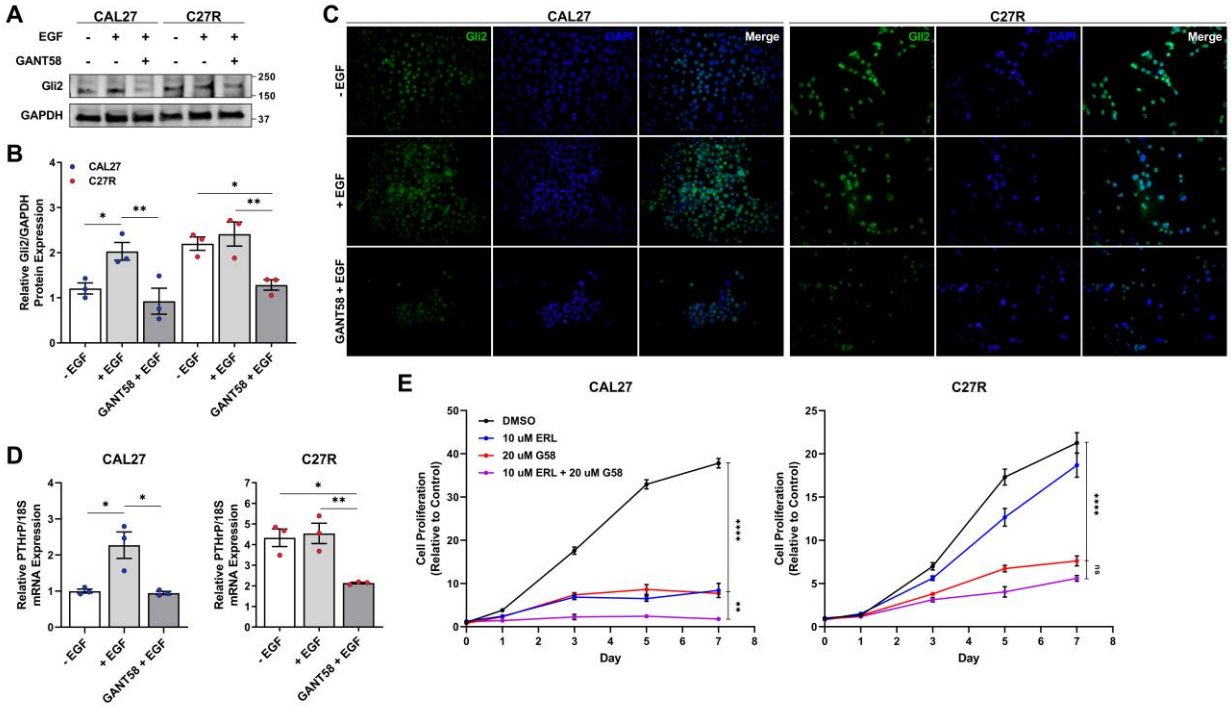

Fig. 4.5. GANT58 reduces Gli2-mediated PTHrP expression and cell proliferation in CAL27 and C27R cells. **(A)** Representative western blots and **(B)** quantification of Gli2 protein in CAL27 and C27R cells treated with DMSO (-EGF), 10 ng/ml rhEGF (+EGF), or a combination of rhEGF and 10 μM GANT58 (GANT58 + EGF) for 48 hr. **(C)** Representative immunofluorescent images Gli2 colocalized with DAPI staining after GANT58 treatment. **(D)** qPCR analysis of PTHrP mRNA levels in CAL27 and C27R cells. **(E)** Tumor cell proliferation as assessed by MTS assay after 48 hr treatment with DMSO, 10 μM erlotinib (ERL), 20 μM GANT58 (G58), or a combination of erlotinib and GANT58 (ERL + G58).

GANT58-MPs reduce bone invasion by erlotinib-sensitive and resistant OSCC tumors in vivo

In order to enhance the pharmacokinetic (PK) properties of GANT58 and improve local delivery to OSCC tumors *in vivo*, we loaded GANT58 into poly(propylene sulfide) (PPS) microparticles that we previously developed [114]. We then utilized a semi-orthotopic model in which CAL27 or C27R cells were injected into the masseter muscle of athymic nude mice and treated with 5 mg/kg GANT58-MPs or control Empty-MPs intratumorally (**Fig. 4.6A**). Due to

different rates of tumor growth, CAL27 and C27R mice were sacrificed separately (when the majority of their respective non-treated cohort reached humane endpoint) and mandibles were collected for *ex vivo* analyses. Despite the promising *in vitro* results, no significant difference in tumor weight was observed for either CAL27 or C27R mice treated with GANT58-MPs or Empty-MP (**Fig. S4.4A**). Histomorphometric analysis of the mandibles also showed no significant differences in tumor burden within groups (**Fig. S4.4B-C**).

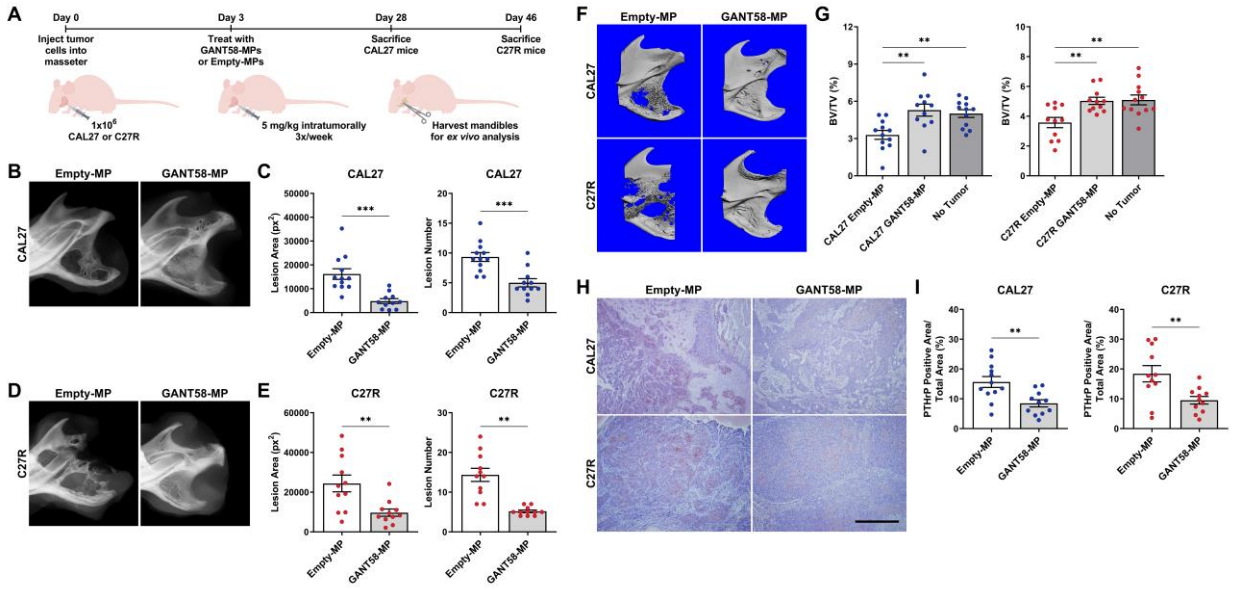

Fig. 4.6. GANT58-MP treatment blocks bone invasion by both CAL27 and C27R cells *in vivo*. (A) Experiment schematic for semi-orthotopic OSCC model and drug treatment. **(B)** Representative radiographic images of mandibles from CAL27 tumor cohort treated with Empty-MP and GANT58-MP. 4-weeks post-tumor inoculation. **(C)** Lesion area and lesion number as assessed by radiographic analysis are significantly reduced in GANT58-MP treated mice with CAL27 tumors. Student's unpaired t-test. **(D)** Representative radiographic images of mandibles from C27R tumor cohort treated with Empty-MP and GANT58-MP. 6-weeks post-tumor inoculation. **(E)** Lesion area and lesion number as assessed by radiographic analysis are significantly reduced in GANT58-MP treated mice with C27R tumors. Student's unpaired t-test. **(F)** Representative µCT reconstructions and **(G)** µCT analysis of mandibular bone volume fraction (BV/TV) of Empty-MP and GANT58-MP-treated CAL27 and C27R mice. Contralateral, non-tumor bearing, non-treated mandible also quantified. **(H)** Representative images and **(I)** quantification of immunohistochemical staining for PTHrP (positive staining = brown) in sections from Empty-MP and GANT58-MP treated tumor-bearing mice. Scale bar: 500 µm. Student's unpaired t-test.

However, while substantial osteolytic lesions were seen radiographically in mice treated with Empty-MPs, smaller and fewer lesions were visible in GANT58-MP treated mice in both CAL27 and C27R cohorts (**Fig. 4.6B-E**). In addition, µCT analyses of the mandibles demonstrated

that GANT58-MP treatment prevented trabecular bone loss in both cohorts compared to control (**Fig. 4.6F-G**). Immunohistological analyses also showed a significant decrease in intratumoral PTHrP protein levels with GANT58-MP treatment (**Fig. 4.6H-I**). Collectively, these findings demonstrate that inhibition of Gli2 via GANT58-MPs treatment blocks osteolytic signaling and subsequent bone invasion by tumors irrespective of their resistance to erlotinib.

4.4 Discussion

Mandibular invasion by OSCC, which accounts for over 90% of head and neck malignancies, remains a major clinical problem. Patients with bone-invasive tumors have significantly reduced survival (**Fig. 4.1D**). Current surgical procedures and chemoradiation therapies used to reduce tumor growth impede healing of damaged bone and induce bone loss, leading to increased morbidity and mortality [156-159]. While bisphosphonates and RANKL inhibitors increase time to adverse SREs in patients with bone metastases, these agents are contraindicated for OSCC patients due to medication-related osteonecrosis of the jaw (MRONJ) [160].

Until recently, the EGFR monoclonal antibody cetuximab was the only approved targeted therapy for patients with recurrent and/or metastatic oral cancer [165-168]. Several other anti-EGFR therapies, primarily tyrosine kinase inhibitors (TKIs) (e.g., erlotinib, gefitinib, afatinib), are currently being evaluated in clinical trials. However, these EGFR inhibitors have demonstrated little to no efficacy as monotherapies or in combination with conventional chemotherapy and radiation treatments due to acquired resistant mechanisms [170, 171].

Several studies have established cooperative EGFR and Hh signaling in various cancer types including basal cell carcinoma, pancreatic, and prostate cancer [186-189], but failed to

investigate how these pathways intersect to promote bone invasion or metastasis. Similarly, previous reports have illustrated that exogenous treatment with EGF stimulates PTHrP expression by breast, prostate, lung, and oral cancer cells, but these studies were conducted *in vitro* and did not establish Gli transcription as a mediator of this signaling [161, 162]. The current study demonstrates for the first time that EGFR regulates Gli2-mediated transcription of PTHrP to promote bone invasion by OSCC. We show that inhibition of Gli2 using the small-molecule inhibitor GANT58 not only reduces EGF-stimulated PTHrP expression (**Fig. 4.5**) but also attenuates bone destruction by tumors *in vivo* (**Fig. 4.6**).

Since there are no viable treatment options available for patients who have developed resistance to EGFR-directed inhibitors, we wanted to investigate whether targeting Gli2 could also block bone invasion in this patient population. We chose to use the EGFR TKI erlotinib to generate resistant cells instead of cetuximab because we wanted to establish an aggressive experimental model. A previous study demonstrated that cells with acquired resistance to cetuximab maintained dependence on EGFR signaling and were sensitive to treatment with erlotinib [190]. We found that erlotinib-resistant C27R cells maintained Gli2 expression by reactivating the downstream kinases pAKT and pERK independently of EGFR in order to induce PTHrP expression (**Fig. 4.3, Fig. S4.3**). C27R tumors were slower growing but appeared to have a more aggressive osteolytic phenotype *in vivo*; still, treatment with GANT58-MPs effectively reduced bone destruction induced by these tumors (**Fig. 4.6**). This finding further emphasizes the therapeutic potential of Gli inhibition in bone-invasive OSCC.

Previous studies have implicated EMT as a mechanism of resistance to EGFR-targeted therapies [170, 171]. EMT involves the accumulation of genetic mutations that disrupt epithelial cell-cell adhesions, resulting in loss of cell polarity and acquisition of a spindle, stem-like

phenotype. We observed that erlotinib-sensitive CAL27 cells maintained their epithelial morphology while the erlotinib-resistant C27R cells adopted a mesenchymal morphology (**Fig. 4.3**). Furthermore, our RNA seq results showed that *CDH1* (epithelial marker) and *VIM* (mesenchymal marker) were upregulated in the CAL27 and C27R cells, respectively (**Fig. 4.4**). Together, these finding suggest that EMT may be an additional mechanism of resistance to erlotinib in bone-invasive OSCC, but this warrants further investigation. It may also be interesting to explore whether targeting EMT stimulates a reversal of this phenotype and re-sensitizes C27R cells to EGFR inhibition.

We saw a significant decrease in PTHrP expression with GANT58 treatment as measured by qRT-PCR and immunohistochemistry in both CAL27 and C27R cells (**Fig. 4.5-6**). This reduction in PTHrP explains, in part, the bone protective effect observed with GANT58 treatment in both cell lines (**Fig.4.6**). However, our RNA seq analyses revealed that GANT58 alters the expression of several genes in the mevalonate (MVA) pathway as well as others with roles in cholesterol biosynthesis (**Fig. 4.4**). Bisphosphonates, which are standard-of-care for patients with metastatic bone malignancies, disrupt the MVA pathway in osteoclasts to block bone resorption [184, 185]. Future studies should evaluate the direct effects of GANT58 on osteoclast-mediated bone resorption.

Lastly, GANT58 treatment inhibited tumor proliferation of both CAL27 and C27R cells *in vitro* but did not reduce tumor burden *in vivo.* This finding is consistent with our previous studies in a model of bone-metastatic breast cancer [174, 175] and other reports demonstrating that GANT58 inhibits tumor proliferation by inducing cytostasis (cell cycle arrest) and early phase apoptosis rather than direct cytotoxic killing [35, 97, 141]. Thus, rather than delivering GANT58 as a single agent, coadministration with a low-dose chemotherapy or another molecular therapy

(e.g., anti-pAKT, anti-pERK inhibitor) may improve its efficacy against both erlotinib-sensitive and -resistant OSCC tumors *in vivo*.

4.5 Supplementary Data

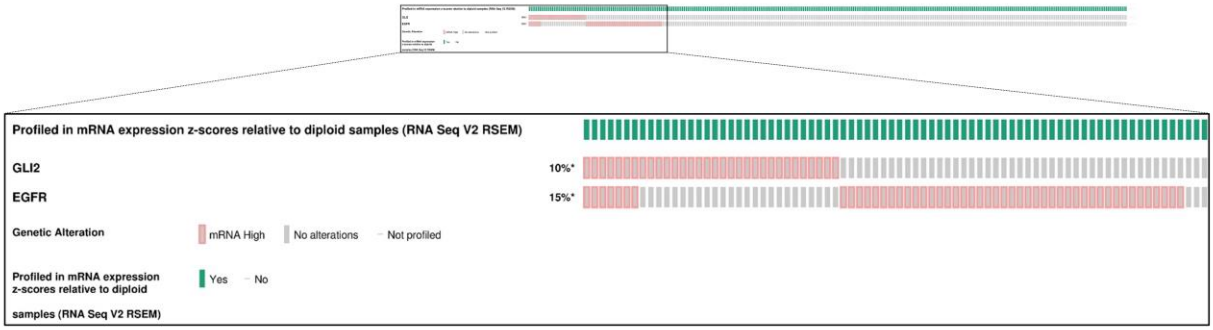

Fig. S4.1. Genetic alterations of EGFR and GLI2 in OSCC patient tumors from the TCGA PanCancer Atlas dataset.

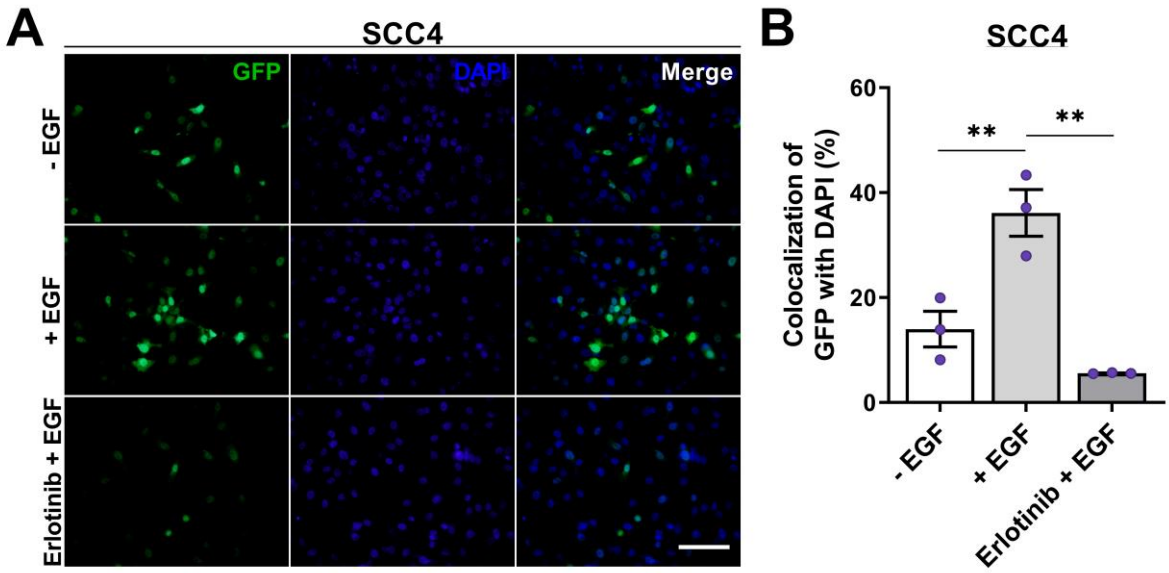

Fig. S4.2. EGFR signaling modulates Gli2 DNA-binding activity in OSCC. (A) Representative immunofluorescent images and **(B)** quantification of GFP colocalized with DAPI staining in SCC4 cells transfected with the pGL3b-8XGliBS:EGFP reporter after treatment with DMSO (-EGF), 10 ng/ml rhEGF (+EGF), or a combination of rhEGF and 5 μM erlotinib (Erlotinib + EGF) for 48 hr. Scale bar: 100 μm. n = 3 biological replicates.

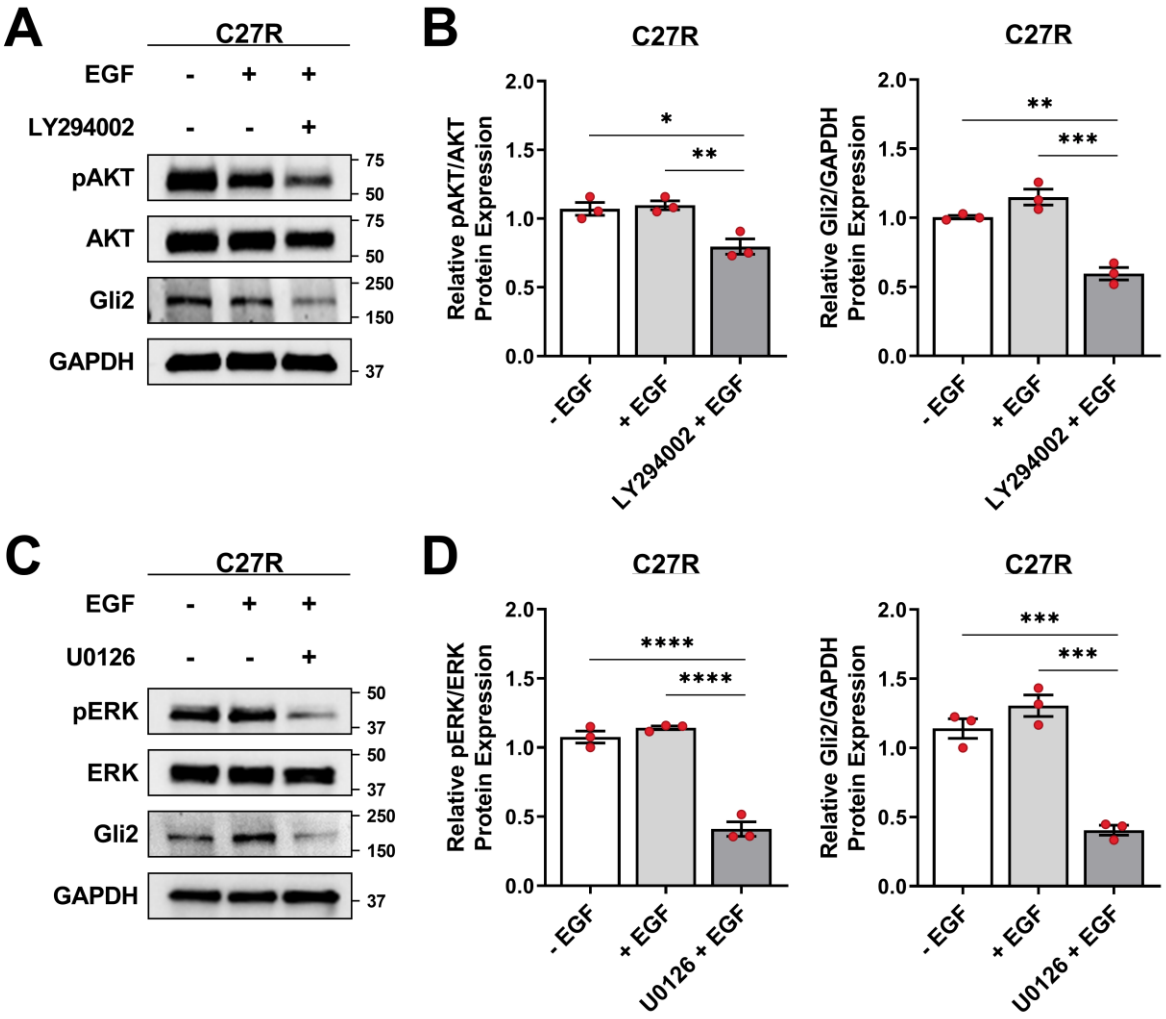

Fig. S4.3. Downstream kinases modulate Gli2 expression in erlotinib-resistant cells. (A) Representative western blots and **(B)** quantification of phosphorylated AKT and Gli2 protein in C27R cells treated with DMSO (-EGF), 10 ng/ml rhEGF (+EGF), or a combination of rhEGF and 50 μM LY294002 (LY294002 + EGF) for 48 hr. **(C)** Representative western blots and **(D)** quantification of phosphorylated ERK and Gli2 protein in C27R cells treated with DMSO (-EGF), 10 ng/ml rhEGF (+EGF), or a combination of rhEGF and 5 μM U0126 (U0126 + EGF) for 48 hr.

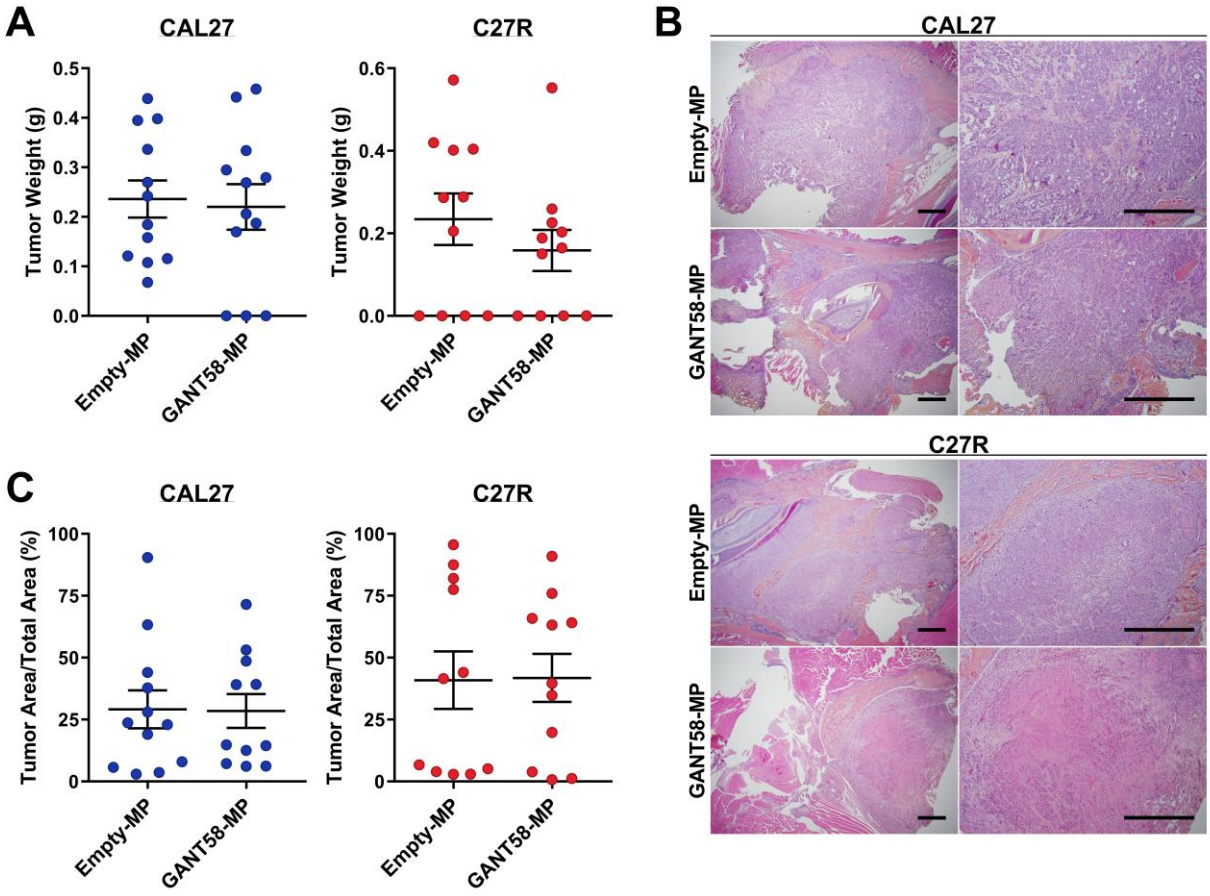

Fig. S4.4. GANT58-MP treatment does not reduce tumor burden. (A) Tumor weights of Empty-MP and GANT58-MP treated at sacrifice. **(B)** Representative H&E stained sections and **(C)** histomorphometric analysis of tumor area in Empty-MP and GANT58-MP treated in mice inoculated with either CAL27 or C27R cells. Scale bars: 500 µm.

CHAPTER 5

ENGINEERING 3D MODELS OF TUMORS AND BONE TO UNDERSTAND TUMOR-INDUCED BONE DISEASE AND IMPROVE TREATMENTS

Adapted from: **Kwakwa KA***, Vanderburgh JP, Guelcher SA, Sterling JA. Engineering 3D Models of Tumors and Bone to Understand Tumor-Induced Bone Disease and Improve Treatments. *Curr Osteoporos Rep.* 2017; 5:247-254.

5.1 Abstract

Purpose of Review: Bone is a structurally unique microenvironment that presents many challenges for the development of 3D models for studying bone physiology and diseases, including cancer. As researchers continue to investigate the interactions within the bone microenvironment, the development of 3D models of bone has become critical.

Recent Findings: 3D models have been developed that replicate some properties of bone, but have not fully reproduced the complex structural and cellular composition of the bone microenvironment. This review will discuss 3D models including polyurethane, silk, and collagen scaffolds that have been developed to study tumor-induced bone disease. In addition, we discuss 3D printing techniques used to better replicate the structure of bone.

Summary: 3D models that better replicate the bone microenvironment will help researchers better understand the dynamic interactions between tumors and the bone microenvironment, ultimately leading to better models for testing therapeutics and predicting patient outcomes.

5.2 Introduction

Tumor cells frequently reside in the bone microenvironment due to primary (osteosarcomas), invasive (melanoma, myeloma), or metastatic disease (breast, prostate, lung, and

renal cancers). Once tumors establish in bone, they interact with the physical microenvironment as well as the resident bone cells to cause bone destruction known as tumor-induced bone disease. While these interactions have been well-established by *in vitro* and *in vivo* studies, it has been challenging to investigate dynamic tumor-bone interactions due to a lack of appropriate 3D models. Thus, many groups have developed new models for studying tumor-induced bone disease that use both tumor cells and bone-resident cells (osteoblasts, osteoclasts). The development of these models has relied heavily on collaborations between biologists, clinicians, and engineers. These 3D models have allowed scientists to better understand the signaling pathways that drive tumor-induced bone disease, the interactions between different cell types, and the influence of the physical bone microenvironment. Furthermore, these models can serve as valuable platforms for the discovery and development of novel therapeutics to target tumors in bone. In this review, we will briefly discuss common 3D culture methods used in cancer research (hydrogels, spheroids) while focusing on current 3D models for studying bone and tumor metastasis to bone, specifically tissue-engineered constructs (TECs).

5.3 3D Cancer Models

Since its development in the late 19th century, cell culture has remained an important tool for both basic biology and medical research, including cancer research. Most adherent tumor cells are cultured as a monolayer on two-dimensional (2D) substrates made of polystyrene plastic or glass. Although 2D culture systems are widely used in cancer research, an increasing body of evidence has shown that 2D cell culture does not adequately replicate the complex interactions and spatial organization of cells in the three-dimensional (3D) tumor microenvironment. Moreover, tumor cell behavior (proliferation, migration, gene expression) and response to drug

treatment can differ dramatically in conventional 2D culture compared to *in vivo* cellular responses [191-193]. To address some of these limitations, several 3D cell culture systems have been developed in the last few decades and the adoption of these methods in cancer cell biology is rapidly increasing. Cancer cells grown in 3D more closely resemble those in the tumor microenvironment and thus, have more physiologically relevant responses. To date, the most common 3D cell culture methods in cancer research include extracellular matrix (ECM)-based hydrogels and tumor spheroids.

Hydrogels

Due to their soft tissue-like properties, hydrogels have been increasingly used to mimic the 3D extracellular matrix (ECM) of solid tumors including breast, prostate, lung, and colorectal cancers [194-197]. Hydrogels are comprised of crosslinked polymer networks derived from natural or synthetic materials. Natural hydrogels are typically formed from ECM proteins like collagen, laminin, and fibrin as well as other matrix components like hyaluronic acid [198, 199]. Collagen type I is a commonly used natural hydrogel since it is the most abundant ECM protein in tumor stroma and has been shown to support tumor growth and increase the expression of genes promoting malignant phenotypes [200, 201]. The commercially available Corning® Matrigel® matrix is perhaps the most widely used natural ECM-based hydrogel for 3D culture of tumor cells in vitro. Matrigel® is a reconstituted basement membrane isolated from murine Engelbreth-Holm-Swarm (EHS) sarcoma which contains various ECM proteins (e.g., laminin, collagen IV, heparin sulfate proteoglycans) and endogenous growth factors (e.g., TGF-β, EGF, IGF-1, PDGF) [202]. These gels are highly biocompatible and not only modulate tumor cell viability, proliferation, adhesion, and motility, but also sensitivity to therapeutic agents [203]. However, the concentration

of proteins and growth factors in natural hydrogels can vary between batches and confounding factors such as undefined matrix components can influence tumor cell behavior [204].

Alternatively, hydrogels made from synthetic materials such as poly(ethylene glycol) (PEG), poly(lactic acid) (PLA), and poly(vinyl alcohol) (PVA) have relatively well-defined structures with tunable chemical compositions and mechanical properties (e.g., stiffness) [205, 206]. Synthetic hydrogels also provide 3D architectural support for tumor cells and have been shown to maintain cell viability even in the absence of endogenous matrix components; however, these gels are usually supplemented with ECM proteins, growth factors, and other bioactive molecules in order to optimize tumor cell growth and survival [207-209]. Both natural and synthetic hydrogels can be used alone or in combination with other 3D culture methods including tumor spheroids.

Tumor Spheroids

In contrast to 2D monolayers, adherent tumor cells cultured in 3D tend to self-assemble into multicellular aggregates known as spheroids. Tumor spheroids are more mimetic of solid tumors *in vivo* with respect to cellular heterogeneity, metabolic and proliferative gradients, and gene expression. Specifically, spheroids typically contain a well-oxygenated outer layer of proliferating cells, a hypoxic inner layer of quiescent cells, and a necrotic core [210, 211]. Multicellular spheroids may consist of tumor cells alone or as co-cultures with stromal, endothelial, and immune cells. The 3D cell culture methods used to generate tumor spheroids include both scaffold-based (e.g., hydrogels) and scaffold-free (e.g., forced floating, hanging drop) platforms.

Scaffold-based methods for spheroid growth involve embedding or encapsulating tumor cells within natural or synthetic hydrogels that mimic the ECM. As previously discussed, the presence of endogenous matrix proteins and growth factors in these gel matrices not only support the organization of tumor cells into 3D spheroids, but also promote the formation of migratory and invasive structures, significantly alter gene expression patterns, and affect cellular response to anti-tumor drugs [194-197].

On the other hand, scaffold-free platforms do not use a gel matrix support. Tumor spheroids produced by these methods are generated in suspension culture. One relatively simple approach is the force floating method which utilizes an ultra-low attachment plate to prevent tumor cell adhesion to the surface. Instead, cells aggregate to form multicellular spheroids [212, 213]. Another scaffold-free approach is the hanging drop method during which tumor cells in suspension aggregate into spheroids under gravity. Specifically, small aliquots of cell suspension are dispensed onto a Petri dish lid that is subsequently inverted to allow droplets to hang [214]. Various spheroid culture array plates have also been developed to better stabilize hanging drops [215, 216]. This 3D tumor culture model generates a large number of spheroids with uniform size and morphology which is suitable for biochemical assays and high-throughput screening of therapeutics [215, 217, 218].

Limitations of 3D Cancer Models for Bone

Tumors originating in the breast, prostate, and lung frequently metastasize to other organs, including bone [3, 219]. In addition to interacting with bone-resident cells, tumor cells also come into contact with the mineralized bone matrix, which is orders of magnitude more rigid than soft tissues [40, 43]. Simple 3D models like hydrogels and tumor spheroids improve upon 2D culture

methods used to investigate soft tissue tumors and provide structural support for 3D cell growth and adhesion that resembles that of cells in their native environment. However, these approaches fail to recapitulate the mechanical and physical properties of bone which should be considered when investigating tumor interactions with bone, especially mechanically responsive genes. Tissue engineering and scaffolding approaches have been employed to develop biomimetic 3D constructs in order to study metastatic tumors in bone. In fact, hydrogels and other organic ECM components are often combined with more rigid scaffolding materials like ceramics, polymers, and composites to better mimic the bone microenvironment (discussed later in this review).

5.4 3D Bone Models

The field of bone tissue engineering has traditionally been focused on regenerating or repairing bone through the development of bone tissue-engineered constructs (TECs). However, advances toward creating TECs for *in vivo* applications have led to progress in designing biomimetic *in vitro* models for studying bone biology, disease progression, and drug screening in the bone microenvironment. 3D *in vitro* bone models have been proposed to aid in bridging the gap between 2D culture and animal models for diseases and medical conditions such as osteomyelitis [220], bone fracture healing [221, 222], and, as will be discussed in this review, tumor metastases. In designing such TECs, studies investigating properties of the constructs indicated that characteristics including rigidity [43, 223], pore size [224, 225], pore shape [226], and curvature [227] all affect cell behavior. Tissue engineers have been working toward creating TECs with precisely controlled physicochemical, mechanical, and structural properties that not only replicate human bone, but also allow for the systematic and parametric study of how these factors influence disease progression and drug response.

Materials & Fabrication Methods

The first step in engineering *in vitro* models is designing the appropriate construct considering the *in vivo* microenvironment of interest. Bone stands apart from other non-mineralized tissues in that the rigidity of bone ($1.7–2.9 \times 10^{10}$ Pa) is orders of magnitude higher than soft tissues ($10^2–10^6$ Pa) [40, 41]. This unique rigidity necessitates TECs with high mechanical properties not attainable by hydrogels and other ECM-mimicking materials. On the other hand, materials used for cancer models vary widely depending on the origin of the tumor, and would ideally exhibit an angiogenic capacity [228, 229]. Thus, in designing TECs for bone applications and 3D cancer models, engineers employ various materials and fabrication methods to create biomimetic matrices on which appropriate cell populations may be cultured.

First and foremost, materials must be biocompatible to avoid eliciting adverse cell responses *in vitro*. Since cells can sense and respond to the matrix, these biocompatible materials are carefully chosen for characteristics that will have the desired effect on the cell populations to be introduced. Mechanical properties, bioactivity, biodegradability, and chemical composition are characteristics that must be considered when choosing TEC materials for cancer and bone modeling alike. The robust mechanical properties of materials like ceramics, metals, polymers, and composites have rendered them the predominant materials used in fabricating bone TECs. While 3D models for soft tissue tumors are not necessarily subjected to the stringent rigidity restrictions, conferring ECM-like properties and surface modifications with specific proteins and growth factors are desirable to mimic the cancer microenvironment [230].

Synthetic Materials

Multiple poly(α-esters) have been used extensively in bone tissue engineering and for cancer models including poly(caprolactone) (PCL) [231-233], PLA [234, 235], and poly(lactic-co-glycolic acid) (PLGA) [236, 237]. These are biocompatible and biodegradable polymers that have other biomaterial applications such as drug delivery. They have also been combined with hydroxyapatite and other ceramics to create composite materials that exhibit more bone-like qualities [238]. However, these materials have drawbacks that can limit their effectiveness in bone applications including slow degradation time (PCL), low mechanical properties (PLGA), and low cell adhesion. Polyurethanes (PUR) are a good alternative due to their tunable rigidity, biodegradability, and physicochemical properties [239]. Furthermore, the ease of PUR processing, high mechanical properties, and biostability makes them attractive materials for biomedical bone implants and other bone-mimicking materials. Poly(propylene fumarate) (PPF) has also been incorporated into TECs due to their biocompatibility, biodegradability, and high mechanical properties [240, 241].

Natural Materials

Natural materials have been employed for bone TEC applications as well. Collagen is a versatile material that has obvious appeal for bone applications as it is the main protein constituent of bone and comprises ~10% of bone matrix [12]. Collagen can be prepared into cross-linked solids or gels with varying mechanical properties and is intrinsically resorbable and bioactive. This makes collagen useful for a variety of applications including bone TECs, skin grafts, hydrogels, and sponges for wound healing [242]. Hydroxyapatite (HA) constitutes 50-70% of bone; therefore, HA and other calcium phosphate materials are also appealing for bone applications. Since HA is a ceramic material and not easily formed into 3D structures by conventional means, it is often

combined with polymeric materials to create composites that impart both the osteoinductive benefits of HA along with the malleability of polymers. These main components of bone are enticing materials to use for bone TECs due to their physiologic relevance, however, other natural materials have been pursued as bone-like substrates. Silk is another biomaterial used in several biomedical applications because of its mechanical properties and versatility through its receptivity to chemical modifications. Silk can be molecularly engineered to confer specific properties onto the material such as cellular recognition and mineralization, and multiple studies have utilized silk as a biomaterial for studying bone metastases [243-245]. Researchers have even used bone cells alone to create TECs for studying cancer progression. In one such study, an osteoid matrix was constructed by long-term culture of osteoblasts in a bioreactor system prior to co-culture with tumor cells [246].

Creating 3D Bone Morphology

In addition to substrate properties, it is important that biomaterials are able to be manipulated into relevant structures and 3D morphologies. Traditional methods to fabricate porous TECs from natural or synthetic polymers includes gas foaming [247, 248], particulate leaching [238, 249, 250], or freeze-drying [236, 251]. While these methods are effective in creating porous scaffolds, they lack the control necessary to create specific architectures.

As the importance of structural properties on which cells are grown becomes more evident, biologists and engineers have looked to new avenues for creating TECs with well-defined architectures. Additive manufacturing (AM), also known as 3D printing, is perhaps the most widely used new technology for creating TECs due to its unparalleled ability to create precisely controlled geometries at increasingly fast speeds [252]. AM, defined as the layer-by-layer

fabrication of parts directed by digital information from a 3D computer-aided design file, is an umbrella term that describes multiple methods for creating 3D constructs. These methods include fused-deposition modeling [117, 253], stereolithography [235, 254], material jetting (inkjetting) [255], and bioprinting [256, 257]. Other AM methods such as selective laser sintering (SLS) have also been implicated for use in biomaterials applications.

In addition to creating TECs with the appropriate physicochemical, structural, and mechanical properties, researchers are using bioreactors to more closely mimic physiologic flow conditions experience by cells *in vivo*. To do this, media is perfused through the TECs and circulated within the system, often using a peristaltic pump. Perfusion culture allows cells to experience physiologic shear conditions which are known to affect cell behavior [258]. Furthermore, perfusion culture allows for the flow of nutrients and other soluble factors that can keep cells viable for longer durations.

5.5 3D Bone-Tumor Models

Collaborations between biologists and engineers have fostered the combining of the discussed biomaterials and fabrication methods to create 3D bone-tumor models using TECs. These biomimetic models not only aim to confer the appropriate cell-cell interactions, but also the appropriate cell-matrix interactions through the creation of TECs with precisely controlled properties that more closely replicate the *in vivo* bone-tumor milieu.

One such study employed a 3D bioreactor culture system to first create a mineralized, multi-layered tissue of osteoblasts and subsequently co-cultured with osteoclasts and metastatic tumor cells to investigate tumor effect on matrix degradation [259]. To create the 3D matrix, MC3T3-E1 murine osteoblasts were cultured for up to 10 months to create a 3D osteoid matrix.

Osteoclasts were then introduced to the 3D culture, and subsequent matrix degradation was observed. After addition of fresh MC3T3-E1s, the matrix was reformed, thereby suggesting that bone remodeling was occurring. Finally, metastatic MDA-MB-231 breast cancer cells were added to the 3D co-culture system. By confocal microscopy, it was observed that the cancer cells migrated towards sites of active remodeling which led to further degradation of the matrix. This study not only demonstrates the ability to study the bone remodeling process in vitro but also how this process can be disrupted in a diseased state. This system is also amenable to clinically-relevant drug screening since it has a measurable physical outcome (matrix degradation).

In another high-impact study, porous silk fibroin scaffolds prepared directly from the silk fibroin protein of silkworms [260], were used in a 3D culture system to investigate the response of metastatic tumor cells to external stimuli in the presence of osteoblasts and mesenchymal stem cells (MSC) [261]. The silk fibroin scaffolds were hypothesized to be an ideal scaffold for investigating metastatic breast cancer behavior due to its mechanical properties in the range of adipose breast cancer in breast cancer patients, its inherent possession of Asp-Gly-Asp (RGD) peptide sequences known to promote cytocompatibility and cell adhesion, and based on the results of previous studies showing that MSCs undergo osteogenic differentiation on the scaffolds. Co-culture of MG-63 human osteoblast-like cells and MDA-MB-231 human breast cancer cells on the silk scaffolds resulted in a decrease in MG-63 population compared to that of the MDA-MB-231 despite being seeded at a 1:1 ratio. This suggests that the breast cancer cells were inhibiting growth of the osteoblasts, a finding that is supported by previous studies [262]. To take these findings a step further, the effect of the breast cancer cells on matrix mineralization was investigated using the same co-culture. Alizarin red staining and alkaline phosphatase activity indicated that matrix mineralization was lower on the scaffolds containing the breast cancer cells, further confirming

the effect of tumor cells on osteoblast viability and function. Further studies in this system indicated that the co-culture significantly increases drug resistance, invasiveness, and angiogenesis.

In a more recent study from the same group, a similar 3D system utilizing silk fibroin scaffolds was used to screen anticancer drugs to understand its effect on the cellular interactions of the co-culture of MDA-MD-231 breast cancer cells and MG-63 osteoblastic cells [263]. A targeted nanoparticle (NP) formulation for the anticancer drug, doxorubicin, was developed using a folate-conjugated silk fibroin polymer. This formulation was then introduced into the 3D co-culture system to test the efficacy of the drug *in vitro* as well as its targeting ability. After 14 days of co-culture, the viability of the cancer cells decreased while osteoblast morphology and density was not much affected by the presence of doxorubicin. Also noted was the IC_{50} of the doxorubicin which was 10-fold higher in the 3D system than 2D, thus illustrating that tumor cell response to drugs can be drastically different in 3D compared to 2D. Further, they found that drug treatment reduced vascular endothelial growth factor (VEGF) expression and glucose consumption, suggesting a down-regulation of angiogenic factors and slowed proliferation of cancer cells, respectively. While the effect of the targeted NP formulation did not necessarily produce notably improved results over free doxorubicin, this study shows that the 3D co-culture system is capable of screening anticancer drugs and outcomes in 3D are notably different than in 2D.

Other studies have incorporated mechanical loading into the model to test how mechanical stress affects bone and cancer cell behavior. One such study employed HA-containing PLGA scaffolds under cyclic compression to investigate the interactions between MDA-MB-231 breast cancer cells and human bone marrow-derived mesenchymal stem cells (hBM-MSCs) in the mechanically stressed environment [264]. Before investigating mechanical loading, HA-

containing scaffolds were seeded with hBM-MSCs and treated with tumor-conditioned media to observe how tumor-derived soluble factors influence osteogenic behavior. Interestingly, it was found that alkaline phosphatase (ALP) activity increased in the presence of tumor-conditioned media. This finding runs contrary to previous findings concluding that tumors tend to inhibit osteogenic differentiation. The authors suggest this could be a result of the early timing at which the hBM-MSCs were exposed to the conditioned media. Upon cyclic compression of HA-containing scaffolds seeded with hBM-MSCs and supplemented with conditioned media from mechanically loaded MDA-MD-231, there was no notable effect on ALP activity as seen in the non-loaded case. However, gene expression of the osteogenic marker osteopontin (OPN) significantly increased when the hBM-MSCs and MDA-MB-231s were mechanically loaded, and these findings were corroborated by measuring OPN protein levels. These data suggest that mechanical loading influences the interaction between hBM-MSCs and tumor cells through modulation of OPN levels. This study stresses the important role mechanical loading plays in bone-tumor interactions, which emphasizes the need to further investigate the effects of dynamic mechanical forces on tumor progression in bone.

As stated earlier, additive manufacturing has become a valuable tool for *in vitro* modeling due to its ability to create precise 3D geometries. Considering that bone has a complex and intricate structure, it is perhaps not surprising that 3D printing has started to influence 3D bone-tumor modeling. A recent study utilized a stereolithography 3D printing technique to create HA-composite scaffolds for modeling breast cancer bone metastases [265]. First, a PEG-based ink was printed into several pore geometries including square and hexagonal. After choosing the optimal geometry (small square pores) based on cell proliferation of MDA-MB-231 cells, HA was incorporated into the PEG ink (10% HA) and printed. The breast cancer cells grown on the HA-

containing scaffolds proliferated significantly faster than the non-HA scaffolds, suggesting the HA component of bone promotes tumor proliferation. To study tumor cell migration on the HA-containing scaffolds, a non-metastatic breast cancer cell line (MCF-7) was also introduced and compared to the MDA-MB-231 cells. MDA-MB-231 cells cultured on the matrices migrated significantly farther than the MCF-7 in both the HA and non-HA scaffolds. They further tested the efficacy of the chemotherapeutic 5-FU in both the 3D and 2D environment. While 5-FU treatment did show efficacy in both environments, the efficacy was significantly less in 3D culture than in 2D. This study highlights the potential impact that 3D printing can have in *in vitro* modeling. It is evident from this study that curvature affects cell proliferation, therefore, it can be conjectured that 3D architecture may play an important role in tumor progression in bone.

5.6 Future of 3D Models

3D models have drastically improved over the past 5 years. However, existing 3D bone models only focus on a few aspects of the bone microenvironment. As researchers continue to study this niche, models will not only begin to incorporate more physical properties (rigidity, fluid flow, compression, pore size) but also different cell types (osteoblasts, osteoclasts, endothelial cells, fibroblasts, immune cells) (**Fig. 5.1**). This will be an exceedingly complex undertaking that will likely take many years to accomplish as well as a variety of expertise from different groups. Additionally, researchers have begun modeling dynamic cellular interactions and processes in bone using computational models in order to develop a more complete understanding of the bone microenvironment and to predict outcomes [266, 267]. These dynamic 3D models will significantly improve our ability to screen and develop new drugs to treat bone diseases including

tumor-induced bone disease. One important objective is to increase usage of patient-derived cells in these 3D models to help predict patient outcomes to novel therapeutics.

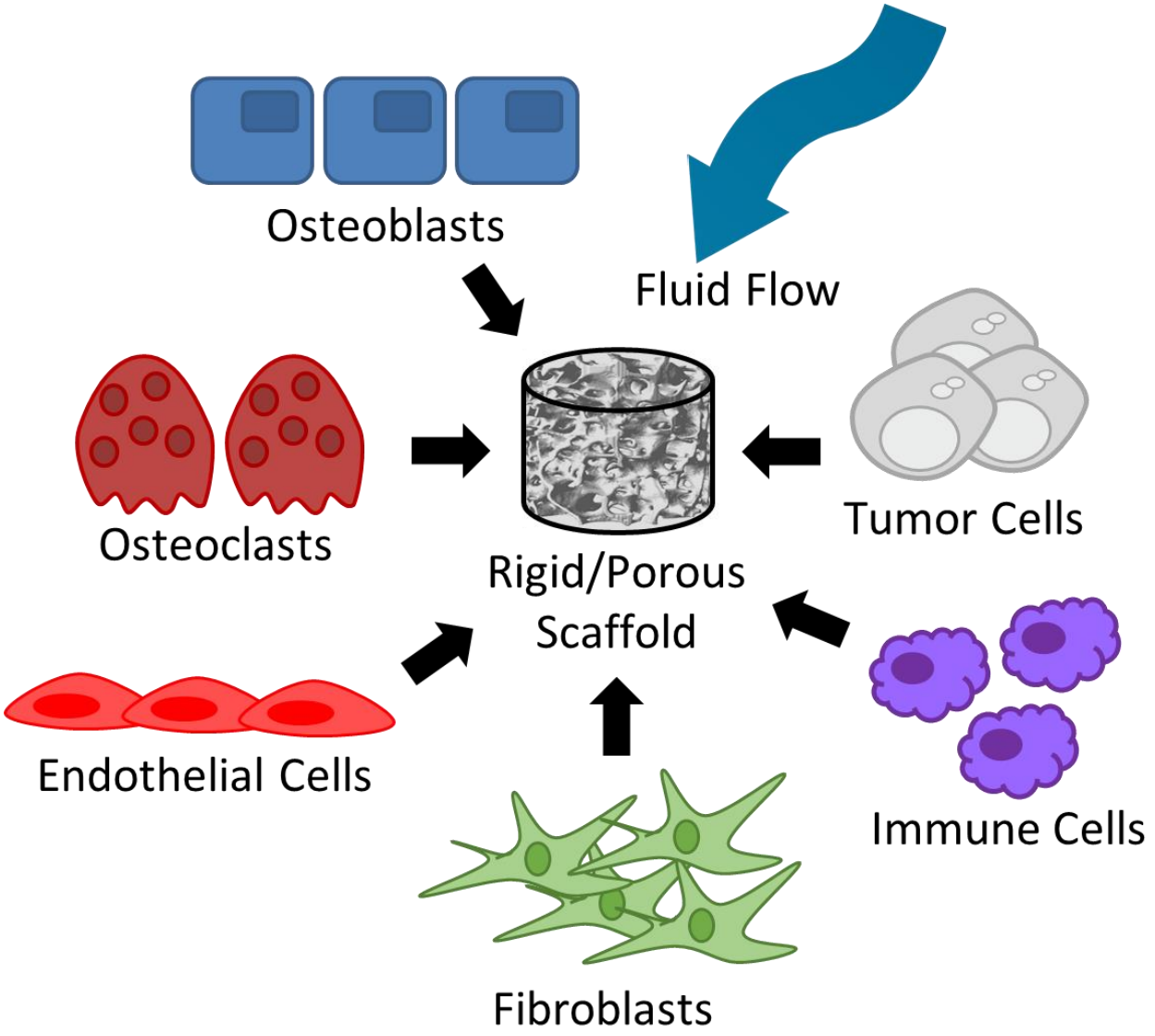

Fig. 5.1. Future of 3D models. The incorporation of additional physical and cellular components in 3D bone models will help increase our understanding of the dynamic interactions in the bone microenvironment.

APPENDIX

THE PHYSICAL BONE MICROENVIRONMENT MODULATES OSTEOLYTIC GENE EXPRESSION IN METASTATIC CANCERS

The bone microenvironment provides a fertile niche for metastatic cancer cells due to its abundance of soluble factors such as transforming growth factor beta (TGF-β). Our group has previously established that TGF-β stimulates bone-metastatic cells to overexpress the Hedgehog transcription factor Gli2, which induces parathyroid hormone-related protein (PTHrP) expression and osteoclast-mediated bone destruction [26, 28, 34]. However, gene expression is not solely regulated by soluble growth factors. Our investigations show that matrix rigidity also regulates tumor cell expression of Gli2, PTHrP, and the mechanosensitive gene integrin beta 3 (ITGB3) [16, 40, 43, 268]. Specifically, metastatic breast, prostate, and lung cancer cells cultured on rigid 2D polyurethane films express significantly higher levels of Gli2, PTHrP, and ITGB3 compared to cells on compliant films [43]. In addition, we recently demonstrated that the pore size of 3D t-FDM scaffolds alters tumor cell motility, gene expression and drug response [268]. Therefore, we hypothesized that the 3D architecture of trabecular bone modulates osteolytic gene expression in tumor cells to promote a bone-destructive phenotype. To test this, we created novel 3D tissue-engineered bone constructs (TEBCs) that mimic the trabecular structure of human bone at different anatomical sites including the femur, tibia, and vertebrae [252]. Bone-metastatic breast (MDA-MB-231), prostate (PC3), and lung (RWGT2) cancer cells cultured on these 3D scaffolds differentially express the osteolytic genes Gli2, PTHrP, and ITGB3 compared to that of cells seeded on a standard scaffold with uniform pore size (**Fig. 6.1**). These data indicate that bone microarchitecture regulates gene expression in metastatic cancer cells and underscores the

potential of the physical bone microenvironment to promote cancer-induced osteolysis. A better understanding of tumor cell behavior in the bone microenvironment may help researchers develop new therapies to treat tumor-induced bone disease.

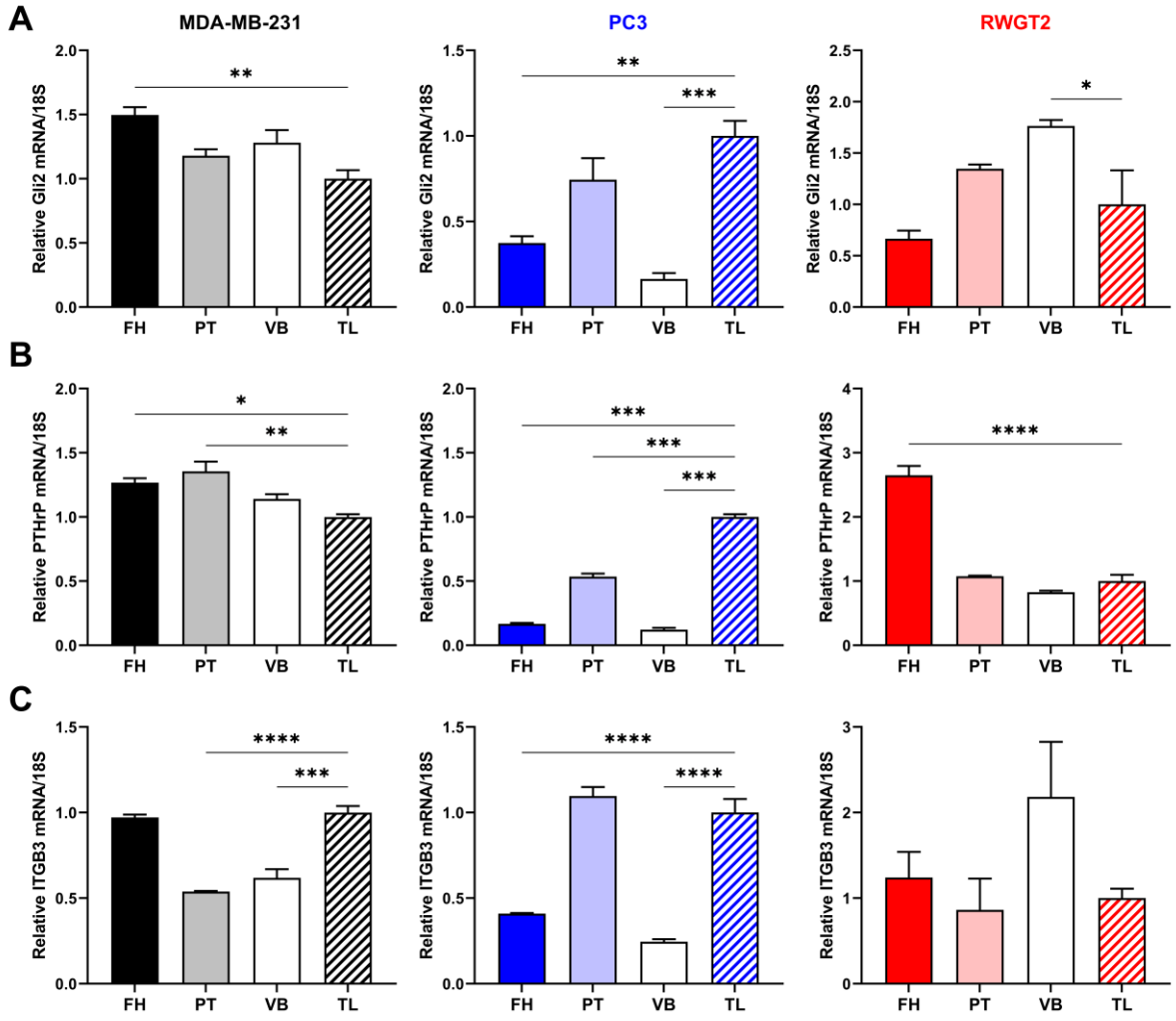

Fig. 6.1. Tumor cells differentially express osteolytic genes on distinct trabecular architectures. MDA-MB-231, PC3, and RWGT2 cells cultured on TEBCs with different trabecular architectures for 24 hours differentially express **(A)** Gli2, **(B)** PTHrP, and **(C)** ITGB3 mRNA as measured by qPCR. TEBCs are FH=femoral head, PT=proximal tibia, and VB=vertebral body. Scaffold with uniform pore size is tube-like=TL.

SUMMARY AND FUTURE DIRECTIONS

"What is it that decides what organs shall suffer in a case of disseminated cancer?"

– Stephen Paget

Although five-year survival rates have improved over the past decade for most tumor types, metastatic disease remains a leading cause of cancer-related deaths. Advanced breast, prostate, and lung cancers frequently metastasize to bone. Likewise, cancers originating in the oral cavity often invade bony structures such as the mandible and maxilla. Once established in bone, tumors initiate a vicious cycle of malignant growth and bone destruction known as tumor-induced bone disease (TIBD) [16-18].

The standard-of-care for patients with TIBD includes chemotherapy, radiation, and anti-resorptive therapies. While conventional chemoradiation therapies inhibit tumor growth, these treatments are also extremely damaging to healthy bone marrow cells [94, 95, 157-159]. Anti-resorptive agents such as bisphosphonates and denosumab effectively reduce osteolytic bone destruction but do not eliminate tumor burden; thus, patients still suffer from adverse skeletal-related events [5, 6]. Moreover, these agents are contraindicated for some patients due to complications associated with osteonecrosis of the jaw [91, 92, 160]. Therefore, new targeted therapies that block bone destruction are needed to improve outcomes.

Our lab previously identified the Hedgehog (Hh) transcription factor Gli2 as a promising therapeutic target for TIBD. We demonstrated that Gli2 regulates expression of the osteolytic factor parathyroid hormone-related protein (PTHrP) to promote bone destruction. In contrast, tumor-induced osteolysis was attenuated by genetic inhibition of Gli2 [26, 28, 172]. Since transcription factors have historically been regarded as "undruggable" [269], pharmacological

inhibitors targeting Gli-mediated transcription were initially developed against the Hh signaling receptor Smoothened (Smo). However, Smo inhibitors had limited success in clinical trials, which may be attributed to acquired receptor mutations and/or non-canonical pathway activation (**Ch. 2 and 4**) [29, 32, 33]. Fortunately, several small molecule Gli inhibitors have been identified in recent years [35, 36]. We hypothesized that directly inhibiting Gli downstream of Smo would be more effective at preventing osteolysis.

My thesis work primarily focused on testing the Gli-antagonist GANT58 in preclinical models to determine its efficacy against tumor-induced bone destruction (**Ch. 3 and 4**). GANT58 treatment reduced PTHrP expression *in vitro* but was largely ineffective against bone-residing tumors due to its low water solubility. In order to improve its bioavailability *in vivo*, we encapsulated GANT58 in polymeric micellar micro- (MPs) and nanoparticles (NPs) for local and systemic delivery, respectively. The resulting GANT58-NP formulation significantly decreased bone destruction in breast and lung cancer models without notable toxicity to bone marrow cells or vital organs [174]. In addition, we demonstrated that GANT58-MPs blocked mandibular invasion by oral squamous cell carcinoma (OSCC) tumors that were sensitive or resistant to the tyrosine kinase inhibitor erlotinib. Collectively, these findings suggest that Gli inhibition may be a promising therapeutic strategy for TIBD patients regardless of their tumor type or resistance status. These studies also highlight the ability of polymeric delivery systems to overcome the pharmacokinetic (PK) and toxicity limitations of otherwise promising drug candidates.

The final part of my dissertation research involved the use of 3D scaffolds to study tumor-bone interactions *in vitro* (**Ch. 5 and appendix**) [252, 270]. In this study, we seeded metastatic cancer cells on 3D tissue-engineered bone constructs (TEBCs) that recapitulate the trabecular microarchitecture of human bone at various anatomical sites including the femur, tibia, and

vertebrae [252]. Our preliminary results show that tumor cells cultured on TEBCs differentially express Gli2, PTHrP, and integrin beta 3 (ITGB3) compared to cells on tube-like scaffolds. This finding illustrates how physical properties of the bone microenvironment can modulate osteolytic gene expression and potentially influence tumor cell behavior.

"To cure sometimes, to relieve often, to comfort always."

– Edward Livingston Trudeau

Cancer is not one disease but rather a group of diseases characterized by the uncontrolled growth and spread of abnormal cells in the body. Every cancer has a unique set of mutations which varies across tumor types and between individual patients. Thus, it is unlikely that a single pharmaceutical drug will *cure* cancer. But I believe a precision medicine approach that includes combination therapies will drastically improve patient quality of life and overall survival. With regard to the clinical translation of GANT58-loaded micelles, further *in vivo* investigation is warranted to evaluate whether combination with a low-dose chemotherapeutic or molecularly targeted agent offers additional therapeutic benefit (i.e., anti-tumor effect) compared to GANT58 monotherapy. Future studies may also utilize biomimetic *in vitro* models (e.g., 3D TEBCs) to screen patient tumors and more accurately predict response to therapy.

On average, it takes over a decade for an experimental drug to be approved for use in humans [271]; however, many cancer patients cannot wait that long for new treatments. My cousin Sylvia, to whom this dissertation is dedicated to, passed away from metastatic breast cancer a few years after her diagnosis. Moving forward, more studies should focus on repurposing drugs that are FDA approved for other pathologies to determine if they are effective against neoplastic

disease. Since the PK and toxicity profiles have already been established, these drugs could quickly progress through clinical trials and be available to cancer patients in a timely manner.

REFERENCES

1. Siegel RL, Miller KD, Fuchs HE, Jemal A. Cancer statistics, 2021. CA Cancer J. Clin. 2021;71:7-33.

2. Chaffer CL, Weinberg RA. A perspective on cancer cell metastasis. Science 2011;331:1559-1564.

3. Johnson RW, Schipani E, Giaccia AJ. HIF targets in bone remodeling and metastatic disease. Pharmacol. Ther. 2015;150:169-177.

4. Mundy GR. Metastasis to bone: Causes, consequences and therapeutic opportunities. Nat. Rev. Cancer 2002;2:584-593.

5. Body JJ. Metastatic bone disease: Clinical and therapeutic aspects. Bone 1992;13:S57-S62.

6. Mundy GR. Mechanisms of bone metastasis. Cancer 1997;80:1546–1556.

7. Coleman RE. Clinical features of metastatic bone disease and risk of skeletal morbidity. Clin. Cancer Res. 2006;12:6243s-6249s.

8. Coleman R, Body JJ, Aapro M, Hadji P, Herrstedt J. Bone health in cancer patients: ESMO clinical practice guidelines. Ann. Oncol. 2014;25:iii124-iii137.

9. Baron R, Ferrari S, Russell RGG. Denosumab and bisphosphonates: Different mechanisms of action and effects. Bone 2011;48:677-692.

10. Coleman RE, Marshall H, Cameron D, Dodwell D, Burkinshaw R, Keane M, et al. Breast-cancer adjuvant therapy with zoledronic acid. N. Engl. J. Med. 2011;365:1396-1405.

11. Lipton A, Steger GG, Figueroa J, Alvarado C, Solal-Celigny P, Body JJ, et al. Extended efficacy and safety of denosumab in breast cancer patients with bone metastases not receiving prior bisphosphonate therapy. Clin. Cancer Res. 2008;14:6690-6696.

12. Clarke B. Normal bone anatomy and physiology. Clin. J. Am. Soc. Nephrol. 2008;3:S131-S139.

13. Sims NA, Martin TJ. Coupling the activities of bone formation and resorption: A multitude of signals within the basic multicellular unit. Bonekey Rep. 2014;3:481.

14. Long F. Building strong bones: Molecular regulation of the osteoblast lineage. Nat. Rev. Mol. Cell Biol. 2012;13:27-38.

15. Roodman GD. Biology of osteoclast activation in cancer. J. Clin. Oncol. 2001;19:3562-3571.

16. Sterling JA, Edwards JR, Martin TJ, Mundy GR. Advances in the biology of bone metastasis: How the skeleton affects tumor behavior. Bone 2011;48:6-15.

17. Buenrostro D, Mulcrone PL, Owens P, Sterling JA. The bone microenvironment: A fertile soil for tumor growth. Curr. Osteoporos. Rep. 2016;14:151-158.

18. Weilbaecher KN, Guise TA, McCauley LK. Cancer to bone: A fatal attraction. Nat. Rev. Cancer 2011;11:411-425.

19. Ingham PW, McMahon AP. Hedgehog signaling in animal development: Paradigms and principles. Genes Dev. 2001;15:3059-3087.

20. Briscoe J, Therond PP. The mechanisms of hedgehog signalling and its roles in development and disease. Nat. Rev. Mol. Cell Biol. 2013;14:416-429.

21. Pasca di Magliano M, Hebrok M. Hedgehog signalling in cancer formation and maintenance. Nat. Rev. Cancer 2004;3:903-911.

22. Kubo M, Nakamura M, Tasaki A, Yamanaka N, Nakashima H, Nomura M, et al. Hedgehog signaling pathway is a new therapeutic target for patients with breast cancer. Cancer Res. 2004;64:6071-6074.

23. Karhadkar SS, Bova GS, Abdallah N, Dhara S, Gardner D, Maitra A, et al. Hedgehog signalling in prostate regeneration, neoplasia and metastasis. Nature 2004;431:707-712.

24. Yuan Z, Goetz JA, Singh S, Ogden SK, Petty WJ, Black CC, et al. Frequent requirement of hedgehog signaling in non-small cell lung carcinoma. Oncogene 2006;26:1046-1055.

25. Honami T, Shimo T, Okui T, Kurio N, Hassan NMM, Iwamoto M, et al. Sonic hedgehog signaling promotes growth of oral squamous cell carcinoma cells associated with bone destruction. Oral Oncol. 2012;48:49-55.

26. Sterling JA, Oyajobi BO, Grubbs B, Padalecki SS, Munoz SA, Gupta A, et al. The hedgehog signaling molecule Gli2 induces parathyroid hormone-related peptide expression and osteolysis in metastatic human breast cancer cells. Cancer Res. 2006;66:7548-7553.

27. Cannonier SA, Sterling JA. The role of hedgehog signaling in tumor induced bone disease. Cancers (Basel) 2015;7:1658-1683.

28. Johnson RW, Nguyen MP, Padalecki SS, Grubbs BG, Merkel AR, Oyajobi BO, et al. TGF-beta promotion of Gli2-induced expression of parathyroid hormone-related protein, an important osteolytic factor in bone metastasis, is independent of canonical hedgehog signaling. Cancer Res. 2011;71:822-831.

29. LoRusso PM, Rudin CM, Reddy JC, Tibes R, Weiss GJ, Borad MJ, et al. Phase I trial of hedgehog pathway inhibitor vismodegib (GDC-0449) in patients with refractory, locally advanced or metastatic solid tumors. Clin. Cancer Res. 2011;17:2502-2511.

30. Jimeno A, Weiss GJ, Miller WH, Jr., Gettinger S, Eigl BJ, Chang AL, et al. Phase I study of the hedgehog pathway inhibitor IPI-926 in adult patients with solid tumors. Clin. Cancer Res. 2013;19:2766-2774.

31. Wagner AJ, Messersmith WA, Shaik MN, Li S, Zheng X, McLachlan KR, et al. A phase I study of PF-04449913, an oral hedgehog inhibitor, in patients with advanced solid tumors. Clin. Cancer Res. 2014;21:1044-1051.

32. Metcalfe C, de Sauvage FJ. Hedgehog fights back: Mechanisms of acquired resistance against smoothened antagonists. Cancer Res. 2011;71:5057-5061.

33. Atwood SX, Sarin KY, Whitson RJ, Li JR, Kim G, Rezaee M, et al. Smoothened variants explain the majority of drug resistance in basal cell carcinoma. Cancer Cell 2015;27:342-353.

34. Johnson RW, Merkel AR, Page JM, Ruppender NS, Guelcher SA, Sterling JA. Wnt signaling induces gene expression of factors associated with bone destruction in lung and breast cancer. Clin. Exp. Metastasis 2014;31:945-959.

35. Lauth M, Bergstrom A, Shimokawa T, Toftgard R. Inhibition of GLI-mediated transcription and tumor cell growth by small-molecule antagonists. Proc. Natl. Acad. Sci. USA 2007;104:8455-8460.

36. Hyman JM, Firestone AJ, Heine VM, Zhao Y, Ocasio CA, Han K, et al. Small-molecule inhibitors reveal multiple strategies for hedgehog pathway blockade. Proc. Natl. Acad. Sci. USA 2009;106:14132-14137.

37. Humphrey JD, Dufresne ER, Schwartz MA. Mechanotransduction and extracellular matrix homeostasis. Nat. Rev. Mol. Cell Biol. 2014;15:802-812.

38. Paszek MJ, Zahir N, Johnson KR, Lakins JN, Rozenberg GI, Gefen A, et al. Tensional homeostasis and the malignant phenotype. Cancer Cell 2005;8:241-254.

39. Levental KR, Yu H, Kass L, Lakins JN, Egeblad M, Erler JT, et al. Matrix crosslinking forces tumor progression by enhancing integrin signaling. Cell 2009;139:891-906.

40. Guelcher SA, Sterling JA. Contribution of bone tissue modulus to breast cancer metastasis to bone. Cancer Microenviron. 2011;4:247-259.

41. Sterling JA, Guelcher SA. Bone structural components regulating sites of tumor metastasis. Curr. Osteoporos. Rep. 2011;9:89-95.

42. Ruppender NS, Merkel AR, Martin TJ, Mundy GR, Sterling JA, Guelcher SA. Matrix rigidity induces osteolytic gene expression of metastatic breast cancer cells. PLoS One 2010;5:e15451.

43. Page JM, Merkel AR, Ruppender NS, Guo R, Dadwal UC, Cannonier S, et al. Matrix rigidity regulates the transition of tumor cells to a bone-destructive phenotype through integrin beta3 and TGF-beta receptor type II. Biomaterials 2015;64:33-44.

44. Logothetis CJ, Lin S-H. Osteoblasts in prostate cancer metastasis to bone. Nat. Rev. Cancer 2005;5:21-28.

45. Coleman RE, McCloskey EV. Bisphosphonates in oncology. Bone 2011;49:71-76.

46. Roodman GD. Mechanisms of bone metastasis. N. Engl. J. Med. 2004;350:1655-1664.

47. Takayama S, Ishii S, Ikeda T, Masamura S, Doi M, Kitajima M. The relationship between bone metastasis from human breast cancer and integrin alphavbeta3 expression. Anticancer Res. 2005;25:79-83.

48. McCabe NP, De S, Vasanji A, Brainard J, Byzova TV. Prostate cancer specific integrin alphavbeta3 modulates bone metastatic growth and tissue remodeling. Oncogene 2007;26:6238-6243.

49. Tucci M, De Palma R, Lombardi L, Rodolico G, Berrino L, Dammacco F, et al. Beta(3) integrin subunit mediates the bone-resorbing function exerted by cultured myeloma plasma cells. Cancer Res. 2009;69:6738-6746.

50. Tome Y, Kimura H, Maehara H, Sugimoto N, Bouvet M, Tsuchiya H, et al. High lung-metastatic variant of human osteosarcoma cells, selected by passage of lung metastasis in nude mice, is associated with increased expression of α(v)β(3) integrin. Anticancer Res. 2013;33:3623-3627.

51. Lai TH, Fong YC, Fu WM, Yang RS, Tang CH. Stromal cell-derived factor-1 increase alphavbeta3 integrin expression and invasion in human chondrosarcoma cells. J. Cell. Physiol. 2009;218:334-342.

52. Stucci S, Tucci M, Passarelli A, Silvestris F. Avβ3 integrin: Pathogenetic role in osteotropic tumors. Crit. Rev. Oncol. Hematol. 2015;96:183-193.

53. Horton M. The αvβ3 integrin 'vitronectin receptor'. Int. J. Biochem. Cell Biol. 1997;29:721–725.

54. Tadokoro S, Shattil SJ, Eto K, Tai V, Liddington RC, de Pereda JM, et al. Talin binding to integrin β tails: A final common step in integrin activation. Science 2003;302:103–106.

55. Ma YQ, Qin J, Wu C, Plow EF. Kindlin-2 (Mig-2): A co-activator of beta3 integrins. J. Cell Biol. 2008;181:439-446.

56. Giancotti FG, Ruoslahti E. Integrin signaling. Science 1999;285:1028-1032.

57. Qin J, Vinogradova O, Plow EF. Integrin bidirectional signaling: A molecular view. PLoS Biol. 2004;2:e169.

58. Liu Z, Han L, Dong Y, Tan Y, Li Y, Zhao M, et al. EGFRvIII/integrin β3 interaction in hypoxic and vitronectin enriching microenvironment promote GBM progression and metastasis. Oncotarget 2016;7:4680–4694.

59. Galliher AJ, Schiemann WP. Beta3 integrin and Src facilitate transforming growth factor-beta mediated induction of epithelial-mesenchymal transition in mammary epithelial cells. Breast Cancer Res. 2006;8:R42.

60. Guo W, Giancotti FG. Integrin signalling during tumour progression. Nat. Rev. Mol. Cell Biol. 2004;5:816-826.

61. Yeh YY, Chiao CC, Kuo WY, Hsiao YC, Chen YJ, Wei YY, et al. TGF-beta1 increases motility and alphavbeta3 integrin up-regulation via PI3K, Akt and NF-kappaB-dependent pathway in human chondrosarcoma cells. Biochem. Pharmacol. 2008;75:1292-1301.

62. Duong LT, Lakkakorpi P, Nakamura I, Rodan GA. Integrins and signaling in osteoclast function. Matrix Biol. 2000;19:97-105.

63. McHugh KP, Hodivala-Dilke K, Zheng MH, Namba N, Lam J, Novack D, et al. Mice lacking beta3 integrins are osteosclerotic because of dysfunctional osteoclasts. J. Clin. Invest. 2000;105:433-440.

64. Mahabeleshwar GH, Feng W, Phillips DR, Byzova TV. Integrin signaling is critical for pathological angiogenesis. J. Exp. Med. 2006;203:2495-2507.

65. Weis SM, Cheresh DA. AlphaV integrins in angiogenesis and cancer. Cold Spring Harb. Perspect. Med. 2011;1:a006478.

66. Savill J, Dransfield I, Hogg N, Haslett C. Vitronectin receptor-mediated phagocytosis of cells undergoing apoptosis. Nature 1990;343:170-173.

67. Schneider JG, Amend SR, Weilbaecher KN. Integrins and bone metastasis: Integrating tumor cell and stromal cell interactions. Bone 2011;48:54-65.

68. Vogetseder A, Thies S, Ingold B, Roth P, Weller M, Schraml P, et al. αv-Integrin isoform expression in primary human tumors and brain metastases. Int. J. Cancer 2013;133:2362-2371.

69. Liapis H, Flath A, Kitazawa S. Integrin αvβ3 expression by bone-residing breast cancer metastases. Diag. Molec. Path. 1996;5:127-135.

70. Pécheur I, Peyruchaud O, Serre CM, Guglielmi J, Voland C, Bourre F, et al. Integrin αvβ3 expression confers on tumor cells a greater propensity to metastasize to bone. FASEB J. 2002;16:1266-1268.

71. Peyruchaud O, Winding B, Pécheur I, Serre CM, Delmas P, Clézardin P. Early detection of bone metastases in a murine model using fluorescent human breast cancer cells: application to the use of the bisphosphonate zoledronic acid in the treatment of osteolytic lesions. J. Bone Miner. Res. 2001;16:2027-2034.

72. Sloan EK, Pouliot N, Stanley KL, Chia J, Moseley JM, Hards DK, et al. Tumor-specific expression of alphavbeta3 integrin promotes spontaneous metastasis of breast cancer to bone. Breast Cancer Res. 2006;8:R20.

73. Harms JF, Welch DR, Samant RS, Shevde LA, Miele ME, Babu GR, et al. A small molecule antagonist of the αvβ3 integrin suppresses MDA-MB-435 skeletal metastasis. Clin. Exp. Metastasis 2004;21:119–128.

74. Thomas RJ, Guise TA, Yin JJ, Elliott J, Horwood NJ, Martin TJ, et al. Breast cancer cells interact with osteoblasts to support osteoclast formation. Endocrinology 1999;140:4451–4458.

75. Zhao Y, Bachelier R, Treilleux I, Pujuguet P, Peyruchaud O, Baron R, et al. Tumor alphavbeta3 integrin is a therapeutic target for breast cancer bone metastases. Cancer Res. 2007;67:5821-5830.

76. Akech J, Wixted JJ, Bedard K, van der Deen M, Hussain S, Guise TA, et al. Runx2 association with progression of prostate cancer in patients: Mechanisms mediating bone osteolysis and osteoblastic metastatic lesions. Oncogene 2010;29:811-821.

77. Gupta A, Cao W, Chellaiah MA. Integrin αvβ3 and CD44 pathways in metastatic prostate cancer cells support osteoclastogenesis via a Runx2/Smad 5/receptor activator of NF-κB ligand signaling axis. Mol. Cancer 2012;11.

78. Coleman R. The use of bisphosphonates in cancer treatment. Ann. N.Y. Acad. Sci. 2011;1218:3-14.

79. Fizazi K, Lipton A, Mariette X, Body JJ, Rahim Y, Gralow JR, et al. Randomized phase II trial of denosumab in patients with bone metastases from prostate cancer, breast cancer, or other neoplasms after intravenous bisphosphonates. J. Clin. Oncol. 2009;27:1564-1571.

80. Mulgrew K, Kinneer K, Yao XT, Ward BK, Damschroder MM, Walsh B, et al. Direct targeting of alphavbeta3 integrin on tumor cells with a monoclonal antibody, Abegrin. Mol. Cancer Ther. 2006;5:3122-3129.

81. Khalili P, Arakelian A, Chen G, Plunkett ML, Beck I, Parry GC, et al. A non-RGD-based integrin binding peptide (ATN-161) blocks breast cancer growth and metastasis in vivo. Mol. Cancer Ther. 2006;5:2271-2280.

82. Reardon DA, Fink KL, Mikkelsen T, Cloughesy TF, O'Neill A, Plotkin S, et al. Randomized phase II study of cilengitide, an integrin-targeting arginine-glycine-aspartic acid peptide, in recurrent glioblastoma multiforme. J. Clin. Oncol. 2008;26:5610-5617.

83. Stupp R, Hegi ME, Gorlia T, Erridge SC, Perry J, Hong Y-K, et al. Cilengitide combined with standard treatment for patients with newly diagnosed glioblastoma with methylated MGMT promoter (CENTRIC EORTC 26071-22072 study): A multicentre, randomised, open-label, phase 3 trial. Lancet Oncol. 2014;15:1100-1108.

84. Hersey P, Sosman J, O'Day S, Richards J, Bedikian A, Gonzalez R, et al. A randomized phase 2 study of etaracizumab, a monoclonal antibody against integrin alpha(v)beta(3), + or - dacarbazine in patients with stage IV metastatic melanoma. Cancer 2010;116:1526-1534.

85. Cirkel GA, Kerklaan BM, Vanhoutte F, Van der Aa A, Lorenzon G, Namour F, et al. A dose escalating phase I study of GLPG0187, a broad spectrum integrin receptor antagonist, in adult patients with progressive high-grade glioma and other advanced solid malignancies. Invest. New Drugs 2016;34:184-192.

86. Buijs JT, van der Pluijm G. Osteotropic cancers: From primary tumor to bone. Cancer Lett. 2009;273:177-193.

87. Saad F, Lipton A, Cook R, Chen YM, Smith M, Coleman R. Pathologic fractures correlate with reduced survival in patients with malignant bone disease. Cancer 2007;110:1860-1867.

88. Sousa S, Clezardin P. Bone-targeted therapies in cancer-induced bone disease. Calcif. Tissue Int. 2018;102:227-250.

89. Edwards BJ, Sun M, West DP, Guindani M, Lin YH, Lu H, et al. Incidence of atypical femur fractures in cancer patients: The MD Anderson Cancer Center experience. J. Bone Miner. Res. 2016;31:1569-1576.

90. Yang SP, Kim TW, Boland PJ, Farooki A. Retrospective review of atypical femoral fracture in metastatic bone disease patients receiving denosumab therapy. Oncologist 2017;22:438-444.

91. Bamias A, Kastritis E, Bamia C, Moulopoulos LA, Melakopoulos I, Bozas G, et al. Osteonecrosis of the jaw in cancer after treatment with bisphosphonates: Incidence and risk factors. J. Clin. Oncol. 2005;23:8580-8587.

92. Coleman R, Woodward E, Brown J, Cameron D, Bell R, Dodwell D, et al. Safety of zoledronic acid and incidence of osteonecrosis of the jaw (ONJ) during adjuvant therapy in a randomised phase III trial (AZURE: BIG 01-04) for women with stage II/III breast cancer. Breast Cancer Res. Treat. 2011;127:429-438.

93. Smith MR, Saad F, Coleman R, Shore N, Fizazi K, Tombal B, et al. Denosumab and bone-metastasis-free survival in men with castration-resistant prostate cancer: Results of a phase 3, randomised, placebo-controlled trial. Lancet 2011;379:39-46.

94. Fan C, Georgiou KR, Morris HA, McKinnon RA, Keefe DMK, Howe PR, et al. Combination breast cancer chemotherapy with doxorubicin and cyclophosphamide damages bone and bone marrow in a female rat model. Breast Cancer Res. Treat. 2017;165:41-51.

95. Green DE, Rubin CT. Consequences of irradiation on bone and marrow phenotypes, and its relation to disruption of hematopoietic precursors. Bone 2014;63:87-94.

96. Neelakantan D, Zhou H, Oliphant MUJ, Zhang X, Simon LM, Henke DM, et al. EMT cells increase breast cancer metastasis via paracrine GLI activation in neighbouring tumour cells. Nat. Commun. 2017;8:15773.

97. Gonnissen A, Isebaert S, McKee CM, Dok R, Haustermans K, Muschel RJ. The hedgehog inhibitor GANT61 sensitizes prostate cancer cells to ionizing radiation both in vitro and in vivo. Oncotarget 2016;7:84286-84298.

98. Huang L, Walter V, Hayes DN, Onaitis M. Hedgehog-GLI signaling inhibition suppresses tumor growth in squamous lung cancer. Clin. Cancer Res. 2014;20:1566-1575.

99. Peer D, Karp JM, Hong S, Farokhzad OC, Margalit R, Langer R. Nanocarriers as an emerging platform for cancer therapy. Nat. Nanotechnol. 2007;2:751-760.

100. Wicki A, Witzigmann D, Balasubramanian V, Huwyler J. Nanomedicine in cancer therapy: Challenges, opportunities, and clinical applications. J. Control Release 2015;200:138-157.

101. Ashton S, Song YH, Nolan J, Cadogan E, Murray J, Odedra R, et al. Aurora kinase inhibitor nanoparticles target tumors with favorable therapeutic index in vivo. Sci. Transl. Med. 2016;8:325ra317.

102. Mizrachi A, Shamay Y, Shah J, Brook S, Soong J, Rajasekhar VK, et al. Tumour-specific PI3K inhibition via nanoparticle-targeted delivery in head and neck squamous cell carcinoma. Nat. Commun. 2017;8:14292.

103. Schmid D, Park CG, Hartl CA, Subedi N, Cartwright AN, Puerto RB, et al. T cell-targeting nanoparticles focus delivery of immunotherapy to improve antitumor immunity. Nat. Commun. 2017;8:1747.

104. Kwak EL, Clark JW, Chabner B. Targeted agents: The rules of combination. Clin. Cancer Res. 2007;13:5232-5237.

105. Gupta MK, Meyer TA, Nelson CE, Duvall CL. Poly(PS-b-DMA) micelles for reactive oxygen species triggered drug release. J. Control Release 2012;162:591-598.

106. Uddin MJ, Werfel TA, Crews BC, Gupta MK, Kavanaugh TE, Kingsley PJ, et al. Fluorocoxib A loaded nanoparticles enable targeted visualization of cyclooxygenase-2 in inflammation and cancer. Biomaterials 2016;92:71-80.

107. Chenna V, Hu C, Pramanik D, Aftab BT, Karikari C, Campbell NR, et al. A polymeric nanoparticle encapsulated small-molecule inhibitor of hedgehog signaling (NanoHHI) bypasses secondary mutational resistance to smoothened antagonists. Mol. Cancer Ther. 2012;11:165-173.

108. Blanco E, Shen H, Ferrari M. Principles of nanoparticle design for overcoming biological barriers to drug delivery. Nat. Biotechnol. 2015;33:941-951.

109. Wei T, Chen C, Liu J, Liu C, Posocco P, Liu X, et al. Anticancer drug nanomicelles formed by self-assembling amphiphilic dendrimer to combat cancer drug resistance. Proc. Natl. Acad. Sci. USA 2015;112:2978-2983.

110. Kim DW, Kim SY, Kim HK, Kim SW, Shin SW, Kim JS, et al. Multicenter phase II trial of Genexol-PM, a novel Cremophor-free, polymeric micelle formulation of paclitaxel, with cisplatin in patients with advanced non-small-cell lung cancer. Ann. Oncol. 2007;18:2009-2014.

111. Ramasamy T, Ruttala HB, Gupta B, Poudel BK, Choi HG, Yong CS, et al. Smart chemistry-based nanosized drug delivery systems for systemic applications: A comprehensive review. J. Control Release 2017;258:226-253.

112. Joshi RV, Nelson CE, Poole KM, Skala MC, Duvall CL. Dual pH- and temperature-responsive microparticles for protein delivery to ischemic tissues. Acta Biomater. 2013;9:6526-6534.

113. Li H, Miteva M, Kirkbride KC, Cheng MJ, Nelson CE, Simpson EM, et al. Dual MMP7-proximity-activated and folate receptor-targeted nanoparticles for siRNA delivery. Biomacromolecules 2014;16:192-201.

114. Poole KM, Nelson CE, Joshi RV, Martin JR, Gupta MK, Haws SC, et al. ROS-responsive microspheres for on demand antioxidant therapy in a model of diabetic peripheral arterial disease. Biomaterials 2015;41:166-175.

115. Guise TA, Yoneda T, Yates AJ, Mundy GR. The combined effect of tumor-produced parathyroid hormone-related protein and transforming growth factor-alpha enhance hypercalcemia in vivo and bone resorption in vitro. J. Clin. Endocrinol. Metab. 1993;77:40-45.

116. Zhang XH, Wang Q, Gerald W, Hudis CA, Norton L, Smid M, et al. Latent bone metastasis in breast cancer tied to src-dependent survival signals. Cancer Cell 2009;16:67-78.

117. Guo R, Lu S, Merkel AR, Sterling JA, Guelcher SA. Substrate modulus regulates osteogenic differentiation of rat mesenchymal stem cells through integrin β1 and BMP receptor type IA. J. Mater. Chem. B Mater. Biol. Med. 2016;4:3584-3593.

118. Mbalaviele G, Chen H, Boyce BF, Mundy GR, Yoneda T. The role of cadherin in the generation of multinucleated osteoclasts from mononuclear precursors in murine marrow. J. Clin. Invest. 1995;95:2757-2765.

119. Michigami T, Shimizu N, Williams PJ, Niewolna M, Dallas SL, Mundy GR, et al. Cell-cell contact between marrow stromal cells and myeloma cells via VCAM-1 and alpha(4)beta(1)-integrin enhances production of osteoclast-stimulating activity. Blood 2000;96:1953-1960.

120. Tietjen GT, DiRito J, Pober JS, Saltzman WM. Quantitative microscopy-based measurements of circulating nanoparticle concentration using microliter blood volumes. Nanomedicine 2017;13:1863-1867.

121. Wright LE, Ottewell PD, Rucci N, Peyruchaud O, Pagnotti GM, Chiechi A, et al. Murine models of breast cancer bone metastasis. Bonekey Rep. 2016;5:804.

122. Lam MH, Thomas RJ, Loveland KL, Schilders S, Gu M, Martin TJ, et al. Nuclear transport of parathyroid hormone (PTH)-related protein is dependent on microtubules. Mol. Endocrinol. 2002;16:390-401.

123. Ansari N, Ho PW, Crimeen-Irwin B, Poulton IJ, Brunt AR, Forwood MR, et al. Autocrine and paracrine regulation of the murine skeleton by osteocyte-derived parathyroid hormone-related protein. J. Bone Miner. Res. 2017;33:137-153.

124. Sparreboom A, van Zuylen L, Brouwer E, Loos WJ, de Bruijn P, Gelderblom H, et al. Cremophor EL-mediated alteration of paclitaxel distribution in human blood: Clinical pharmacokinetic implications. Cancer Res. 1999;59:1454-1457.

125. Gupta MK, Martin JR, Werfel TA, Shen T, Page JM, Duvall CL. Cell protective, ABC triblock polymer-based thermoresponsive hydrogels with ROS-triggered degradation and drug release. J. Am. Chem. Soc. 2014;136:14896-14902.

126. Dollinger BR, Gupta MK, Martin JR, Duvall CL. Reactive oxygen species shielding hydrogel for the delivery of adherent and nonadherent therapeutic cell types. Tissue Eng. Part A 2017;23:1120-1131.

127. O'Grady KP, Kavanaugh TE, Cho H, Ye H, Gupta MK, Madonna MC, et al. Drug-free ROS sponge polymeric microspheres reduce tissue damage from ischemic and mechanical injury. ACS Biomater. Sci. Eng. 2018;4:1251-1264.

128. Monfardini C, Schiavon O, Caliceti P, Morpurgo M, Harris JM, Veronese FM. A branched monomethoxypoly(ethylene glycol) for protein modification. Bioconjug. Chem. 1995;6:62-69.

129. Gao W, Liu W, Mackay JA, Zalutsky MR, Toone EJ, Chilkoti A. In situ growth of a stoichiometric PEG-like conjugate at a protein's N-terminus with significantly improved pharmacokinetics. Proc. Natl. Acad. Sci. USA 2009;106:15231-15236.

130. Gao W, Liu W, Christensen T, Zalutsky MR, Chilkoti A. In situ growth of a PEG-like polymer from the C terminus of an intein fusion protein improves pharmacokinetics and tumor accumulation. Proc. Natl. Acad. Sci. USA 2010;107:16432-16437.

131. Gurer-Orhan H, Ince E, Konyar D, Saso L, Suzen S. The role of oxidative stress modulators in breast cancer. Curr. Med. Chem. 2017;25:4084-4101.

132. Werfel TA, Jackson MA, Kavanaugh TE, Kirkbride KC, Miteva M, Giorgio TD, et al. Combinatorial optimization of PEG architecture and hydrophobic content improves ternary siRNA polyplex stability, pharmacokinetics, and potency in vivo. J. Control Release 2017;255:12-26.

133. Shane E, Burr D, Abrahamsen B, Adler RA, Brown TD, Cheung AM, et al. Atypical subtrochanteric and diaphyseal femoral fractures: Second report of a task force of the American Society for Bone and Mineral Research. J. Bone Miner. Res. 2013;29:1-23.

134. Pozzi S, Vallet S, Mukherjee S, Cirstea D, Vaghela N, Santo L, et al. High-dose zoledronic acid impacts bone remodeling with effects on osteoblastic lineage and bone mechanical properties. Clin. Cancer Res. 2009;15:5829-5839.

135. Idris AI, Rojas J, Greig IR, Van't Hof RJ, Ralston SH. Aminobisphosphonates cause osteoblast apoptosis and inhibit bone nodule formation in vitro. Calcif. Tissue Int. 2008;82:191-201.

136. Xu Y, Chenna V, Hu C, Sun HX, Khan M, Bai H, et al. Polymeric nanoparticle-encapsulated hedgehog pathway inhibitor HPI-1 (NanoHHI) inhibits systemic metastases in an orthotopic model of human hepatocellular carcinoma. Clin. Cancer Res. 2012;18:1291-1302.

137. Ross MH, Esser AK, Fox GC, Schmieder AH, Yang X, Hu G, et al. Bone-induced expression of integrin beta3 enables targeted nanotherapy of breast cancer metastases. Cancer Res. 2017;77:6299-6312.

138. Yamashita S, Katsumi H, Hibino N, Isobe Y, Yagi Y, Tanaka Y, et al. Development of PEGylated aspartic acid-modified liposome as a bone-targeting carrier for the delivery of paclitaxel and treatment of bone metastasis. Biomaterials 2018;154:74-85.

139. Hu W, Sung T, Jessen BA, Thibault S, Finkelstein MB, Khan NK, et al. Mechanistic investigation of bone marrow suppression associated with palbociclib and its differentiation from cytotoxic chemotherapies. Clin. Cancer Res. 2016;22:2000-2008.

140. Fonseca H, Carvalho A, Esteves J, Esteves VI, Moreira-Goncalves D, Duarte JA. Effects of doxorubicin administration on bone strength and quality in sedentary and physically active Wistar rats. Osteoporos. Int. 2016;27:3465-3475.

141. Mazumdar T, DeVecchio J, Agyeman A, Shi T, Houghton JA. Blocking hedgehog survival signaling at the level of the GLI genes induces DNA damage and extensive cell death in human colon carcinoma cells. Cancer Res. 2011;71:5904-5914.

142. Torchilin V. Tumor delivery of macromolecular drugs based on the EPR effect. Adv. Drug Deliv. Rev. 2011;63:131-135.

143. Jansen LE, Birch NP, Schiffman JD, Crosby AJ, Peyton SR. Mechanics of intact bone marrow. J. Mech. Behav. Biomed. Mater. 2015;50:299-307.

144. Sethi N, Dai X, Winter CG, Kang Y. Tumor-derived JAGGED1 promotes osteolytic bone metastasis of breast cancer by engaging notch signaling in bone cells. Cancer Cell 2011;19:192-205.

145. Zheng H, Bae Y, Kasimir-Bauer S, Tang R, Chen J, Ren G, et al. Therapeutic antibody targeting tumor- and osteoblastic niche-derived jagged1 sensitizes bone metastasis to chemotherapy. Cancer Cell 2017;32:731-747.e736.

146. Li C, Wang S, Xing Z, Lin A, Liang K, Song J, et al. A ROR1-HER3-lncRNA signalling axis modulates the Hippo-YAP pathway to regulate bone metastasis. Nat. Cell Biol. 2017;19:106-119.

147. Wan L, Pantel K, Kang Y. Tumor metastasis: Moving new biological insights into the clinic. Nat. Med. 2013;19:1450-1464.

148. Powell GJ, Southby J, Danks JA, Stillwell RG, Hayman JA, Henderson MA, et al. Localization of parathyroid hormone-related protein in breast cancer metastases: increased incidence in bone compared with other sites. Cancer Res. 1991;51:3059-3061.

149. Vigneswaran N, Williams MD. Epidemiologic trends in head and neck cancer and aids in diagnosis. Oral Maxillofac. Surg. Clin. North Am. 2014;26:123-141.

150. Warnakulasuriya S. Global epidemiology of oral and oropharyngeal cancer. Oral Oncol. 2009;45:309-316.

151. Bose P, Brockton NT, Dort JC. Head and neck cancer: From anatomy to biology. Int. J. Cancer 2013;133:2013-2023.

152. Cramer JD, Burtness B, Le QT, Ferris RL. The changing therapeutic landscape of head and neck cancer. Nat. Rev. Clin. Oncol. 2019;16:669-683.

153. Wong RJ, Keel SB, Glynn RJ, Varvares MA. Histological pattern of mandibular invasion by oral squamous cell carcinoma. Laryngoscope 2000;110:65-72.

154. Jimi E FH, Matsuo K, Tominaga K, Takahashi T, Nakanishi O. The cellular and molecular mechanisms of bone invasion by oral squamous cell carcinoma. Oral Dis. 2011;17:462-468.

155. Mucke T, Holzle F, Wagenpfeil S, Wolff KD, Kesting M. The role of tumor invasion into the mandible of oral squamous cell carcinoma. J. Cancer Res. Clin. Oncol. 2011;137:165-171.

156. Smits RWH, Ten Hove I, Dronkers EAC, Bakker Schut TC, Mast H, Baatenburg de Jong RJ, et al. Evaluation of bone resection margins of segmental mandibulectomy for oral squamous cell carcinoma. Int. J. Oral Maxillofac. Surg. 2018;47:959-964.

157. Lai TY, Wang TH, Liu CJ, Chao TF, Chen TJ, Hu YW. Risk factors for osteonecrosis of the jaw in oral cancer patients after surgery and eventual adjuvant treatment: The potential role of chemotherapy. Radiother. Oncol. 2017;123:406-411.

158. Jereczek-Fossa BA, Orecchia R. Radiotherapy-induced mandibular bone complications. Cancer Treat Rev. 2002;28:65-74.

159. Peterson DE, Doerr W, Hovan A, Pinto A, Saunders D, Elting LS, et al. Osteoradionecrosis in cancer patients: The evidence base for treatment-dependent frequency, current management strategies, and future studies. Support Care Cancer 2010;18:1089-1098.

160. Ruggiero SL, Dodson TB, Fantasia J, Goodday R, Aghaloo T, Mehrotra B, et al. American Association of Oral and Maxillofacial Surgeons position paper on medication-related osteonecrosis of the jaw--2014 update. J. Oral Maxillofac. Surg. 2014;72:1938-1956.

161. Yamada T, Tsuda M, Ohba Y, Kawaguchi H, Totsuka Y, Shindoh M. PTHrP promotes malignancy of human oral cancer cell downstream of the EGFR signaling. Biochem. Biophys. Res. Commun. 2008;368:575-581.

162. Foley J, Nickerson N, Riese DJ, Hollenhorst PC, Lorch G, Foley AM. At the crossroads: EGFR and PTHrP signaling in cancer-mediated diseases of bone. Odontology 2012;100:109-129.

163. Bossi P, Resteghini C, Paielli N, Licitra L, Pilotti S, Perrone F. Prognostic and predictive value of EGFR in head and neck squamous cell carcinoma. Oncotarget 2016;7:74362-74379.

164. Larkins E, Blumenthal GM, Yuan W, He K, Sridhara R, Subramaniam S, et al. FDA approval summary: Pembrolizumab for the treatment of recurrent or metastatic head and neck squamous cell carcinoma with disease progression on or after platinum-containing chemotherapy. Oncologist 2017;22:873-878.

165. Vermorken JB, Trigo J, Hitt R, Koralewski P, Diaz-Rubio E, Rolland F, et al. Open-label, uncontrolled, multicenter phase II study to evaluate the efficacy and toxicity of cetuximab as a single agent in patients with recurrent and/or metastatic squamous cell carcinoma of the head and neck who failed to respond to platinum-based therapy. J. Clin. Oncol. 2007;25:2171-2177.

166. Burtness B, Goldwasser MA, Flood W, Mattar B, Forastiere AA. Phase III randomized trial of cisplatin plus placebo compared with cisplatin plus cetuximab in metastatic/recurrent head and neck cancer: an Eastern Cooperative Oncology Group study. J. Clin. Oncol. 2005;23:8646-8654.

167. Vermorken JB, Mesia R, Rivera F, Remenar E, Kawecki A, Rottey S, et al. Platinum-based chemotherapy plus cetuximab in head and neck cancer. N. Engl. J. Med. 2008;359:1116-1127.

168. Bonner JA, Harari PM, Giralt J, Azarnia N, Shin DM, Cohen RB, et al. Radiotherapy plus cetuximab for squamous-cell carcinoma of the head and neck. N. Engl. J. Med. 2006;354:567-578.

169. Ang KK, Zhang Q, Rosenthal DI, Nguyen-Tan PF, Sherman EJ, Weber RS, et al. Randomized phase III trial of concurrent accelerated radiation plus cisplatin with or without cetuximab for stage III to IV head and neck carcinoma: RTOG 0522. J. Clin. Oncol. 2014;32:2940-2950.

170. Chen LF, Cohen EEW, Grandis JR. New strategies in head and neck cancer: Understanding resistance to epidermal growth factor receptor inhibitors. Clin. Cancer Res. 2010;16:2489-2495.

171. Byeon HK, Ku M, Yang J. Beyond EGFR inhibition: Multilateral combat strategies to stop the progression of head and neck cancer. Exp. Mol. Med. 2019;51:1-14.

172. Cannonier SA, Gonzales CB, Ely K, Guelcher SA, Sterling JA. Hedgehog and TGFbeta signaling converge on Gli2 to control bony invasion and bone destruction in oral squamous cell carcinoma. Oncotarget 2016;7:76062-76075.

173. Benvenuto M, Masuelli L, De Smaele E, Fantini M, Mattera R, Cucchi D, et al. In vitro and in vivo inhibition of breast cancer cell growth by targeting the Hedgehog/GLI pathway with SMO (GDC-0449) or GLI (GANT-61) inhibitors. Oncotarget 2016;7:9250-9270.

174. Vanderburgh JP, Kwakwa KA, Werfel TA, Merkel AR, Gupta MK, Johnson RW, et al. Systemic delivery of a Gli inhibitor via polymeric nanocarriers inhibits tumor-induced bone disease. J. Control Release 2019;311-312:257-272.

175. Vanderburgh J, Hill JL, Gupta MK, Kwakwa KA, Wang SK, Moyer K, et al. Tuning ligand density to optimize pharmacokinetics of targeted nanoparticles for dual protection against tumor-induced bone destruction. ACS Nano. 2020;14:311-327.

176. Pao W, Miller VA, Politi KA, Riely GJ, Somwar R, Zakowski MF, et al. Acquired resistance of lung adenocarcinomas to gefitinib or erlotinib is associated with a second mutation in the EGFR kinase domain. PLoS Med. 2005;2:e73.

177. Kobayashi S, Boggon TJ, Dayaram T, Jänne PA, Kocher O, Meyerson M, et al. EGFR mutation and resistance of non-small-cell lung cancer to gefitinib. N. Engl. J. Med. 2005;352:786-792.

178. Sok JC, Coppelli FM, Thomas SM, Lango MN, Xi S, Hunt JL, et al. Mutant epidermal growth factor receptor (EGFRvIII) contributes to head and neck cancer growth and resistance to EGFR targeting. Clin. Cancer Res. 2006;12:5064-5073.

179. Tinhofer I, Klinghammer K, Weichert W, Knödler M, Stenzinger A, Gauler T, et al. Expression of amphiregulin and EGFRvIII affect outcome of patients with squamous cell carcinoma of the head and neck receiving cetuximab-docetaxel treatment. Clin. Cancer Res. 2011;17:5197-5204.

180. Xiang J, Fu X, Ran W, Wang Z. Grhl2 reduces invasion and migration through inhibition of TGFβ-induced EMT in gastric cancer. Oncogenesis 2017;6:e284-e284.

181. Chung VY, Tan TZ, Ye J, Huang R-L, Lai H-C, Kappei D, et al. The role of GRHL2 and epigenetic remodeling in epithelial–mesenchymal plasticity in ovarian cancer cells. Commun. Biol. 2019;2.

182. Raoof S, Mulford IJ, Frisco-Cabanos H, Nangia V, Timonina D, Labrot E, et al. Targeting FGFR overcomes EMT-mediated resistance in EGFR mutant non-small cell lung cancer. Oncogene 2019;38:6399-6413.

183. Lu Y, Liu Y, Oeck S, Zhang GJ, Schramm A, Glazer PM. Hypoxia induces resistance to EGFR inhibitors in lung cancer cells via upregulation of FGFR1 and the MAPK pathway. Cancer Res. 2020;80:4655-4667.

184. Fisher JE, Rodan GA, Reszka AA. In vivo effects of bisphosphonates on the osteoclast mevalonate pathway. Endocrinology 2000;141:4793-4796.

185. Rogers MJ, Crockett JC, Coxon FP, Mönkkönen J. Biochemical and molecular mechanisms of action of bisphosphonates. Bone 2011;49:34-41.

186. Mangelberger D. Cooperative Hedgehog-EGFR signaling. Front Biosci. (Landmark Ed) 2012;17:90.

187. Schnidar H, Eberl M, Klingler S, Mangelberger D, Kasper M, Hauser-Kronberger C, et al. Epidermal growth factor receptor signaling synergizes with Hedgehog/GLI in oncogenic transformation via activation of the MEK/ERK/JUN pathway. Cancer Res. 2009;69:1284-1292.

188. Eberl M, Klingler S, Mangelberger D, Loipetzberger A, Damhofer H, Zoidl K, et al. Hedgehog-EGFR cooperation response genes determine the oncogenic phenotype of basal cell carcinoma and tumour-initiating pancreatic cancer cells. EMBO Mol. Med. 2012;4:218-233.

189. Zhu G, Zhou J, Song W, Wu D, Dang Q, Zhang L, et al. Role of GLI-1 in epidermal growth factor-induced invasiveness of ARCaPE prostate cancer cells. Oncol. Rep. 2013;30:904-910.

190. Brand TM, Dunn EF, Iida M, Myers RA, Kostopoulos KT, Li C, et al. Erlotinib is a viable treatment for tumors with acquired resistance to cetuximab. Cancer Biol. Ther. 2011;12:436-446.

191. Ma XH, Piao S, Wang D, McAfee QW, Nathanson KL, Lum JJ, et al. Measurements of tumor cell autophagy predict invasiveness, resistance to chemotherapy, and survival in melanoma. Clin. Cancer Res. 2011;17:3478-3489.

192. Lee JM, Mhawech-Fauceglia P, Lee N, Parsanian LC, Lin YG, Gayther SA, et al. A three-dimensional microenvironment alters protein expression and chemosensitivity of epithelial ovarian cancer cells in vitro. Lab Investig. 2013;93:528-542.

193. Imamura Y, Mukohara T, Shimono Y, Funakoshi Y, Chayahara N, Toyoda M, et al. Comparison of 2D- and 3D-culture models as drug-testing platforms in breast cancer. Oncol. Rep. 2015;33:1837-1843.

194. Vantangoli MM, Madnick SJ, Huse SM, Weston P, Boekelheide K. MCF-7 human breast cancer cells form differentiated microtissues in scaffold-free hydrogels. PLoS One 2015;10:1-20.

195. Härmä V, Virtanen J, Mäkelä R, Happonen A, Mpindi JP, Knuuttila M, et al. A comprehensive panel of three-dimensional models for studies of prostate cancer growth, invasion and drug responses. PLoS One 2010;5:e10431-e10431.

196. Cichon MA, Gainullin VG, Zhang Y, Radisky DC. Growth of lung cancer cells in three-dimensional microenvironments reveals key features of tumor malignancy. Integr. Biol. 2012;4:440-448.

197. Luca AC, Mersch S, Deenen R, Schmidt S, Messner I, Schäfer KL, et al. Impact of the 3D microenvironment on phenotype, gene expression, and EGFR inhibition of colorectal cancer cell lines. PLoS One 2013;8:e59689-e59689.

198. Sokol ES, Miller DH, Breggia A, Spencer KC, Arendt LM, Gupta PB. Growth of human breast tissues from patient cells in 3D hydrogel scaffolds. Breast Cancer Res. 2016;18:1-13.

199. Xu X, Gurski LA, Zhang C, Harrington DA, Farach-Carson MC, Jia X. Recreating the tumor microenvironment in a bilayer, hyaluronic acid hydrogel construct for the growth of prostate cancer spheroids. Biomaterials 2012;33:9049-9060.

200. Szot CS, Buchanan CF, Freeman JW, Rylander MN. 3D in vitro bioengineered tumors based on collagen I hydrogels. Biomaterials 2011;32:7905-7912.

201. Riching KM, Cox BL, Salick MR, Pehlke C, Riching AS, Ponik SM, et al. 3D collagen alignment limits protrusions to enhance breast cancer cell persistence. Biophys. J. 2014;107:2546-2558.

202. Kleinman HK, Martin GR. Matrigel: Basement membrane matrix with biological activity. Semin. Cancer Biol. 2005;15:378-386.

203. Lovitt CJ, Shelper TB, Avery VM. Evaluation of chemotherapeutics in a three-dimensional breast cancer model. J. Cancer Res. Clin. Oncol. 2015;141:951-959.

204. Hughes CS, Postovit LM, Lajoie GA. Matrigel: A complex protein mixture required for optimal growth of cell culture. Proteomics 2010;10:1886-1890.

205. Chung IM, Enemchukwu NO, Khaja SD, Murthy N, Mantalaris A, García AJ. Bioadhesive hydrogel microenvironments to modulate epithelial morphogenesis. Biomaterials 2008;29:2637-2645.

206. Gurski LA, Petrelli NJ, Jia X, Farach-Carson MC. 3D matrices for anti-cancer drug testing and development. Oncol. Issues 2010;25:20-25.

207. Gill BJ, Gibbons DL, Roudsari LC, Saik JE, Rizvi ZH, Roybal JD, et al. A synthetic matrix with independently tunable biochemistry and mechanical properties to study epithelial morphogenesis and EMT in a lung adenocarcinoma model. Cancer Res. 2012;72:6013-6023.

208. Del Bufalo F, Manzo T, Hoyos V, Yagyu S, Caruana I, Jacot J, et al. 3D modeling of human cancer: A PEG-fibrin hydrogel system to study the role of tumor microenvironment and recapitulate the in vivo effect of oncolytic adenovirus. Biomaterials 2016;84:76-85.

209. Pradhan S, Hassani I, Seeto WJ, Lipke EA. PEG-fibrinogen hydrogels for three-dimensional breast cancer cell culture. J. Biomed. Mater. Res. Part A 2017;105:236-252.

210. Feder-Mengus C, Ghosh S, Reschner A, Martin I, Spagnoli GC. New dimensions in tumor immunology: What does 3D culture reveal? Trends Mol. Med. 2008;14:333-340.

211. Zanoni M, Piccinini F, Arienti C, Zamagni A, Santi S, Polico R, et al. 3D tumor spheroid models for in vitro therapeutic screening: a systematic approach to enhance the biological relevance of data obtained. Sci. Rep. 2016;6:19103-19103.

212. Vinci M, Gowan S, Boxall F, Patterson L, Zimmermann M, Court W, et al. Advances in establishment and analysis of three-dimensional tumor spheroid-based functional assays for target validation and drug evaluation. BMC Biol. 2012;10:1-20.

213. Breslin S, O'Driscoll L. Three-dimensional cell culture: The missing link in drug discovery. Drug Discov. Today 2013;18:240-249.

214. Yip D, Cho CH. A multicellular 3D heterospheroid model of liver tumor and stromal cells in collagen gel for anti-cancer drug testing. Biochem. Biophys. Res. Commun. 2013;433:327-332.

215. Tung Y-C, Hsiao AY, Allen SG, Torisawa Y-s, Ho M, Takayama S. High-throughput 3D spheroid culture and drug testing using a 384 hanging drop array. Analyst 2011;136:473-478.

216. Amann A, Zwierzina M, Gamerith G, Bitsche M, Huber JM, Vogel GF, et al. Development of an innovative 3D cell culture system to study tumour-stroma interactions in non-small cell lung cancer cells. PLoS One 2014;9.

217. Raghavan S, Ward MR, Rowley KR, Wold RM, Takayama S, Buckanovich RJ, et al. Formation of stable small cell number three-dimensional ovarian cancer spheroids using hanging drop arrays for preclinical drug sensitivity assays. Gynecol. Oncol. 2015;138:181-189.

218. Raghavan S, Mehta P, Horst EN, Ward MR, Rowley KR, Mehta G. Comparative analysis of tumor spheroid generation techniques for differential in vitro drug toxicity. Oncotarget 2016;7:16948-16961.

219. Aboulafia AJ, Levine AM, Schmidt D, Aboulafia D. Surgical therapy of bone metastases. Semin. Oncol. 2007;34:206-214.

220. García-Alvarez R, Izquierdo-Barba I, Vallet-Regí M. 3D scaffold with effective multidrug sequential release against bacteria biofilm. Acta Biomater. 2016;49:113-126.

221. Sundelacruz S, Li C, Choi YJ, Levin M, Kaplan DL. Bioelectric modulation of wound healing in a 3D invitro model of tissue-engineered bone. Biomaterials 2013;34:6695-6705.

222. Lee JH, Gu Y, Wang H, Lee WY. Microfluidic 3D bone tissue model for high-throughput evaluation of wound-healing and infection-preventing biomaterials. Biomaterials 2012;33:999-1006.

223. Chatterjee K, Lin-Gibson S, Wallace WE, Parekh SH, Lee YJ, Cicerone MT, et al. The effect of 3D hydrogel scaffold modulus on osteoblast differentiation and mineralization revealed by combinatorial screening. Biomaterials 2010;31:5051-5062.

224. Guo R, Lu S, Page JM, Merkel AR, Basu S, Sterling JA, et al. Fabrication of 3D scaffolds with precisely controlled substrate modulus and pore size by templated-fused deposition modeling to direct osteogenic differentiation. Adv. Healthc. Mater. 2015;4:1826-1832.

225. Sun L, Parker ST, Syoji D, Wang X, Lewis JA, Kaplan DL. Direct-write assembly of 3D silk/hydroxyapatite scaffolds for bone co-cultures. Adv. Healthc. Mater. 2012;1:729-735.

226. Bidan CM, Kommareddy KP, Rumpler M, Kollmannsberger P, Fratzl P, Dunlop JWC. Geometry as a factor for tissue growth: Towards shape optimization of tissue engineering scaffolds. Adv. Healthc. Mater. 2013;2:186-194.

227. Gamsjager E, Bidan CM, Fischer FD, Fratzl P, Dunlop JWC. Modelling the role of surface stress on the kinetics of tissue growth in confined geometries. Acta Biomater. 2013;9:5531-5543.

228. Yamada KM, Cukierman E. Modeling tissue morphogenesis and cancer in 3D. Cell 2007;130:601-610.

229. Fischbach C, Chen R, Matsumoto T, Schmelzle T, Brugge JS, Polverini PJ, et al. Engineering tumors with 3D scaffolds. Nat. Methods 2007;4:855-860.

230. Schuessler TK, Chan XY, Chen HJ, Ji K, Park KM, Roshan-Ghias A, et al. Biomimetic tissue-engineered systems for advancing cancer research: NCI strategic workshop report. Cancer Res. 2014;74:5359-5363.

231. Temple JP, Hutton DL, Hung BP, Huri PY, Cook Ca, Kondragunta R, et al. Engineering anatomically shaped vascularized bone grafts with hASCs and 3D-printed PCL scaffolds. J. Biomed. Mater. Res. Part A 2014;102:4317-4325.

232. Williams JM, Adewunmi A, Schek RM, Flanagan CL, Krebsbach PH, Feinberg SE, et al. Bone tissue engineering using polycaprolactone scaffolds fabricated via selective laser sintering. Biomaterials 2005;26:4817-4827.

233. Petrie Aronin CE, Cooper JA, Sefcik LS, Tholpady SS, Ogle RC, Botchwey EA. Osteogenic differentiation of dura mater stem cells cultured in vitro on three-dimensional porous scaffolds of poly(epsilon-caprolactone) fabricated via co-extrusion and gas foaming. Acta Biomater. 2008;4:1187-1197.

234. Gay S, Arostegui S, Lemaitre J. Preparation and characterization of dense nanohydroxyapatite/PLLA composites. Mater. Sci. Eng. C 2009;29:172-177.

235. Guillaume O, Geven MA, Sprecher CM, Stadelmann VA, Grijpma DW, Tang TT, et al. Surface-enrichment with hydroxyapatite nanoparticles in stereolithography-fabricated composite polymer scaffolds promotes bone repair. Acta Biomater. 2017;54:386-398.

236. Grinberg O, Binderman I, Bahar H, Zilberman M. Highly porous bioresorbable scaffolds with controlled release of bioactive agents for tissue-regeneration applications. Acta Biomater. 2010;6:1278-1287.

237. Horning JL, Sahoo SK, Vijayaraghavalu S, Dimitrijevic S, Vasir JK, Jain TK, et al. 3-D tumor model for in vitro evaluation of anticancer drugs. Mol. Pharm. 2008;5:849-862.

238. Zhang P, Wu H, Wu H, Lù Z, Deng C, Hong Z, et al. RGD-conjugated copolymer incorporated into composite of poly(lactide-co-glycotide) and poly(l-lactide)-grafted nanohydroxyapatite for bone tissue engineering. Biomacromolecules 2011;12:2667-2680.

239. Guelcher SA. Biodegradable polyurethanes: Synthesis and applications in regenerative medicine. Tissue Eng. Part B Rev. 2008;14:3-17.

240. Temenoff JS, Mikos aG. Injectable biodegradable materials for orthopedic tissue engineering. Biomaterials 2000;21:2405-2412.

241. Kim K, Dean D, Mikos AG, Fisher JP. Effect of initial cell seeding density on early osteogenic signal expression of rat bone marrow stromal cells cultured on cross-linked poly(propylene fumarate) disks. Biomacromolecules 2009;10:1810-1817.

242. Chattopadhyay S, Raines RT. Collagen-based biomaterials for wound healing. Biopolymers 2015;101:821-833.

243. Reagan MR, Mishima Y, Glavey SV, Zhang Y, Manier S, Lu ZN, et al. Investigating osteogenic differentiation in multiple myeloma using a novel 3D bone marrow niche model. Blood 2014;124:3250-3259.

244. Vepari C, Kaplan DL. Silk as a biomaterial. Prog. Polym. Sci. 2007;32:991-1007.

245. Kwon H, Kim HJ, Rice WL, Subramanian B, Park S-h, Georgakoudi I, et al. Development of an in vitro model to study the impact of BMP-2 on metastasis to bone. J. Tissue Eng. Regen. Med. 2010;4:590-599.

246. Mastro AM, Vogler EA. A three-dimensional osteogenic tissue model for the study of metastatic tumor cell interactions with bone. Cancer Res. 2009;69:4097-4100.

247. Thein-Han W, Xu HHK. Prevascularization of a gas-foaming macroporous calcium phosphate cement scaffold via coculture of human umbilical vein endothelial cells and osteoblasts. Tissue Eng. Part A 2013;19:1675-1685.

248. Annabi N, Fathi A, Mithieux SM, Martens P, Weiss AS, Dehghani F. The effect of elastin on chondrocyte adhesion and proliferation on poly(epsilon-caprolactone)/elastin composites. Biomaterials 2011;32:1517-1525.

249. Akar B, Jiang B, Somo SI, Appel AA, Larson JC, Tichauer KM, et al. Biomaterials with persistent growth factor gradients in vivo accelerate vascularized tissue formation. Biomaterials 2015;72:61-73.

250. Zhang J, Zhou H, Yang K, Yuan Y, Liu C. RhBMP-2-loaded calcium silicate/calcium phosphate cement scaffold with hierarchically porous structure for enhanced bone tissue regeneration. Biomaterials 2013;34:9381-9392.

251. Fereshteh Z, Fathi M, Bagri A, Boccaccini AR. Preparation and characterization of aligned porous PCL/zein scaffolds as drug delivery systems via improved unidirectional freeze-drying method. Mater. Sci. Eng. C 2016;68:613-622.

252. Vanderburgh J, Sterling JA, Guelcher SA. 3D printing of tissue engineered constructs for in vitro modeling of disease progression and drug screening. Ann. Biomed. Eng. 2016:1-16.

253. Hutmacher DW, Schantz T, Zein I, Ng KW, Teoh SH, Tan KC. Mechanical properties and cell cultural response of polycaprolactone scaffolds designed and fabricated via fused deposition modeling. J. Biomed. Mater. Res. 2001;55:203-216.

254. Lee SJ, Nowicki M, Harris B, Zhang LG. Fabrication of a highly aligned neural scaffold via a table top stereolithography 3D printing and electrospinning. Tissue Eng. Part A 2017;23:491-502.

255. Li G, Cuidi L, Fangping C, Changsheng L. Fabrication and characterization of toughness-enhanced scaffolds comprising beta-TCP/POC using the freeform fabrication system with micro-droplet jetting. Biomed. Mater. 2015;10:035009-035009.

256. Kundu J, Shim JH, Jang J, Kim SW, Cho DW. An additive manufacturing-based PCL-alginate-chondrocyte bioprinted scaffold for cartilage tissue engineering. J. Tissue Eng. Regen. Med. 2015;9:1286-1297.

257. Kang HW, Lee SJ, Ko IK, Kengla C, Yoo JJ, Atala A. A 3D bioprinting system to produce human-scale tissue constructs with structural integrity. Nat. Biotechnol. 2016:312-319.

258. Bancroft GN, Sikavitsas VI, van den Dolder J, Sheffield TL, Ambrose CG, Jansen JA, et al. Fluid flow increases mineralized matrix deposition in 3D perfusion culture of marrow stromal osteoblasts in a dose-dependent manner. Proc. Natl. Acad. Sci. USA 2002;99:12600-12605.

259. Krishnan V, Vogler EA, Mastro AM. Three-dimensional in vitro model to study osteobiology and osteopathology. J. Cell Biochem. 2015;116:2715-2723.

260. Talukdar S, Nguyen QT, Chen AC, Sah RL, Kundu SC. Effect of initial cell seeding density on 3D-engineered silk fibroin scaffolds for articular cartilage tissue engineering. Biomaterials 2011;32:8927-8937.

261. Talukdar S, Kundu SC. Engineered 3D silk-based metastasis models: Interactions between human breast adenocarcinoma, mesenchymal stem cells and osteoblast-like cells. Adv. Funct. Mater. 2013;23:5249-5260.

262. Mastro AM, Gay CV, Welch DR, Donahue HJ, Jewell J, Mercer R, et al. Breast cancer cells induce osteoblast apoptosis: A possible contributor to bone degradation. J. Cell Biochem. 2004;91:265-276.

263. Subia B, Dey T, Sharma S, Kundu SC. Target specific delivery of anticancer drug in silk fibroin based 3D distribution model of bone-breast cancer cells. ACS Appl. Mater. Interfaces 2015;7:2269-2279.

264. Lynch ME, Chiou AE, Lee MJ, Marcott SC, Polamraju PV, Lee Y, et al. Three-dimensional mechanical loading modulates the osteogenic response of mesenchymal stem cells to tumor-derived soluble signals. Tissue Eng. Part A 2016;22:1006-1015.

265. Zhu W, Holmes B, Glazer RI, Zhang LG. 3D printed nanocomposite matrix for the study of breast cancer bone metastasis. Nanomedicine 2016;12:69-79.

266. Wang Y, Pivonka P, Buenzli PR, Smith DW, Dunstan CR. Computational modeling of interactions between multiple myeloma and the bone microenvironment. PLoS One 2011;6:e27494-e27494.

267. Araujo A, Cook LM, Lynch CC, Basanta D. An integrated computational model of the bone microenvironment in bone-metastatic prostate cancer. Cancer Res. 2014;14:2391-2401.

268. Dadwal UC, Merkel AR, Page JM, Kwakwa KA, Kessler M, Rhoades JA. 3D bone morphology alters gene expression, motility, and drug responses in bone metastatic tumor cells. Int. J. Mol. Sci. 2020;21:6913.

269. Dang CV, Reddy EP, Shokat KM, Soucek L. Drugging the 'undruggable' cancer targets. Nat. Rev. Cancer 2017;17:502-508.

270. Kwakwa KA, Vanderburgh JP, Guelcher SA, Sterling JA. Engineering 3D models of tumors and bone to understand tumor-induced bone disease and improve treatments. Curr. Osteoporos. Rep. 2017;15:247-254.

271. Zhang Z, Zhou L, Xie N, Nice EC, Zhang T, Cui Y, et al. Overcoming cancer therapeutic bottleneck by drug repurposing. Signal Transduct. Target Ther. 2020;5.